The Dissertation Committee for James Roland Welch Certifies that this is the approved version of the following dissertation:

SELF-MODULATED LASER WAKEFIELDS DRIVEN BY A CO_2 LASER

Committee:

Michael C. Downer, Supervisor

John Keto

Todd Ditmire

Mikhail Belkin

SELF-MODULATED LASER WAKEFIELDS DRIVEN BY A CO_2 LASER

by

James Roland Welch

DISSERTATION

Presented to the Faculty of the Graduate School of

The University of Texas at Austin

in Partial Fulfillment

of the Requirements

for the Degree of

DOCTOR OF PHILOSOPHY

The University of Texas at Austin

August 2019

Self-Modulated Laser Wakefields Driven By a CO_2 LASER

James Roland Welch, PhD

The University of Texas at Austin, 2019

Supervisor: Michael C. Downer

Long-wavelength lasers are being explored for use in multi-stage laser wakefield accelerators with the eventual goal of creating a TeV-scale lepton collider. We use a high-power, ultrafast CO_2 laser (5 J, 4 ps, 10.6 μm) to generate self-modulated laser wakefields in a hydrogen gas jet, the first such experiment in this regime to our knowledge. Collective Thomson scattering (CTS) co-propagating probes were used to measure the plasma density in the gas jet and estimate the wakefield amplitudes. The measured wakefield have similar amplitudes to previous self-modulated laser wakefield experiments which measured accelerated electrons. The effects of gas jet geometry on the measured wavelength shift of the CTS probes were explored in depth, demonstrating a complex interplay of self-focusing and divergence effects based on the local plasma density and the pulse power.

Table of Contents

List of Tables

List of Figures

Chapter 1: Introduction

Unlike many dissertations which are placed squarely in a single continuous philosophical history, this dissertation deals with topics at the intersection of two scientific traditions: electron accelerator science and ultrafast lasers. Additional extension to the field of plasma physics could be justified, but is eschewed in favor of a focus on the practical details of plasmas.

A review of the relevant developments in each of these fields is presented to provide context for the motivation of the work. The evolution of the laser-plasma accelerator concept is tracked from its foundational text in 1979 through the major developments of the past decade. The chapter concludes with a detailed exploration of the propagation dynamics of a laser pulse through gaseous media over multiple intensity regimes.

1.1 History of Electron Acceleration

Development of accelerators has always been coupled with their intended use. The dawn of high-energy electron acceleration methods began with the desire to understand the nucleus. After Rutherfold probed the nucleus of gold with alpha particle emitters [1], the development of electrostatic accelerators followed rapidly to explore the centers of atoms. Robert J. van der Graff utilized the triboelectric effect to generate large, steady DC voltages. The original design separate electrons and ions by rubbing dissimilar materials together, then used a silk belt to transport the charges to metallic spheres which held potentials limited only by the breakdown voltage of surrounding media. He designed versions of these which reached peaks of 1.5 MV [2] and then 10 MV [3]. This basic idea was eventually used by M. A. Tuve, et al., to create a 1-m diameter sphere capable of

generating 600 kV of potential for proton experiments [4]. Figure 1.1 displays a picture of a van der Graff generator capable of producing over one million volts.

Simultaneous to van der Graff, Cockcroft and Walton were developing a system of diodes and capacitors in series which utilized AC current to charge high DC voltages. The

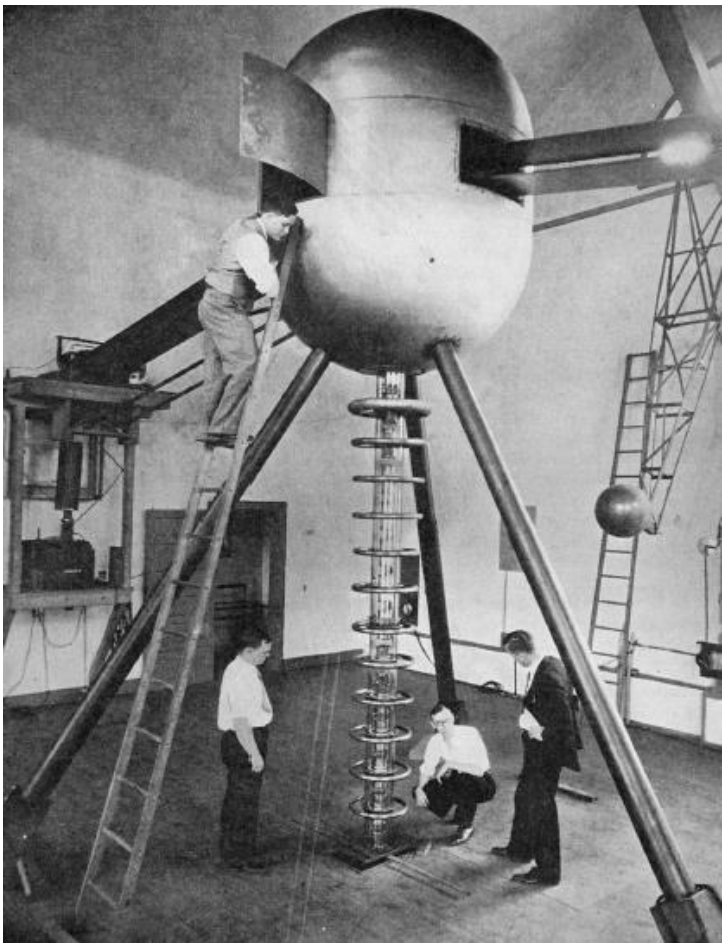

Figure 1.1: View of a two-meter van der Graff generator with provisional cascade tube capable of producing voltages as high as 1,300 kV

operating principle resembles a cascade of buckets, in which one capacitor is filled with charge during one half of the AC cycle, then spills half its charge into the next capacitor during the second half of the AC cycle. The relative simplicity and inexpensiveness of the

design allowed Cockcroft and Walton to achieve protons of energies as high as 700 keV [5], which were used to bombard lithium nuclei [6]. Detection of resultant helium nuclei confirmed the splitting of the atom, for which Cockcraft and Walton received the Nobel Prize for Physics in 1951 [7].

While providing the first successes, the technical and practical limitations of ever-increasing voltages prevented the electrostatic methods from extending the energy frontier ever higher. Mitigation of dielectric breakdown from the large quantities of stored charge required increasingly elaborate experimental facilities. Instead, two new accelerator design paradigms took hold and continue to dominate today: linear accelerators and circular accelerators based on non-static forces.

While tools for accelerating electrons in a linear fashion existed before, going back to at least the early Crookes tubes of 1870 [8], the idea for the first linear accelerator is often attributed to Gustav Ising, who proposed a linac model in 1924 [9]. Ising proposed that a series of increasingly long metallic "drift tubes" with alternating voltages between neighboring tubes, separated by gaps in an evacuated tube, could accelerate particles using electrodynamic potentials.

The development of the betatron, the first circular accelerator named after the nuclear decay mode associated with electrons (β-decay), came from the advances made by Rolf Widerøe, creator of the first linac based on Ising's model in 1928 [10], in understanding the principles of operation and was eventually created by Max Steenback of Germany in 1935 and Donald Kerst of the United States in 1940 [11]. Figure 1.2 shows the cross-section of a betatron. Particles circulate in an evacuated toroidal tube surrounded by a magnetic yoke. A static magnetic field in the axial direction keeps the electrons circulating about the center, leading to compactness in the design. A time-varying magnetic

field in the same direction induces a strong azimuthal electric field, accelerating the electrons while they orbit.

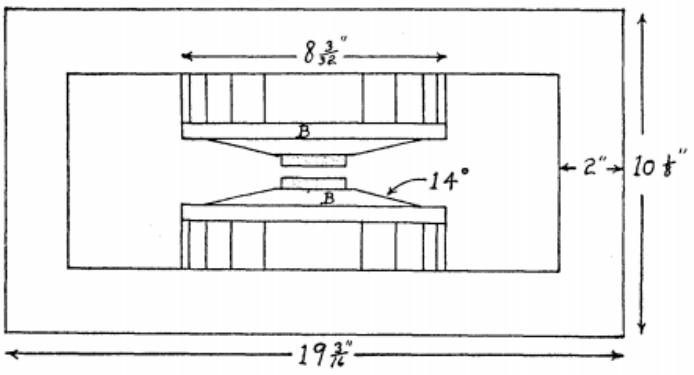

FIG. 2. Dimensions of the magnet. Parts *B* are the pole caps made with all laminations placed in a radial direction. The iron dust disks supply the central flux. Outside of the 14° conical surface a flat rim on the pole face tends to prevent too rapid decrease of the field at the edge of the gap.

Figure 1.2: Cross section of a betatron from 1941

While the device is an important part of accelerator history, advancements in radiofrequency technologies allowed for more versatile, extensible, and affordable ways of electron acceleration. Additionally, the energy scale for betatron usage was practically limited to sub-relativistic ones for electrons due to dephasing between the accelerating field and the particles when relativistic mass corrections begin to accumulate.

Once the general theory of particle acceleration was established, the task of reaching new energy regimes became one of engineering. While the primary methods were extendable, the cost scaling of the elements and labor associated with projects became a more critical task. The compactness afforded to accelerator systems by magnetic fields was generalized in new inventive designs. The synchrotron, today's primary high-energy standard, provides a magnetic field perpendicular to direction of particle acceleration to

contain its size [12]. Figure 1.3 shows a diagram for a simple synchrotron configuration [13]. The particles are inserted into the synchrotron ring at the injection site. The particles orbit in an evacuated tube with their orbital radius maintained by a transverse magnetic field pointing into or out of the page depending on charge. As the particles gain energy through RF acceleration, the magnetic field strength must increase to maintain the orbital radius. When the desired energy is reached, the particles are ejected.

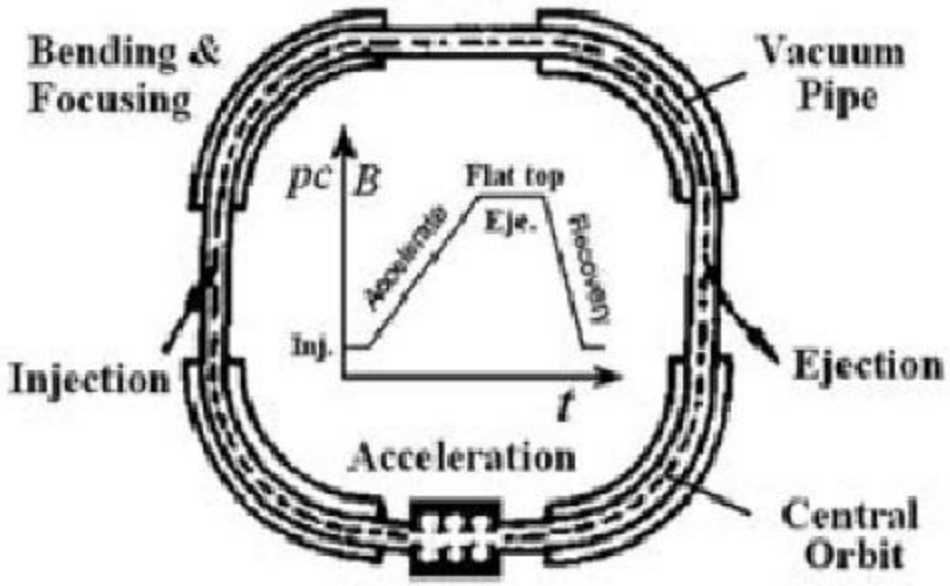

Figure 1.3: Synchrotron diagram

Two additional tools allowed accelerators to continue to advance. Microwave resonators are used for accelerating cells to provide high acceleration while maintaining dimensions required for beam clearance. A klystron amplifies radiofrequency (RF) power through electron bunch compression followed by resonant cavity coupling, allowing access to high microwave-band power. The reliability and efficiency of these systems allows them to provide pulsed or CW power consistently and affordably.

The accelerating cavities themselves need high Q factors and repetition rates to produce high-quality charged particle beams frequently. Superconducting RF (SRF) cavities have proven adept at producing high electric-field gradients with high Q factors, generating quality bunches of electrons with low power losses and high-duty cycles [14]. The high-gradient cavities also allow for fewer cavities to achieve the same acceleration, minimizing the beam instabilities caused by the accelerating structure. Figure 1.4 shows the difference in accelerating cavity shape for copper and SRF cavities. The most commonly used material for constructing SRF cavities is niobium (Nb) due to its relatively-high critical temperature of 9.3 K. An Nb SRF cavity encased in a liquid-helium bath

operating around 4.2 K can accommodate a high thermal load without losing superconductivity.

Nb SRF cavities have seen numerous improvements over the years, but the growth in the peak attainable gradient is discontinuous. Figure 1.5 shows the peak accelerating gradient of Nb SRF cavities over time. While various polishing methods and a new shape have increased the peak gradient by jumps, the progress between breakthroughs is sparse. Additionally, experts suspect that the maximum gradient is below 100 MV/m before Nb suffers from voltage breakdown, putting an upper limit on the future of the graph.

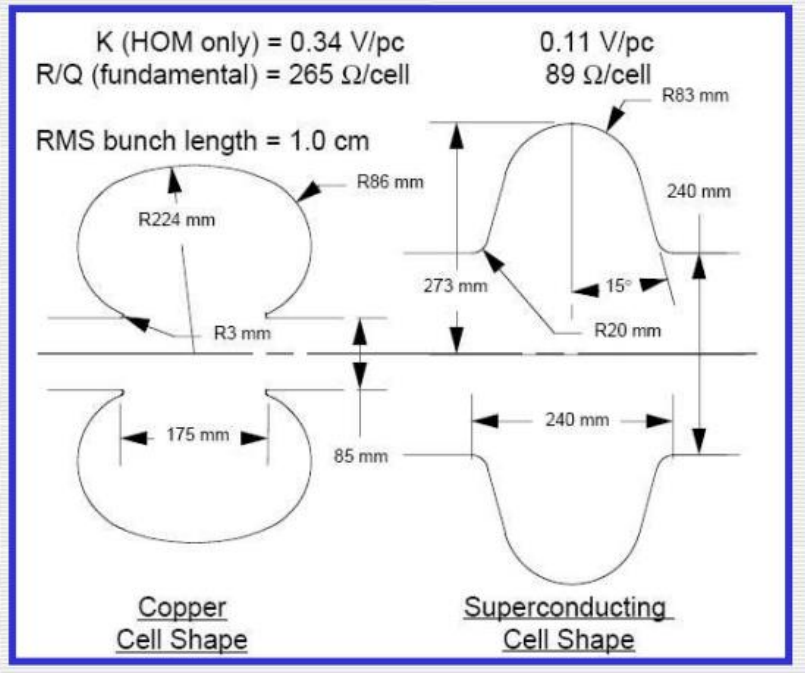

Figure 1.4: Diagram demonstrating the differences in shape and aperture width between copper (left) and superconducting (right) RF cell cavities. Ohmic power losses in copper increase as V^2, making high power expensive.

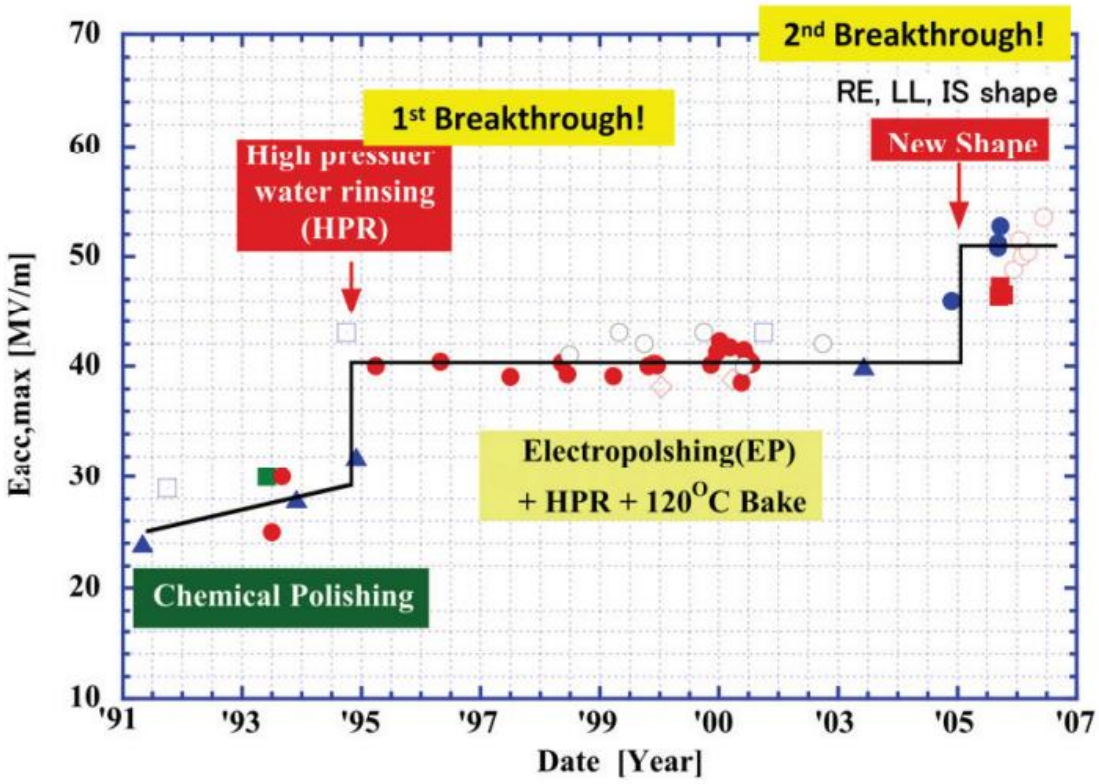

Figure 1.5: Peak Nb SRF cavity gradients versus time. The red arrows point to the jumps of significant advancement.

Most SRF cavities are operated in a regime which ensures steady beam power rather than peak field, just like a car used for transportation is capable of driving at 130 mph but rarely does so. As such, the values presented in Figure 1.5 are overestimates of practical gradients. The International Linear Collider (ILC) is an upcoming collider system which is designed to collide electrons and positrons together to achieve a collisional energy of 500 GeV. The initial design for the collider has each of the accelerating tracks composed of 7,400 1-m, 9-cell SRF cavities operating at 2 K. These cavities provide 31.5 MV/m accelerating gradients to take 15-GeV beams of electrons to 250 GeV [15]. This reduction in effective gradient means the collider length (as well as all associated costs) grows.

Figure 1.6 shows the progress in collider center-of-mass energies over the past several decades [16]. The independent axis shows the year of the accelerator beginning operation while the dependent axis plots the constituent center-of-mass energies on a logarithmic scale. A nearly linear fit is shown before the start of the 2000s, when new planned accelerators for both hadron and lepton colliders begin leveling off. The large capital investment and operational costs needed to accelerate next-generation center-of-mass-energy particles combined with the lack of drastic improvements in the SRF accelerating gradients will lower the slope of both the hadron and lepton lines for future accelerators.

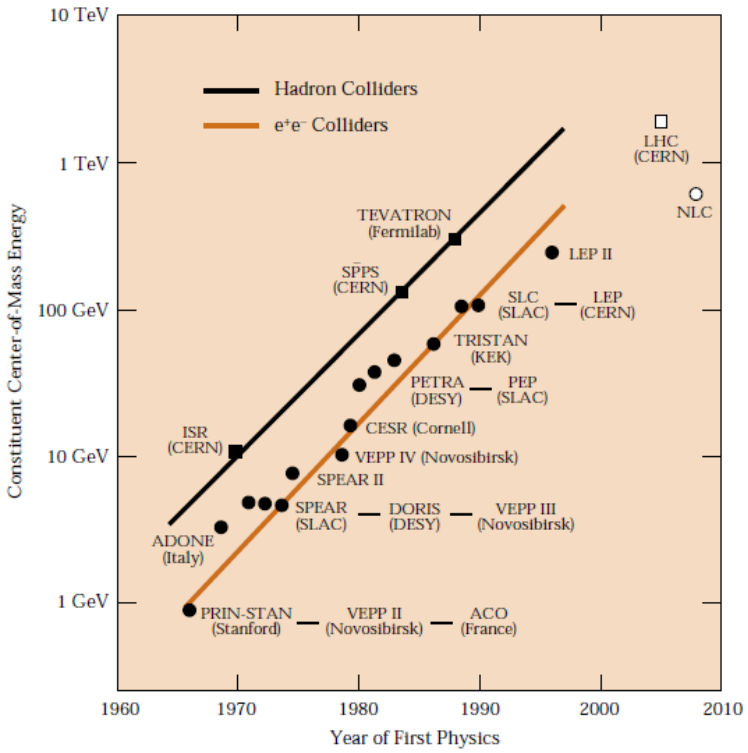

Figure 1.6: A logarithmic plot of constituent CoM energies versus year.

Beyond the high collisional energy demands, colliders also require high luminosity to increase the opportunities of observing low-probability events. The luminosity of a collider is given by the following expression [17]

$$\mathcal{L} = \frac{f N_e^2}{4\pi\sigma_\perp^2}$$

where f is the bunch repetition rate, N_e is the number of particles per bunch, and $\sigma_\perp$ is the beam radius at the collider interaction point. Luminosity this increases with higher repetition rates, more charge per shot, and more tightly focused beams.

Figure 1.## shows the luminosity as a function of center-of-mass energy. CERN's Large Electron-Positron Collider (LEP), which was operational from 1989 to 2000 and which used counter-propagating pulses of leptons at 45 GeV each to generate the Z-Boson (91 MeV/c^2), had a luminosity of 10^{32} $cm^{-2}*s^{-1}$ [18]. The ILC has a target luminosity of $1.35*10^{34}$ $cm^{-2}*s^{-1}$ [19], with discussions of potential luminosity upgrades underway. The benchmark luminosity for high-energy physics up to roughly 1 TeV is ~10^{32} $cm^{-2}*s^{-1}$.

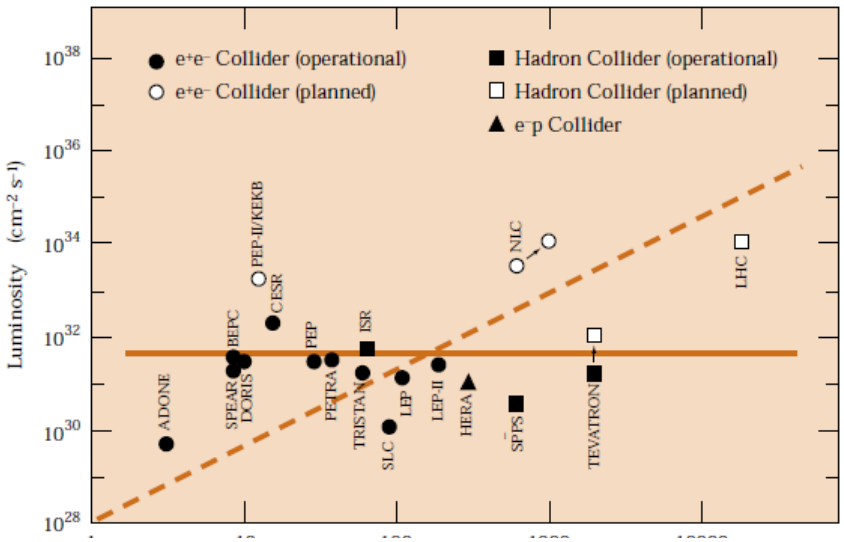

Figure 1.7: Collider luminosity vs CoM energies. The dashed line shows luminosity as the square of CoM mass.

An LWFA-driven lepton collider is perhaps the loftiest goal of the LWFA community. To achieve this goal, an LWFA system must be an electron accelerator which has both high center-of-mass energies and high luminosities at total capital investment and operational costs lower than those of a traditional SRF system (otherwise, simply using a traditional SRF system would be a safer bet). The luminosity condition requires achieving repetition rates and beam charges (final magnetic focusing methods should not change substantially) that are at least competitive with past generations of traditional lepton colliders. For reference, the LEP had a repetition rate of 11.2 kHz with beam charge of each species in the range of 10^{11} [20]. Reproducing an equivalent luminosity using LWFA technology will require judicious accelerator design choices and numerous engineering improvements.

1.2 History of Solid-State Lasers

The first laboratory laser was achieved using a 1-cm ruby rod doped with chromium (Al_2O_3:Cr) which was coated with silver on the ends and irradiated by high-power flash lamps in 1960 [21]. This achievement led to the development of lasers in many different mediums, such as gases and diodes. However, for ultrafast, high-power lasers, solid-state lasers reign as the primary tool of the trade.

As the field of laser design matured, beam energy amplification rapidly increased to the point where the pulse could damage the optical elements and amplifying medium. To allow further amplification without damaging equipment, Donna Strickland and Gerard Mourou published a paper on the chirped-pulse amplification (CPA) method in 1985 [22]. Figure 1.8 displays the configuration of their original design. CPA involves temporally stretching the pulse (using the single-mode fiber), which results in the red wavelengths

traveling in front of the blue wavelengths in the pulse. As the pulse travels through the amplifying medium, it does not reach sufficient intensities to damage the medium due to the temporal stretching. After amplification, a pair of diffraction gratings are used to compress the pulse to a much shorter duration.

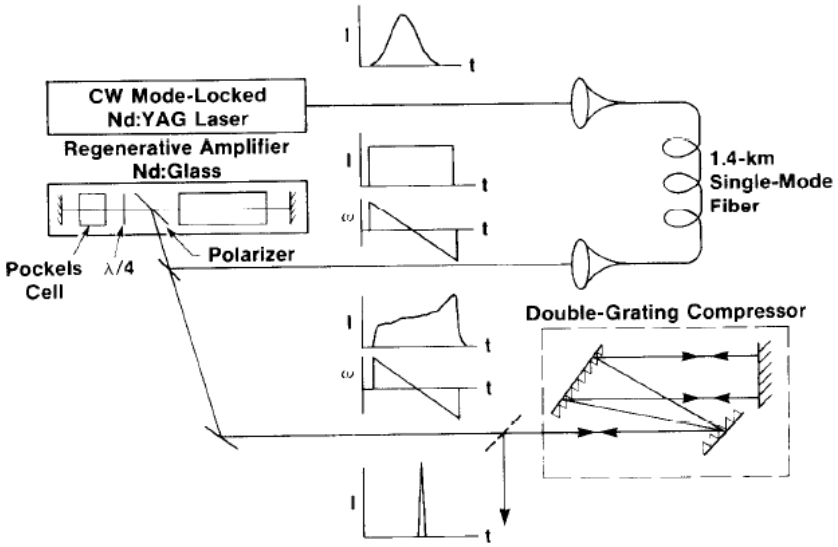

Fig. 1. Amplifier and compression system configuration.

Figure 1.8: CPA setup used by Strickland and Mourou

With the advent of CPA, achieving higher laser powers was much simpler. However, to achieve ultrafast pulses, the spectral properties of the laser pulse need to be appropriate. The time-bandwidth product of a laser determines the shortest duration it can attain, known as the transform-limited duration. Equation 1.1 expresses this quantity for a Gaussian laser pulse:

$$\Delta\omega * \Delta t = 0.441 \tag{1.1}$$

where $\Delta\omega$ is the full-width half-maximum (FWHM) of the bandwidth of the pulse in frequency space and Δt is the FWHM of the temporal duration of the pulse in time space. In order to achieve short pulses, the laser spectrum must be broad.

The search for lasing materials which produce wide-bandwidth lasers found a great candidate in Ti:Sapphire. Research begun on these materials in 1982 by Peter Moulton [23]. He discovered that the solid-state laser had a broad gain curve (spanning between 650 nm and 1,100 nm) and a large gain cross section. The gain curve allowed for pulses to reach durations as short as single femtoseconds. Additionally, the absorption wavelength range of 514 to 532 nm needed to pump the laser was achievable with other common laser systems such frequency-doubled Nd:YAG and, later, green diode lasers. These lasers are now the most common laser used for ultrafast, high-intensity research.

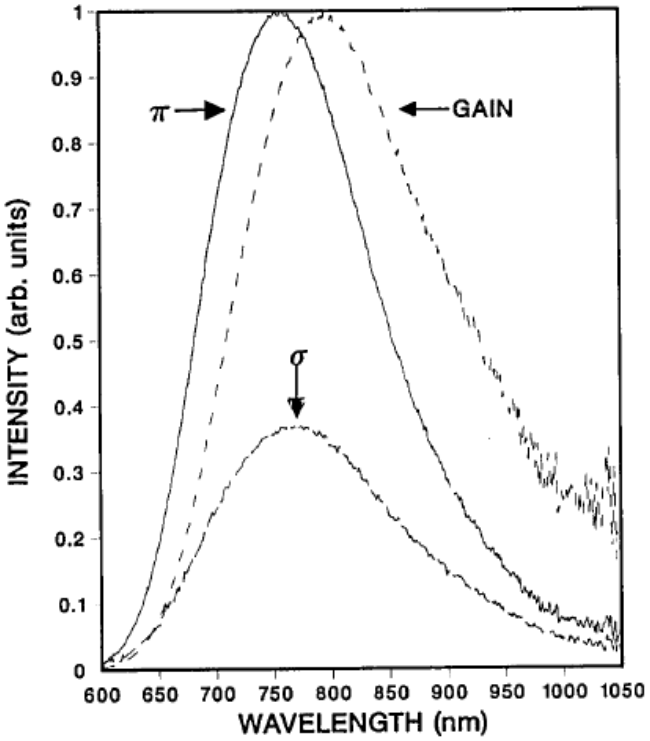

Fig. 2. Polarized fluorescence spectra and calculated gain line shape for Ti:Al_2O_3.

Figure 1.9: Measured Ti:Sapphire gain lines from Moulton's original 1982 paper

Another popular lasing material for ultrafast, high-intensity research are Nd:glass systems. Triply ionized neodymium is used as a dopant in a glass of materials such as

yttrium aluminum garnet (YAG) or yttrium lithium fluoride (YLF). Nd:glass is used in many high-power ultrafast operations due to the relative simplicity of scaling a glass system compared to a crystal system and the ability to use holographic gratings, both of which reduce costs for building high-power lasers. Nd:glass systems make up the bulk of the remaining high-power laser systems not using Ti:Sapphire, further demonstrating the dominance of solid-state lasers in ultrafast high-power physics.

Solid-state components have the advantages of being fairly stable and allowing the production of short, high-power lasers. However, as the desired power increases, the cost of larger gratings and crystals or glasses balloons quickly. Additionally, if a crystal is damaged during operation and needs replacing, realignment is required which can lead to long operational downtimes. For high-energy applications such as colliders, the stability of RF acceleration methods is critical for maintaining high uptimes necessary to observe high-energy physics' low-probability phenomena.

1.3 Laser-Electron Acceleration Mechanisms

1.3.1 The Lawson-Woodward Theorem

The general principles of accelerating an electron with electric and magnetic fields are captured in the Lawson-Woodward Theorem [24], which states that particle acceleration from electric and magnetic fields is impossible under the conditions that: 1) no static electric or magnetic fields are present, 2) the oscillating electric and magnetic fields exist in vacuum with no boundaries, 3) the region of interaction is infinite, and 4) nonlinear forces such as the ponderomotive force are neglected. The conceptual thesis of all of these conditions is that, in the absence of static forces, the physical or temporal characteristics of the electromagnetic fields must change to cause acceleration.

These criteria have a rigorous theoretical foundation and have held mostly true over time. Recent work by D. Cline, et al., demonstrated that acceleration of electrons in vacuum is possible at a laser focus due to a laser's own diffraction lowering the phase velocity of the laser [25], which is an interesting result but not one which disproves the theorem.

1.3.2 Initial Conception of the Laser-Plasma Accelerator

In the same year that Lawson published his findings, Tajima and Dawson [26] proposed that then-cutting-edge glass lasers with intensities of 10^{18} W/cm^2 could accelerate electrons in underdense plasma structures created via the ponderomotive force to maximum energies on the order of GeVs within 1 cm of propagation length. Large electric-field gradients provided acceleration several orders of magnitude greater than conventional RF methods and are not limited by material breakdown voltage. Additionally, the electron bunch duration is on the order of $\sim\lambda_p/c$, allowing the generation of femtosecond electron beams. This paper initiated a significant push for the development of laser accelerators utilizing plasma wakefields.

Individual electron motion in the presence of external electric and magnetic fields is determined by the Lorentz force law. The classic expression of this law is given by [27]

$$\boldsymbol{F_e} = \frac{d\boldsymbol{p}}{dt} = q\boldsymbol{E} + q(\boldsymbol{v} \times \boldsymbol{B}) \tag{1.2}$$

Assuming a spatially varying electromagnetic field oscillating with frequency ω, the electric and magnetic field components in vacuum are represented as such [28]:

$$\boldsymbol{E}(\boldsymbol{r}, t) = \boldsymbol{E}_0(\boldsymbol{r}) * \cos(\omega t) \tag{1.3a}$$

$$\boldsymbol{B}(\boldsymbol{r}, t) = -\boldsymbol{\nabla} \times \boldsymbol{E}_0(\boldsymbol{r}) * \frac{\cos(\omega t)}{\omega} \tag{1.3b}$$

Inserting these expressions into Equation 1.2 yields:

$$\frac{d\boldsymbol{p}}{dt} = m\frac{d\boldsymbol{v}}{dt} = q\boldsymbol{E}_0(\boldsymbol{r}) * \cos(\omega t) - q\left(\boldsymbol{v} \times \left(\boldsymbol{\nabla} \times \boldsymbol{E}_0(\boldsymbol{r}) * \frac{\cos(\omega t)}{\omega}\right)\right) \tag{1.4}$$

For electromagnetic waves acting on an electron, the momentum as expressed above will incorporate oscillations of the momentum as well as long-term positional change.

Separating the oscillatory and drift motions is possible by asserting the motion variable has a form:

$$\boldsymbol{v}(t,\tau) = \boldsymbol{V}(t) + \epsilon\boldsymbol{\zeta}(\boldsymbol{R},\boldsymbol{V}t,\tau) \tag{1.5}$$

where τ is the period of oscillation of the field, **V**(t) represents the τ-averaged **v**, and the term **ζ**(**R**, **V**t, τ) is a periodic function whose cycle average in τ is zero. The same process is possible for the position vector, **r**:

$$\boldsymbol{r}(t,\tau) = \boldsymbol{R}(t) + \epsilon\boldsymbol{\xi}(\boldsymbol{R},\boldsymbol{V}t,\tau) \tag{1.6}$$

where ε is a parameter used to characterize the different orders of terms present in the expansion. By using oscillatory terms only, the position and velocity of the electron will naturally oscillate with a frequency of ω. Similarly, the total time derivative of **r** equals **v** and the total time derivative of **R** is equal to **V**.

The time evolution of **V** can be expressed in terms of the sums of the different orders of terms in the expansion:

$$\frac{d\boldsymbol{V}}{dt} = \boldsymbol{A_0}(\boldsymbol{V},t) + \epsilon\boldsymbol{A_1}(\boldsymbol{V},t) + \epsilon^2\boldsymbol{A_2}(\boldsymbol{V},t) + \cdots \tag{1.7}$$

The change of non-oscillatory velocity is the subject of interest of this derivation.

The linear combination of oscillatory and gradual movement allows a vector Taylor expansion to be performed on both the electric and magnetic fields:

$$\boldsymbol{E_0}(\boldsymbol{r}) = \boldsymbol{E_0}(\boldsymbol{R} + \boldsymbol{\xi}) \sim \mathbf{E_0}(\boldsymbol{R}) + \epsilon(\boldsymbol{\xi} \cdot \boldsymbol{\nabla})\boldsymbol{E_0}(\boldsymbol{R}) \tag{1.8a}$$

$$\boldsymbol{B_0(r) = B_0(R + \xi) \sim B_0(R) + \epsilon(\xi \cdot \nabla) B_0(R)} \tag{1.8b}$$

Substituting these terms into the expression for momentum yields

$$m\frac{d\boldsymbol{v}}{dt} = q\big(\,\mathbf{E_0}(\boldsymbol{R}) + (\boldsymbol{\xi}\cdot\boldsymbol{\nabla})\boldsymbol{E_0}(\boldsymbol{R})\big) * \cos(\omega t) - q\left(\boldsymbol{v}\times\left(\boldsymbol{\nabla}\times\big(\,\mathbf{E_0}(\boldsymbol{R}) + (\boldsymbol{\xi}\cdot\boldsymbol{\nabla})\boldsymbol{E_0}(\boldsymbol{R})\big) * \frac{\cos(\omega t)}{\omega}\right)\right) \tag{1.9}$$

Next, this equation is converted into a form which describes the non-oscillatory motion. The lowest-order terms yield only oscillations in the electric field. Looking only at the first-order terms and remembering that the oscillatory motion is much faster than the central motion, **v** on the right-hand side being replaced by **ζ,** and the $\mathbf{E_0(R)}$ term being omitted, the resulting equation looks like

$$m\frac{d\boldsymbol{V}}{dt} = \langle q\big(\,(\boldsymbol{\xi}\cdot\boldsymbol{\nabla})\boldsymbol{E_0}(\boldsymbol{R})\big) * \cos(\omega t) - q\left(\boldsymbol{\zeta}\times\left(\boldsymbol{\nabla}\times\mathbf{E_0}(\boldsymbol{R}) * \frac{\cos(\omega t)}{\omega}\right)\right)\rangle \tag{1.10}$$

Through taking the cycle average, the application of common vector identities, and the conversion to a more familiar nomenclature, the final result is

$$\frac{d\boldsymbol{p}}{dt} = -\frac{e^2}{4m_e\omega_l^2}\nabla\,\overline{E^2} \tag{1.11}$$

where **p** is the electron momentum vector, e is the electron charge, m_e is the electron mass, ω_l is the laser frequency, and **E** is the laser electric field. The right-hand term is an expression for the ponderomotive force, which depicts the tendency of charged particles to migrate from high-field to low-field areas over the course of a single laser oscillation. This equation holds while the peak normalized laser amplitude, a_0, is less than one [29]. An expression for a_0 is:

$$a_0 = \frac{eE}{cm_e\omega_l} = 8.54 * 10^{-10}[\lambda(\mu m)]\left[I_0\left(\frac{W}{cm^2}\right)\right]^{\frac{1}{2}} \tag{1.12}$$

Here, λ is the laser wavelength and I_0 is the laser intensity.

When generalizing to the relativistic regime ($a_0 >> 1$), if the paraxial approximation is not used, the expression for the ponderomotive force becomes [30]:

$$\frac{d\boldsymbol{p}}{dt} = -\frac{m_e c^2}{2\langle\gamma\rangle}\nabla\langle a^2\rangle \tag{1.13}$$

where γ is the relativistic correction factor of the electrons due to the laser field and the brackets indicate a time average is taken. The expression for the relativistic correction factor related to electron motion is expressible using the normalized laser amplitude:

$$\gamma^2 = 1 + \frac{a_0^2}{2} \tag{1.14}$$

1.3.3 Early Methods of Laser-Plasma Acceleration

I will describe the development of laser-plasma accelerators (LPAs) as an evolution through three stages of development related to the pump pulse duration [29]: 1) plasma beat-wave methods to circumvent the lack of sufficiently short pump pulses, 2) self-modulated laser wakefields, where pulse lengths shorten, but are still substantially longer than a single plasma wavelength, and 3) "bubble-regime" laser wakefield, where the pump pulse length is close to the plasma wavelength. Although historically LPAs did not develop monotonically from one stage to the next, this outline is useful to depict how the field evolved as the duration of pulses shrank.

A practical method for achieving electron acceleration from plasma oscillations was mentioned by Tajima and Dawson in their original paper. Plasma beat-wave acceleration (PBWA) uses two lasers with long pulses durations and frequencies ω_1 and ω_2 such that:

$$\omega_1 - \omega_2 \sim \omega_p \tag{1.15}$$

By carefully offsetting these two pulses in time, the resulting electromagnetic wave packet takes the form of multiple pulses at the plasma frequency. Clayton, et al., [31] demonstrated the first plasma wave excitation using a beat-wave laser between two CO_2 lasers at 10.6 and 9.57 μm. The two 2-ns pulses had 12 and 4 J respectively and were focused using an f/7.5 optic into 1 Torr of pre-ionized hydrogen gas of approximately 10^{17} cm^{-3}. Measurements of the plasma frequency were made using a 7.5-degree ruby collective Thomson scattering laser. The measured wakefield amplitude of 1-3% produces potential gradients as high as 1 GV/m, confirming Tajima and Dawson's original theory.

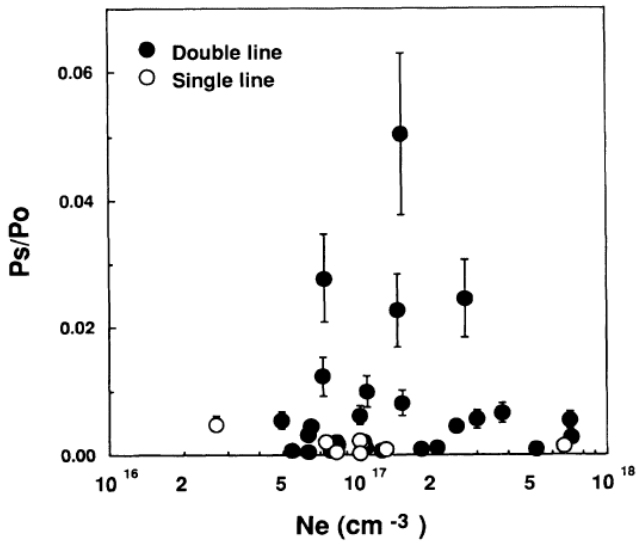

Figure 1.10: CTS probe light ratio as a function of density. The peak signal is indicative of a high-amplitude plasma wake, which scatters high-order CTS shifts more efficiently.

Kitagawa, et al., [32] used a CO_2 system with 150-J pulses of the same laser lines as Clayton accelerated electrons to between 10 and 21 MeV using a hydrogen gas plasma with density 1.1e17 cm^{-3}. The spectrum of accelerated electrons reflects a Boltzmann

distribution of energies, with an exponentially decaying high-energy tail. Estimates of the plasma interaction length as well as the powers of the initial pump pulse and final Stokes-scattered pump light predicted a plasma wake amplitude as high as five percent (Figure 1.10). (For those unfamiliar with the Forward Raman Scattering instability and its characteristic effects on lasers in plasmas, see section 4.1 on collective Thomson scattering.)

While these initial successes were encouraging, there were several shortcomings of the method. The beat wave's frequency is fixed for a particular experimental configuration, yet the plasma wave period increases as the wave becomes relativistic, limiting the ultimate amplitude of the wave unless specifically tuned to compensate for the dephasing. Laser-plasma instabilities can also leech significant amounts of energy from the plasma wake. Most significantly, however, the advent of Ti:Sapphire lasers made shorter pulses with relativistic intensity more readily available, overtaking an interesting but inefficient technique.

1.3.4 Self-Modulated Laser Wakefields

As pulse durations begin to shorten, the self-modulated wakefield regime becomes available for a given laser. Self-modulated wakefields require that the pulse duration is longer than plasma wavelength ($c\tau_{laser} > \lambda_{plasma}$) and the pulse power is greater than the critical power for self-focusing ($P > P_c$) [33]. When focused into a gas jet, the rising edge of the pulse ionizes the medium to create a plasma. Random noise within the plasma density distribution seeds the modulation instability, which causes the plasma wake to efficiently gain energy from the laser. Due to longitudinal ponderomotive forces and the axial variation of the plasma density, the laser pulse becomes $\pi/2$ out of phase with the plasma

wave, leading to resonant excitation of the wave. The plasma wake structure's wavelength leads to oscillations shorter than the pulse duration, which extracts energy from the laser most efficiently on the slopes of the oscillations. The result is that the laser pulse has the modulations imprinted on it with the characteristic wavelength of the plasma wake. These oscillations are capable of capturing electrons, which are then carried with the wake as it moves. The electron energy spectrum has a similar Boltzmann distribution. A more thorough and mathematical treatment of this process is described in section 1.4.

Experimental evidence confirmed the capability of self-modulated laser wakefields to produce MeV electrons. Joshi, Tajima, Dawson, et al., observed the acceleration of electrons from self-modulated laser wakefields back in 1981 [34]. A 130-Å-thick carbon foil was irradiated by 700-ps, 10^{15} W/cm^2 CO_2 lasers, ejecting electrons with energies of 1.4 MeV.

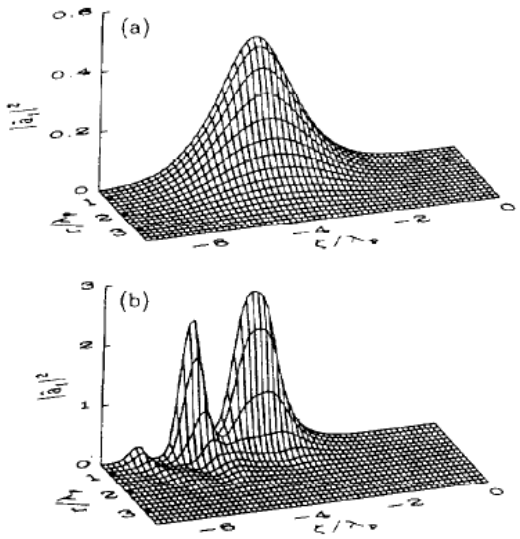

Figure 3: Laser intensity $|\hat{a}_f|^2$, sampled over a coarse grid (the numerical grid is much finer), at (a) $c\tau = 2Z_R$ and (b) $c\tau = 3.2Z_R$. The laser pulse is moving towards the right.

Figure 1.11: The evolution of the laser profile as it undergoes self-modulation [35]

An outline of the physics of a self-modulated laser wakefield electron accelerator was drawn by Krall, et al., using laser-plasma fluid simulations in 1993 [35]. Modena, et al., [36] were able to generate electrons with energy in excess of 44 MeV using a 1.054-um laser with intensity greater 5e18 W/cm^2 and pulse length less than 1 ps. The output laser spectrum demonstrated numerous Stokes and anti-Stokes plasma shifts. Characterization of the output light of collective Thomson-scattered light by Ting [37] and Le Blanc [38] measured the persistence of wakes in time at several ps, both measuring electrons with energies in the single digits of MeVs with Ti:Sapphire systems.

As an intermediate step, self-modulated laser wakefield acceleration was a certifiable success. It required much less energy to achieve significant electron energies using modern laser technology. Since the plasma wavelength is required to be smaller than the pulse duration, large densities are usable, resulting in a large axial electric field, since the maximum sustainable field is given by [29]:

$$E_z\left(\frac{V}{m}\right) = 96\sqrt{n_0(cm^{-3})} \tag{1.16}$$

Still, numerous instabilities made shot-to-shot variation large in terms of electron output and the output energy spectrum produced few high-energy electrons. Similar to the plasma beat-wave accelerator, the self-modulated laser wakefield accelerator was eventually outclassed by advances in pulse length reduction.

1.3.5 Bubble-Regime Laser Wakefields

As was previously derived in 1.3.2, the ponderomotive force in a plasma pushes electrons from regions of high intensity to regions of low intensity in time-varying electromagnetic fields. Increasing the strength of the ponderomotive force results in the

eventual expulsion of all the electrons present in the laser field. In order to achieve this result, the ponderomotive force must balance the Coulomb force of the relatively stationary ions in the plasma:

$$F_{pm} = -\frac{e^2}{2m_e\omega_p^2}\nabla\,\overline{E^2} = \frac{\rho_{ion}V_{ex}}{4\pi\epsilon_0 r^2} \tag{1.17}$$

where V_{ex} is the volume of the expulsion region, ρ_{ion} is the ion density, and r is the radius of the expulsion region. This cavitation of the region is known as a plasma "bubble", which travels along with the plasma wave. Electrons which fall into the bubble become trapped in the back section of the cavity (a process known as self-injection), experiencing an accelerating force from the ions as long as they remain behind the center of the bubble, which propagates at the laser pulse's group velocity.

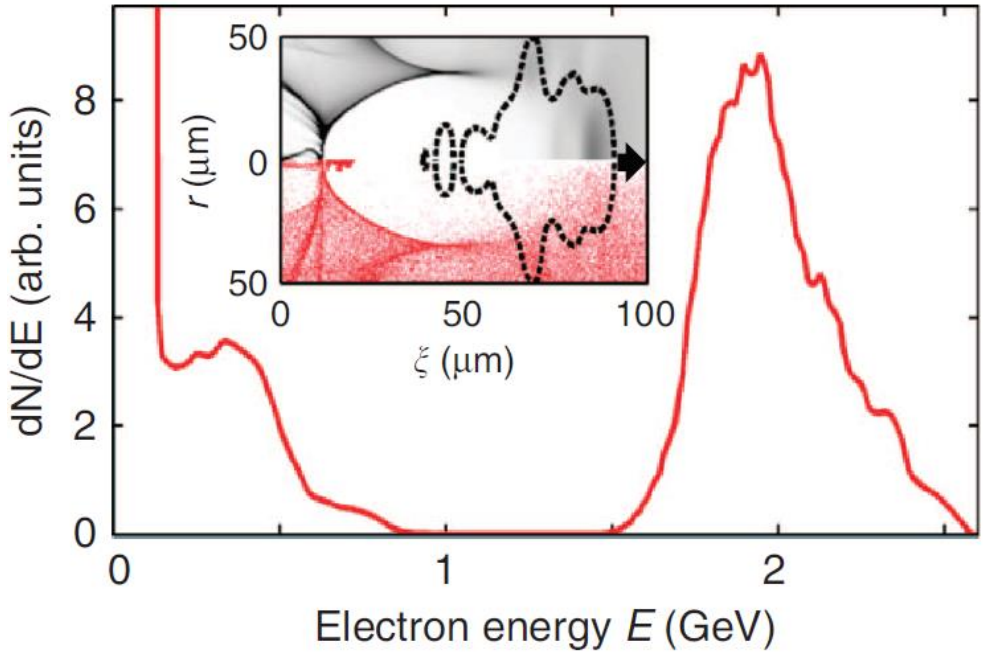

Figure 1.12: Electron spectrum from Wang, et al., demonstrating 2-GeV electron acceleration using a PW-class laser. Inset: electron density profile showing black background electrons and red test electrons in the bubble.

This process has proven capable of creating nearly monoenergetic electron beams up to GeV energies over small distances [39]. Wang, et al., [40] used 150-fs, 150-J, 1.057-μm laser pulses with a f/47 optic in a 7-cm-long helium gas cell. 2-GeV electrons were generated in a plasma with a density of $4.8*10^{17}$ cm^{-3} by a pulse with $a_0 \sim 8$. The corresponding electric field gradient was estimated at 2 GV/cm, thirty-three times larger than the peak gradient achievable by Nb SRF cavities and sixty-six times larger than the operational gradients planned for the ILC. This experiment is a proof of concept of the potential for LWFA to accelerate leptons to collider-level energies.

1.4 Laser-Matter Interactions

1.4.1 Laser Propagation and Self-Focusing

For a laser propagating in neutral gas, the pulse focuses from the introduction of focusing elements in the path and defocuses due to diffraction [41]. While the pulse is below critical power and ionization intensities, the majority of the spatial evolution is dictated by these basic elements plus dispersion, which is small for gaseous densities.

Here I will describe the propagation of a pulse of Gaussian transverse spatial profile. The reason for its use is quite practical. The scalar wave equation has the following form:

$$\nabla^2\psi(\boldsymbol{r},t) - \frac{1}{c^2}\frac{\partial^2\psi}{\partial t^2} = 0 \tag{1.18}$$

where $\psi(\mathbf{r},t)$ is a scalar solution to the source-free wave equation [42]. The expression can be found for individual constant frequencies by taking the Fourier transform of the solutions of the scalar Helmholtz equation:

$$(\nabla^2 + k^2)\psi(\boldsymbol{r},\omega) = 0 \tag{1.19}$$

where ω is the frequency of interest. The spherical-coordinate-system decomposition of the angular and radial components of the scalar expression results in the spherical harmonics times spherical Bessel and Hankel function solutions. The Gaussian beam is the transverse electromagnetic (TEM) mode with m = n = 0, which is obtainable from a multipole expansion of the electric and magnetic fields. A more efficient and intuitive solution is presented below [43].

Starting from the vector Helmholtz equation, which describes the propagation of a component of a wave, the beam propagation equation must satisfy:

$$\nabla^2 \boldsymbol{X} + k^2 \boldsymbol{X} = 0 \tag{1.20}$$

where the vector **X** represents either the electric field or magnetic field. The Helmholtz equation assumes separation of variables into spatial and temporal components, allowing solutions to each part individually. Focusing only on the spatial variation, one transverse component of the electric field can be written as follows:

$$E(x, y, z) = u(x, y, z) * e^{-ikz} \tag{1.21}$$

where u(x,y,z) is a spatially varying function, i is the imaginary unit, and k is the wave vector determined by the wavelength of the component. Note that, due to function u's dependence on x and y, this expression allows for variation in the transverse dimensions unlike a plane wave solution. By plugging in Eq. 1.20 into Eq. 1.21, the reduced wave equation is constructed:

$$\frac{\partial^2 u}{\partial x^2} + \frac{\partial^2 u}{\partial y^2} + \frac{\partial^2 u}{\partial z^2} - 2ik\frac{\partial u}{\partial z} = 0 \tag{1.22}$$

At this point, two assumptions are made to simplify the above expression. First, the variation in u along z is assumed to be small over the distance of a wavelength:

$$\frac{\partial^2 u}{\partial z^2} \ll 2k\frac{\partial u}{\partial z} \tag{1.23}$$

Second, the axial variation is assumed small compared to the transverse variation:

$$\frac{\partial^2 u}{\partial z^2} \ll \frac{\partial^2 u}{\partial x^2}, \frac{\partial^2 u}{\partial y^2} \tag{1.24}$$

These two assumptions allow the curvature of u in the direction of z to be neglected:

$$\frac{\partial^2 u}{\partial x^2} + \frac{\partial^2 u}{\partial y^2} - 2ik\frac{\partial u}{\partial z} = 0 \tag{1.25}$$

Ignoring the second derivative of u in z is known as the paraxial approximation and the above equation is known as the paraxial wave equation. The solutions to this equation are quite close to the real solutions for divergences less than 30 degrees and beam waists larger than the order of a wavelength or smaller.

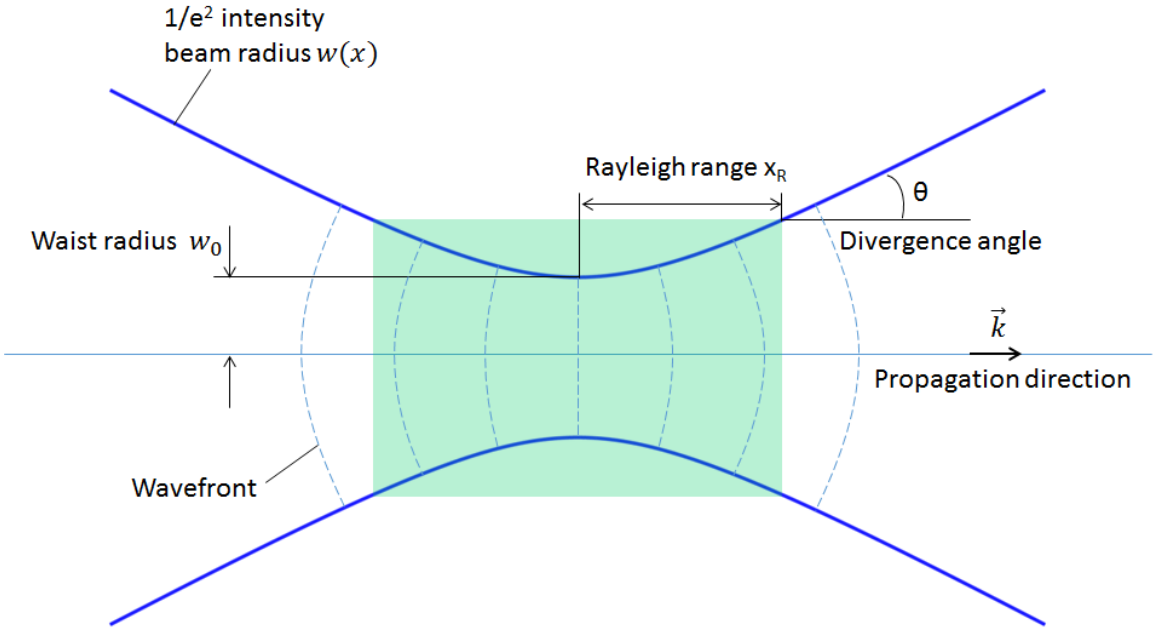

Figure 1.13: Focusing of a Gaussian beam. The blue line outlines the $1/e^2$ intensity, the other common metric beside full-width half-maximum. The beam waist, w_0, is the smallest radius of the beam and is achieved at the focus.

The mathematical descriptions of numerous characteristics of Gaussian beams are simple and convenient. The beam diameter has the following expression for its growth relative to its beam waist, the location of smallest diameter:

$$w(z) = w_0\sqrt{1+\left(\frac{\lambda z}{\pi w_0^2}\right)^2} = w_0\sqrt{1+\left(\frac{z}{z_R}\right)^2} \tag{1.26}$$

Here, w_0 is the beam waist, z is the propagation distance, λ is the laser wavelength, and z_R is the Rayleigh range for the pulse (the distance the pulse propagates in which the beam cross section doubles in size). For reference, the Rayleigh range is defined as:

$$z_R = \frac{\pi w_0^2}{\lambda} \tag{1.27}$$

The radius of curvature of the beam is expressed in a similar expression:

$$R(z) = z * \left(1+\left(\frac{z_r}{z}\right)^2\right) \tag{1.28}$$

which has the limiting behavior of being flat at the beam waist. The curvature is particularly useful for comparing the optical power of focusing elements, defined as [44]:

$$P_{optical} = \frac{1}{f} = \frac{2}{R} \tag{1.29}$$

For two thin lenses, the total optical power is the sum of the positive optical powers minus the sum of the negative optical powers.

The index of refraction in a neutral gas dictates the phase speed of a pulse propagating within the medium [41]:

$$n = n_0 + n_2 * I \tag{1.30}$$

where n_0 is the index of refraction of light in the medium, n_2 is the nonlinear refractive index caused by the $\chi^{(3)}$ property of the medium which has units of cm^2/W, and I is the laser intensity.

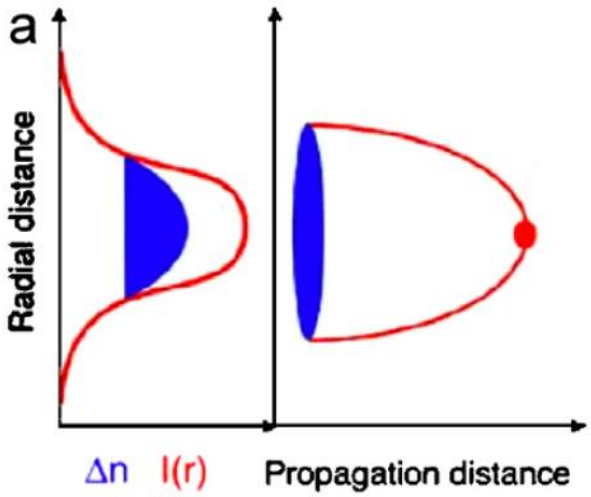

Figure 1.14: A demonstration of self-focusing. The pulse originally has a Gaussian transverse profile, leading to a varying refractive index across it. After propagating some distance, the transverse profile has shrunk. [51]

For low intensities, the second term has little effect on the propagation dynamics. As I increases, the spatial intensity variation across the pulse becomes more pronounced and causes the peak intensity region of the pulse to slow relative to the less intense parts. The result of the slower central region and Huygens' principle are the focusing of the light in the medium. A derivation of these dynamics will now be presented following [45].

Assume a laser has a Gaussian transverse intensity profile:

$$I(r) = I_0 * e^{-2\left(\frac{r}{w}\right)^2} \tag{1.31}$$

where I_0 is the peak intensity, r is the radial point of interest, and w is the beam width at a given z-position. The phase of the light has a transverse profile as well, which is dependent on the frequency of the light as well as the index of refraction:

$$\phi(t) = \omega * t - \omega * \frac{z}{c} * (n_0 + n_2 * I(r)) \tag{1.32}$$

where ω is the frequency of the light, z is the propagation distance from a known starting point, and t is the time elapsed. By combining Eqs. 1.31 and 1.32 and subtracting the value of the phase at an infinity radius (i.e., $n_0 + n_2*I$ becomes n_0), the radial variation of the phase is found:

$$\Delta\phi(r,z) = \omega * \frac{z}{c} * n_2 * I_0 * e^{-\frac{2r^2}{w^2}} \tag{1.33}$$

Note that this value represents that phase *lag* of the region, so the sign of the expression is positive compared to Eq. 1.32.

At this point, a brief aside to provide expressions for phase and group velocity is appropriate. The equation for the phase speed of an EM wave in vacuum is [46]:

$$c = \lambda\nu \tag{1.34}$$

where ν is the frequency. In a medium other than vacuum, the index of refraction dictates the change of the speed of light by modifying the wavelength:

$$v_\phi = \frac{\lambda}{n}\nu = \frac{c}{n} \tag{1.35}$$

Common expressions for the angular frequency and the wave vector are also known:

$$\omega = 2\pi\nu \tag{1.36a}$$

$$k = \frac{2\pi}{\lambda} \tag{1.36b}$$

Combining these yields an alternative expression for the phase velocity:

$$v_\phi = \frac{\omega(k)}{k} = \frac{c}{n(k)} \tag{1.37}$$

The group velocity is found from the derivative of ω with respect to the wave vector:

$$v_g = \frac{d\omega}{dk}|_{k_0} \tag{1.38}$$

By differentiating Eq. 1.37 with respect to ω, the expression for the group velocity of a wave packet becomes [47]

$$v_g = \frac{c}{n(\omega) + \omega \frac{dn}{d\omega}} \tag{1.39}$$

In regions where the refractive index does not change rapidly with frequency (i.e., if the group velocity does not change with frequency), the phase velocity and group velocity are almost identical. However, they describe different behaviors. Phase front dynamics are dictated by phase velocity, since it considers constructive interference of electromagnetic fields originating from different locations. Group velocity documents that transportation of energy and information. When interference effects are relevant, the phase velocity is considered. When interested in the movement of the electromagnetic energy, the group velocity is discussed.

If the phase delay across the beam is significant, it can overtake diffraction and lead to a shrinking beam area. This effect is known as self-focusing. A characteristic power, known as the critical power (P_{cr}), determines the onset of the self-focusing of a laser. P_{cr} is found by calculating the pulse power necessary for the optical power of self-focusing to be greater than the optical power of diffraction:

$$P_{optical} = \frac{2}{R_{SF}} - \frac{2}{R_{Diffraction}} \geq 0 \tag{1.40}$$

Rewritten in terms of the radii

$$R_{SF} \leq R_{Diffraction} \tag{1.41}$$

For the radius of diffraction, Eq. 1.29 is used. For the radius of self-focusing, the spatial shift is caused by phase retardation is computed. For a given curve in Cartesian coordinates y(x), the radius of curvature is expressed as:

$$R = \left| \frac{(1 + y'^2)^{\frac{3}{2}}}{y''} \right| \tag{1.42}$$

The equation which expresses the phase curve of the laser pulse with a radially varying intensity in a medium is found via the difference between the propagation distance at infinite radius and the propagation distance of the central regions:

$$\Delta s(r,z) = v(I) * t - v_0 * t = \left(\frac{c}{n(I)} - \frac{c}{n_0}\right) * t \tag{1.43}$$
$$= \frac{ct}{n_0 + n_2 * I}\left(1 - \frac{n_0 + n_2 * I}{n_0}\right) = -\frac{ct}{n_0 + n_2 * I}\frac{n_2}{n_0} * I_0 * e^{-\frac{2r^2}{w^2}}$$

Note that the first term in the final expression can be rewritten in terms of the propagation distance given that $\frac{ct}{n(I)} = v_\phi t \approx z$. This conversion as well as an expansion of the exponential term leads to the following expression for the phase curve:

$$\Delta s(r,z) = -z * \frac{n_2}{n_0} * I_0 * \left(1 - \frac{2r^2}{w^2}\right) \tag{1.44}$$

Now derivatives of the expression are taken with respect to radius to find the expressions in Eq. 1.42:

$$\Delta s(r,z)' = z * \frac{n_2}{n_0} * I_0 * \left(\frac{4r}{w^2}\right) \tag{1.45a}$$

$$\Delta s(r,z)'' = z * \frac{n_2}{n_0} * I_0 * \left(\frac{4}{w^2}\right) \tag{1.45b}$$

Combining Eqs. 1.45a and 1.45b into Eq. 1.42 terms yields:

$$R_{SF} = \left| \frac{\left(1 + \left(z * \frac{n_2}{n_0} * I_0 * \left(\frac{4r}{w^2}\right)\right)^2\right)^{\frac{3}{2}}}{z * \frac{n_2}{n_0} * I_0 * \left(\frac{4}{w^2}\right)} \right| \tag{1.46}$$

Evaluating this expression at center of the pulse (i.e., r = 0) reduces it to:

$$R_{SF} = \frac{w^2 n_0}{4 I_0 n_2 z} \tag{1.47}$$

Plugging Eqs. 1.28 and 1.47 into Eq. 1.41:

$$\frac{w^2 n_0}{4 I_0 n_2 z} \leq z * \left(1 + \left(\frac{z_r}{z}\right)^2\right) \tag{1.48}$$

For small propagation distances in a medium with index of refraction n_0, the right-hand expression of Eq. 1.48 becomes:

$$z * \left(1 + \left(\frac{z_r}{z}\right)^2\right) \approx z * \left(\frac{z_r}{z}\right)^2 = \frac{\pi^2 w_0^4 n_0^2}{\lambda_0^2 z} \tag{1.49}$$

The final expression comparing radii of curvature is then:

$$\frac{w_0^2 n_0}{4 I_0 n_2 z} \leq \frac{\pi^2 w_0^4 n_0^2}{\lambda_0^2 z} \tag{1.50}$$

or, alternatively:

$$\frac{n_0}{4 I_0 n_2} \leq \frac{(\pi^2 w_0^2 n_0^2)}{\lambda_0^2} \tag{1.51}$$

By recognition that the power of a pulse is expressible by beam waist and intensity, the conversion to power is straight forward:

$$P_{cr} \leq P \tag{1.52a}$$

$$\frac{\lambda_0^2}{8\pi n_0 n_2} \leq \frac{\pi w_0^2 I_0}{2} \tag{1.52b}$$

Additional considerations for beam shape modify this expression slightly, multiplying the left-hand side of Eq. 1.52b by a constant α based on the beam shape. For Gaussian beams, α is approximately 1.8962. The final expression for critical power is:

$$P_{cr} = \frac{\alpha \lambda_0^2}{8\pi n_0 n_2} \tag{1.53}$$

Figure 1.14 demonstrates the behavior of a pulse with $P > P_{cr}$ as it propagates.

1.4.2 Ionization, Additional Focusing Effects, and Wakefield Generation

As the pulse power increases, either through higher pulse energy or self-focusing, the pulse reaches ionization intensities (~10^{14} W/cm^2 for gaseous hydrogen) [48]. The Keldysh tunneling parameter helps to demarcate non-resonant tunneling ionization, which

dominates at high intensity, from non-resonant multiphoton ionization, which dominates at low intensity. The Keldysh parameter is [49]

$$\gamma = \sqrt{\frac{U_{ion}}{2U_{pond}}} \tag{1.54}$$

where U_{ion} is the ionization potential of hydrogen gas (13.6 eV) and U_{pond} is the ponderomotive energy of the pump pulse. Keldysh's parameter can also be expressed as the ratio of the tunneling time to twice the laser oscillation period [50]. Both expressions provide an intuitive understanding of what the parameter is measuring: how difficult it is for a bound electron to escape its atom while under the influence of the laser pulse.

The equation for U_{pond} is:

$$U_{pond} = \frac{e^2 I}{2c\epsilon_0 m_e \omega^2} \tag{1.55}$$

where e is the electron charge, ε_0 is the vacuum permittivity, m_e is the electron mass, and ω is the laser angular frequency. For Keldysh parameters much larger than 1, the primary ionization mechanism is multiphoton ionization, in which photons are simultaneously absorbed to overcome the Coulomb barrier [51]. For Keldysh parameters much less than 1, the Coulomb barrier is suppressed by the pulse field, allowing electrons to tunnel through the barrier within a half-cycle. For the experimental work in this thesis, which used a CO_2 pump laser with an f-number of 3 and energy between 1 and 5 J (2e16 to 10e16 W/cm^2), the Keldysh parameter is between 0.0026 and 0.0057, solidly in the tunneling ionization region. Under these conditions, the tunneling time is nearly one thousand times shorter than

the laser oscillation period. It is safe to assume that plasma is fully ionized at the peak of the pump pulse.

After ionization of a gaseous medium, the laser propagates through a plasma. The electrons in a plasma will have a characteristic oscillation frequency based on its density

$$\omega_p = \sqrt{\frac{n_e e^2}{\epsilon_0 m_e}} \tag{1.56}$$

where n_e is the electron number density [52]. In a plasma, electromagnetic waves are subject to the plasma dispersion relationship [53]:

$$\omega^2 = \omega_p^2 + c^2 k^2 \tag{1.57}$$

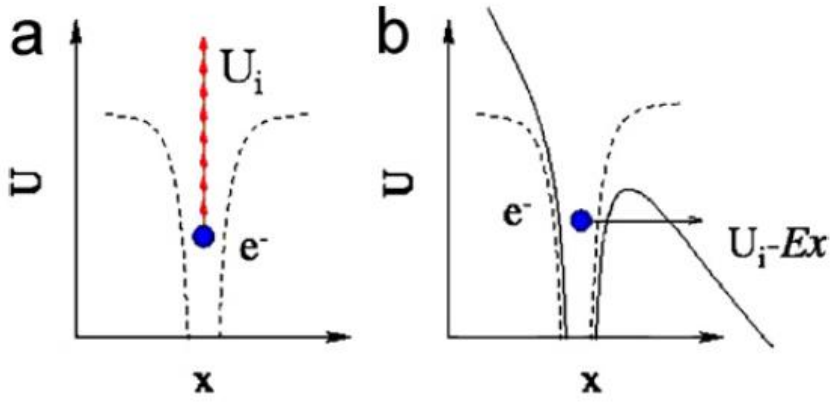

Figure 1.15: a) Multiphoton ionization, and b) tunnel ionization

Any electromagnetic wave with a frequency below this value will require an imaginary wave vector. This occurs because free electrons can move fast enough to screen low-frequency light, preventing it from propagating. Conversion of k from real to imaginary means that a propagating wave of the form $e^{i*Re(k)*z}$ becomes an exponentially attenuating wave $e^{-Im(k)z}$. The density at which this occurs is called the critical density (n_{cr}). Plasmas

which have characteristic frequencies less than the laser frequency of the pulse which is bombarding it are called underdense plasmas.

The phase and group velocities of electromagnetic waves in a plasma are found from the plasma dispersion relation:

$$v_\phi = \frac{\omega}{k} = \frac{c}{\sqrt{1 - \frac{\omega_p^2}{\omega^2}}} \tag{1.58}$$

$$v_g = c\sqrt{1 - \frac{\omega_p^2}{\omega^2}} \tag{1.59}$$

Both phase and group velocity approach the vacuum speed of light for $\omega >> \omega_p$.

The change of a medium from neutral gas to ionized plasma changes its refractive index. Using Eq. 1.58, a plasma refractive index takes the form:

$$\eta = \frac{c}{v_\phi} = \sqrt{1 - \frac{\omega_p^2}{\omega^2}} \tag{1.60}$$

The same radial intensity variation that caused self-focusing in a neutral gas can cause additional focusing effects in a plasma, i.e. ponderomotive self-focusing, as the laser-plasma interaction becomes relativistic.

A complete description of the spatio-temporal dynamics inherent in ponderomotive self-focusing is difficult, but a general description is possible. Strong ponderomotive effects eject electrons from the sloped region of the pulse, causing radial variation of the plasma density. At steady state, the electron density will have transverse shape [54]

$$n_e(r) = n_{e_0} * e^{-\frac{e^2|\boldsymbol{E}(r)|^2}{m\omega^2 T_e}} \tag{1.61}$$

where n_{e0} is the original unperturbed electron density of the plasma, $\mathbf{E}(r)$ is the electric field as a function of radius, and T_e is the electron temperature. This cavitation of electrons from the ponderomotive force will cause the plasma frequency to drop at the highest laser intensity regions. Since the index is one minus the ratio of the local density divided by the

square of the laser angular frequency, the index is largest in highest intensity regions just as it was for self-focusing in a neutral medium. The consequence is a focusing of phase fronts towards the propagation axis.

Note that even this simplified situation becomes complicated quickly because, simultaneously, the group velocity of the center of the laser becomes larger in a region of smaller plasma density. This leads to the central energy moving faster than the sides while the phase fronts begin to focus. Full consideration of the focusing effects involves detailed computation of all these spatio-temporal components, as well as plasma instabilities and laser-plasma energy transfer modes.

In addition to ponderomotive effects, relativistic effects can start to influence the local plasma frequency. As was displayed in Eq. 1.61, high laser intensities can lead to relativistic corrections to the electron mass, decreasing the effective density and consequently the plasma frequency itself. The relativistic corrections on-axis will be larger than those off-axis, causing a modification to the index of refraction similar to ponderomotive self-focusing. The interplay of these two effects further complicates a clean description of the dynamics of the pulse. An alternative and more convenient estimate of critical power for the onset of relativistic self-focusing comes from G. Z. Sun, et al. [55]:

$$P_{cr} \approx 17\left(\frac{\omega}{\omega_p}\right)^2 GW \tag{1.62}$$

Figure 1.16 shows diagrams of relativistic and ponderomotive self-focusing. It is useful for the first-time reader to better understand the details of the processes.

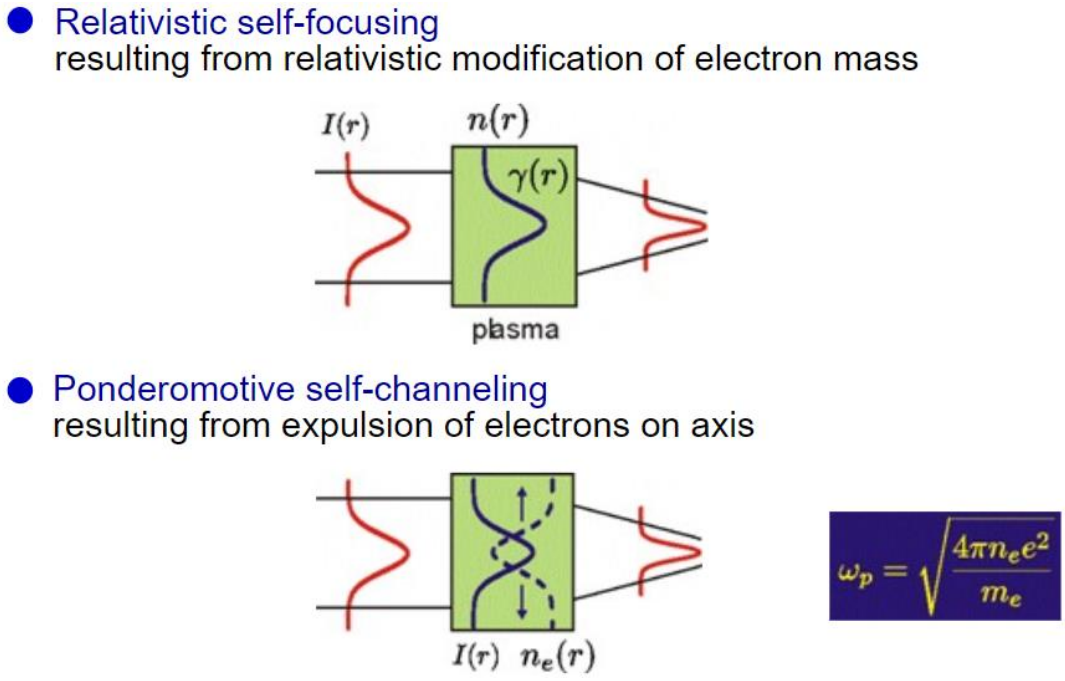

Figure 1.16: Diagrams of relativistic and ponderomotive self-focusing

Chapter 2: Self-Modulated Laser Wakefields

The conditions necessary to sustain a self-modulated laser wakefield are discussed in this chapter. Subsequently, the broad details of the plasma wave and laser pulse evolution are mentioned before touching upon the electron acceleration mechanism. Estimates for the electron energy gain are calculated. A study of different metrics for predicting the experimental onset of electron trapping and acceleration is also presented.

2.1 Wakefield Generation

2.1.1 Necessary Conditions

A laser pulse requires three conditions to form a self-modulated laser wakefield:

(1) The laser must propagate in a medium in which its frequency, ω_l, is above the natural frequency of the plasma formed, ω_p

(2) The laser must have a power, P, above the critical power, P_c, to allow the onset of self-focusing

(3) The pulse duration, τ, must be longer than the plasma period, T_p

The first condition is the underdense plasma condition mentioned in Section 1.4.2. Even if a pulse had sufficient energy to start propagating in a medium by ionizing it and forming a wake, a frequency below that of the plasma frequency would lead to reflection of the incoming pulse energy, preventing the formation and sustained drive for a wake.

The second condition assures that self-focusing is possible, which allows the laser pulse to propagate through the plasma without expanding too quickly due to diffraction. While the other two conditions rely on steady system parameters such as frequency and pulse duration, the degree of self-focusing is controllable by adjusting the laser energy at a fixed pulse duration or the gaseous density of the medium. A consistent theme in Chapter 6 is the interplay between these two characteristics in determining where strong collective Thomson scattering probe signals – and consequently strong wakefields – were observed.

The third condition guarantees that the temporal (i.e., z-dimension) extent of the pulse will allow multiple plasma oscillations to form along it. The drive pulse can then self-modulate at the plasma frequency, enabling it to drive the wake resonantly to high amplitude so that it can capture and accelerate plasma electrons. The details of this process are discussed in Section 2.1.4.

2.1.2 Wakefield Seeding

While the laser-plasma acceleration might appear as simple as focusing a high-powered laser into a gas, the mechanics of sustaining a sufficiently large plasma wake require attention. When a locally uniform gaseous plasma is ionized by a laser, the local distribution of electrons has some random variation while the background ions remain more uniformly distributed due to their greater mass. A plasma wave needs a strong and consistent energy source to ensure that it can reach high enough amplitudes to accelerate electrons efficiently and compactly.

In self-modulated laser wakefield acceleration, generation of a plasma wakefield from a laser pulse is typically executed by the ponderomotive force in the linear wakefield regime ($a << 1$) [56]:

$$\left(\frac{\partial^2}{\partial t^2} + \omega_p^2\right)\frac{\delta n}{n_0} = c^2\nabla^2\left(\frac{a_0^2}{2}\right) \tag{2.3}$$

where $\delta n/n_0$ is the normalized density perturbation – the ratio of the ambient plasma electrons which undergo the plasma oscillation – and a_0 is the normalized laser parameter. A similar expression in terms of the electrostatic potential of the wave is also derivable:

$$\left(\frac{\partial^2}{\partial t^2} + \omega_p^2\right)\phi = \frac{\omega_p^2 a_0^2}{2} \tag{2.4}$$

The wakefield amplitude is thus found via Laplace transform:

$$\frac{\delta n}{n_0} = \frac{c^2}{\omega_p}\int_0^t dt' \sin\left(\omega_p(t-t')\right) * \frac{\nabla^2 a_0^2(\boldsymbol{r},t)}{2} \tag{2.5}$$

Through similar means and normalizing to the wavebreaking electric field discussed in Section 2.2, the axial electric field of the wave is calculated:

$$\frac{\boldsymbol{E}}{E_0} = -c\int_0^t dt' \sin\left(\omega_p(t-t')\right) * \frac{\nabla a_0^2(\boldsymbol{r},t)}{2} \tag{2.6}$$

These two equations – Eqs 4.3 and 4.4 – highlight the primacy of the ponderomotive force in wakefield generation.

Tajima and Dawson noted that the most efficient driving length of a plasma is given when the laser pulse's longitudinal extent is close to the plasma wavelength [57]. From an oscillator model perspective of a wake, the ideal duration of a resonant laser pulse for efficient wakefield generation is half of the plasma frequency:

$$c * \tau_l = \frac{\omega_p}{2} \tag{2.7}$$

Fig 2.1 shows a simplistic diagram of a temporal Gaussian laser pulse, its associated ponderomotive force at each location, and the wakefields generated by it. The ponderomotive force will have peaks separated by half of a plasma wavelength, effectively driving half of a plasma oscillation or one wake with a push and a pull.

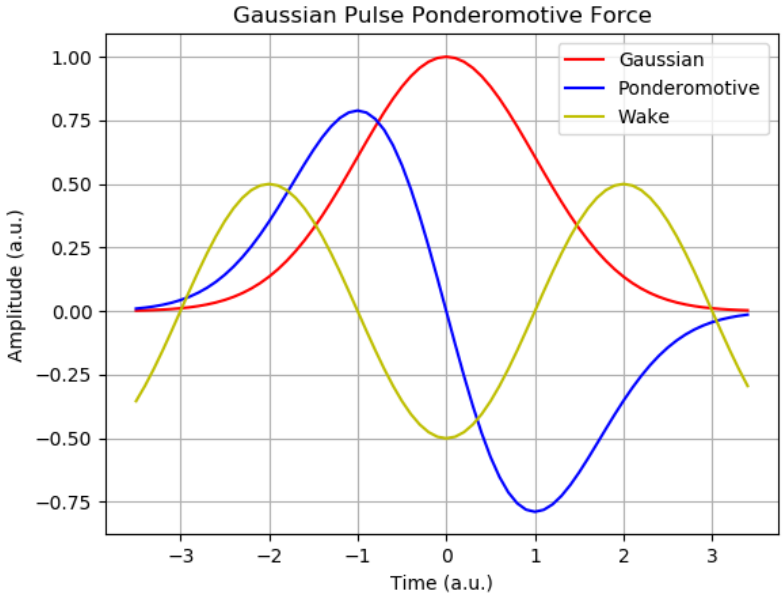

Figure 2.1: A plot of a 1D temporal Gaussian pulse's profile, ponderomotive force, and generated wake. The Gaussian size was chosen to match the plasma frequency condition in Eq. 4.5.

Two instabilities are critical to the formation of a self-modulated laser wakefield: the stimulated Raman scattering instability and the self-modulation instability. The first provides a widely used mechanism for observation of the wake properties while driving wake amplitude to large magnitudes. The second is where the technique take its name from.

2.1.3 Stimulated Raman Scattering

Stimulated Raman scattering refers to a set of scattering behaviors that occur when light travels in a plasma and interacts with an electron plasma wave. The light experiences a frequency shift then scatters. Two most important versions are Raman back scattering (RBS) and forward Raman scattering (FRS). These names refer to the direction of the

emitted light relative to the motion of the original pulse. The matching conditions for all stimulated Raman scattering processes are [58]

$$\omega_s = \omega_o \pm \omega_p \tag{2.6}$$

$$\boldsymbol{k}_s = \boldsymbol{k}_o \pm \boldsymbol{k}_p \tag{2.7}$$

where ω_s is the scattered frequency, ω_o is the incident frequency, ω_p is the plasma frequency, and the k-vectors are the wavevectors of each wave with the associated subscript. For reference, in experiments reported here, the CO_2 laser has ω_o of 177.7 THz and $|\mathbf{k}|$ is 592,800 m^{-1}. Typical values of ω_p and $\mathbf{k}_p$ for the range of densities used for this experiment spanned 20 to 80 THz as well as 66,713 to 266,850 m^{-1}, with the usual values near 50 THz and 166,800 m^{-1}.

FRS can be understood as a four-wave conversion process of an electromagnetic wave into a plasma wave and several electromagnetic sidebands. The initial laser pulse, with frequency ω_0 and wave vector k_0, is scattered by the electron plasma oscillation. The interaction converts some energy into a plasma wave with frequency ω_p. The remainder is transformed into Stokes sideband light, which has frequency $\omega_0 - \omega_p$ and wave vector $k_0 - k_p$, and anti-Stokes sideband light, which has frequency $\omega_0 + \omega_p$ and wave vector $k_0 + k_p$. Both modes are resonant during the interaction.

The signal magnitude of the FRS sidebands is highly correlated with large wakefield generation and, although less strongly, electron acceleration. Numerous sources of the onset of the FRS signal have been observed in simulations and experiments, as discussed by Chen [59]. The simplest noise source is random fluctuations in the ionized density, creating an imperfect but useful structure for energy conversion between the pulse and the plasma. The lowest energy electron plasma waves which can travel in a plasma occur at the plasma frequency, making even weak wave generation a mechanism for seeding amplification.

Ionization-induced ponderomotive forces, first identified by Mori, et al., [60] are another generator of preliminary ripples. A time-varying dielectric constant caused by the ionization of a gaseous medium leads to a liberated electron obtaining momentum from the electric field at the moment of ionization. The collective effect of these electron accelerations leads to a discrete ponderomotive-like force whose magnitude is proportional to $E^2\nabla\epsilon$. Such pushes lead to an initial plasma structure for FRS instabilities to utilize.

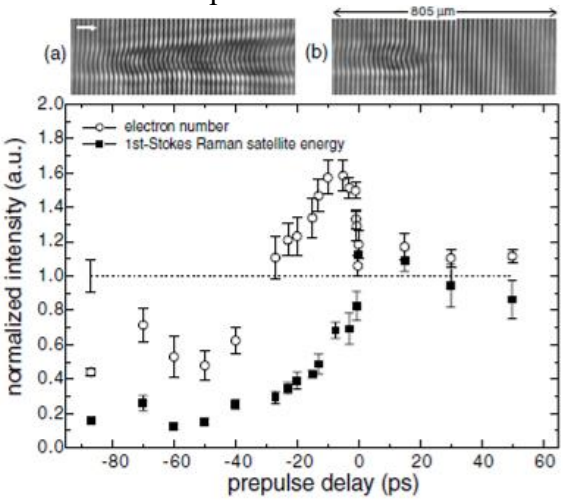

FIG. 1. First-Stokes Raman intensity (solid squares) and the number of electrons accelerated (open circles) as a function of prepulse timing. The dotted line is the value for the case of using only the main pulse. The inset shows the interferograms measured with a probe pulse arriving at the same time with the main pulse for a prepulse timing at (a) −10 ps and (b) 0 ps. With only the main pulse, the number of electrons above 200 keV is 10^9.

Figure 2.2: Electron acceleration and 1st-order Stokes signal strength as a function of prepulse delay from Chen

The ionization front of the pulse was observed experimentally to coincide temporally with the onset of FRS signals in SM-LWFA from a Ti:Sapphire system by LeBlanc [61] and 1D simulations confirmed the findings [62]. Gordon [63] points out that the large, instantaneous decrease in density at the ionization front will diminish the laser

pulse amplitude, leading to depressions in the laser pulse followed by steep rises, which causes immense ponderomotive forces. This laser-plasma behavior is known as ionization steepening and adds to the modulation of the laser pulse. It also increases the spatial variation in the neutral gas dielectric constant, further enhancing ionization-induced ponderomotive effects. Chen [59] prepared a 60-mJ, 55-fs prepulse to ionize helium gas at $1.8*10^{19}$ cm^{-3} before the 280-mJ, 250-fs pump pulse. When the prepulse led the pump by less than the decay time of the ionization-induced plasma wave, both FRS signal and number of electrons above 200 keV increased (Figure 2.2).

Back Raman scattering follows the same matching conditions, but directs the scattered light backwards relative to the incident laser light. Only Stokes shifted light is resonantly generated in this case, since the conservation of momentum goes as:

$$\boldsymbol{k}_o = \frac{2\pi}{\lambda}\widehat{\boldsymbol{k_o}} = \frac{2\pi}{\Delta\lambda}\widehat{\boldsymbol{k_p}} - \frac{2\pi}{\lambda + \Delta\lambda}\widehat{\boldsymbol{k_s}} = \boldsymbol{k}_p - \boldsymbol{k}_s \tag{2.8}$$

Here, a plasma oscillation is generated while some amount of light is reflected at a lower momentum. An anti-Stokes backscatter photon would need simultaneous increases in momentum and energy from a scattering source whose energy is moving in the opposite direction. While there is anti-Stokes backscatter signal generated in some experiments, the Stokes backscatter is much stronger. Back Raman scattering is the fastest growing of the stimulated Raman scattering, which allows quick generation of the preliminary wakefields in a plasma.

Back Raman scattering has also been theorized to play a role in generating the initial source of forward Raman scattering. Decker, et al., [64] found that Raman backscattering deforms the pump wave sufficiently to generate a wake and stimulate the FRS instability more rapidly, similar to the ionization self-steepening mechanism. Tzeng, et al. [65] observed in high-intensity simulations that both BRS and near-forward Raman

side scatter are present in the early stages of ionization and even undergo wavebreaking before the rapid growth of FRS suppresses their ability to grow. BRS energy in the strongly coupled regime also created a beat frequency with the pump light, leading to ponderomotive forces that allowed electron self-trapping and acceleration.

2.1.4 Modulation Instability

After the initial plasma wake is formed, the laser energy propagates through a wake structure of density depressions and peaks. The interplay between the pump pulse and the wake continues to drive energy from the pulse to the wake. The most efficient driving conditions for a simple harmonic oscillator near the resonant frequency occur when the peak of the driving force is $\pi/2$ out of phase with the oscillations [66]. Maintaining resonance of a wake in a plasma requires sustaining such a condition over an extended distance. The modulation instability does precisely that.

When a laser pulse with a temporal extent longer than the plasma wavelength travels through a wake, different portions of the beam observe different densities [67]. The peak densities have the smallest group velocities while the lowest densities have the smallest group velocities. The net result of the periodic structure of the wake is that the laser pulse begins to modulate, causing large depressions at the plasma density extrema and amassing peaks on the slope of the plasma wakes. Consequently, the locations of steepest ponderomotive potential slope spatially and temporally overlap with the wake peaks. Continued propagation through a wake medium allows large plasma wake amplitudes to form while imprinting an intensity oscillation with a characteristic length of the plasma period onto the laser pulse (Figure 2.3). This behavior is further reinforced from

transverse focusing of the energy at the depressions and defocusing at the peaks caused by effects similar in form to the ponderomotive self-focusing discussed in Section 1.4.2

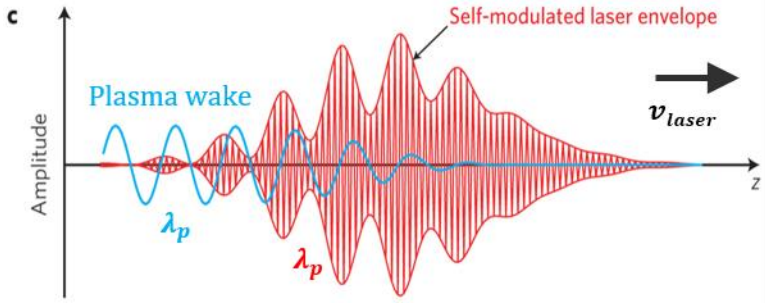

Figure 2.3: Diagram of the co-propagating self-modulated laser and the generated wakefield.

Note that while both FRS and self-modulation instabilities lead to wake format ion through interaction between the laser pulse and wakefield, the FRS mechanism does not incorporate the same spatio-temporal details inherent in the self-modulation instability. Esarey, et al., [68] put this idea concisely when writing that an LWFA based on purely FRS can be viewed as the 1D analog of the self-modulated LWFA.

2.2 Wakefield Evolution, Self-Trapping of Electrons, and Electron Acceleration

A plasma wave is composed of some ratio of the ambient background electrons providing a coherent oscillation at the same time. The ratio is typically denoted by α, which is consistent with the usage used in Chapter 4. When the ratio approaches 1, the result is a nonlinear wakefield. The electric field when α is 1 is known as the non-relativistic 1D cold plasma wavebreaking electric field, which is represented as [69]

$$E_z\left(\frac{V}{m}\right) = 96\sqrt{n_0(cm^{-3})} \tag{2.9}$$

In the case of a relativistic plasma, the condition is modified to [70]

$$E_z = \sqrt{2(1+a_0^2)(\gamma_p - 1)}E_0 \tag{2.10}$$

where E_0 is the non-relativistic wavebreaking field from Eq 4.9 and

$$\gamma_p = \frac{1}{\sqrt{1-\left(\frac{v_p^2}{c^2}\right)}} \tag{2.11}$$

For highly relativistic fields, the expression can be written as $\gamma_p \cong \frac{\omega}{\omega_p}$.

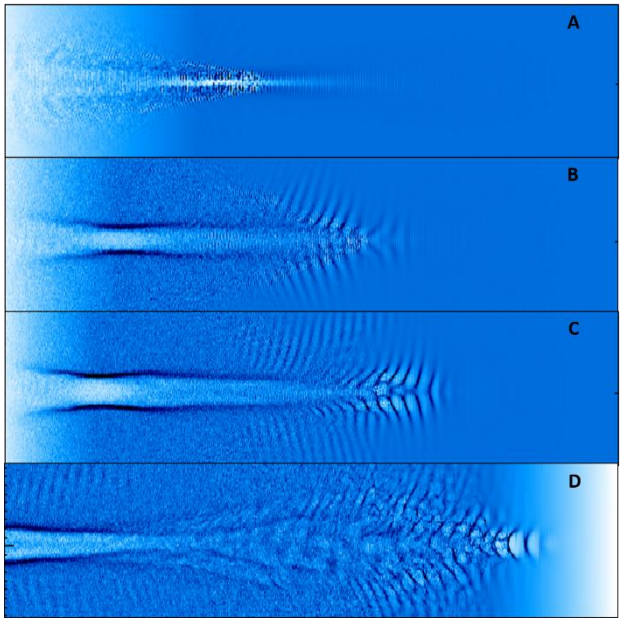

Figure 2.4: Four stages of wakefield formation and propagation. a) Self-focusing reduces the transverse dimensions of the pulse. b) Linear wakefields are generated near the front of the beam. c) Nonlinear wakes start to cause severe curvature to occur. d) The wakefield grows to unsustainable amplitudes and breaks down.

The propagation of plasma waves follows a common pattern of evolution during propagation. Understanding these steps is important to the upcoming discussion, so an example of the behavior is shown here. 3D OSIRIS simulations were performed by collaborators at Tsinghua University to detail the evolution of the plasma wakefield in $6*10^{17}$ cm^{-3} gas, assuming a CO_2 pulse power of 0.5 TW, a pulse duration of 2 ps, and a

beam waist of 25 μm. Fig 2.4a shows the onset of the initial self-focusing in the laser, compressing the pulse to a smaller cross section and resulting in a smaller spatial extent to the plasma wake. Fig 2.4b details the beginning of wake formation, which then propagates in the ionized region in a forward volume. Fig 2.4c details a region where both linear and nonlinear wake components are present, though the nonlinear volume is much smaller. Note the curvatures in the wakefield region are severe and in the opposite direction from propagation. Lastly, Fig 2.4d demonstrates the mix of structures after a prolonged period of propagation. If the laser and plasma parameters are such that the wake is driven to extreme growth, then the region tends to be chaotic and dispersed. Additionally, any probe signal is destroyed by the massive decoherence caused by the rapid changes in plasma density.

To effectively accelerate electrons, the plasma wave must capture some and provide a sustained longitudinal field over a significant propagation distance without the particles dispersing. The most common method of capturing electrons is self-capture of ambient non-oscillating electrons in the plasma, although work is currently being pursued at Brookhaven National Laboratory to provide an externally injected 50-fs electron beam into a resonant CO_2 laser wakefield to use it as an accelerating stage.

2.2.1 Wavebreaking

Figures 2.4b and 2.4c show the period in which electrons are captured and accelerated. One method of electron capture is known as wavebreaking. A problem for capturing ambient electrons in a self-modulated laser wakefield accelerator is that many of the plasma electrons already have significant transverse momentum which is largely coherent due to the wake oscillation. Non-oscillating electrons must migrate from their

initial locations into a region inside the traveling wake. Given that the wake travels at close to the speed of light, the trapped electrons must possess significant momentum before being captured to be able to make it into the accelerating region.

Fortunately, as the plasma electric field strength increases, it becomes easier to capture electrons. In the 1D limit, wavebreaking accelerates electrons by capturing ambient electrons that have sufficient momentum into the traveling wave. Bulanov describes 1D wavebreaking as occurring when the electron displacement is on the order of a plasma wavelength in two distinct regimes, one in which the wave merely disappears and another adiabatic one in which only a few electrons leave the wake and are accelerated. The latter regime allows wavebreaking for self-capture of electrons without the corresponding destruction of the wakefield.

Schroeder, et al. [71] used a warm relativistic plasma theory to calculate a minimum peak plasma electric field for the onset of capturing low-transverse-momentum ($p_t << m_e c$) electrons in the ultrarelativistic ($\gamma_p = 1$ and $\beta_p = 1$) regime:

$$\frac{E_z}{E_0} \approx \sqrt{\frac{m_e c}{p_t}} \tag{2.12}$$

Consequently, higher plasma electric fields capture electrons more efficiently. This also highlights the potential for increasing the capture rate by heating the surrounding plasma, though that will impact the ability to form and sustain a wake.

Experimental evidence of acceleration similar to 1D wavebreaking has been observed by Modena [72] and Gordon [73]. Modena used the 1.053-μm VULCAN laser at Rutherford Appleton Labs with 25-TW, 800-fs pulses with a beam waist of 10 μm in helium. When the plasma density was increased from 0.54 10^{19} cm^{-3} to 1.5*10^{19} cm^{-3}, formerly clean upshifted FRS peaks expanded significantly (corresponding to scattering off of a thermal distribution of electrons) coinciding with a dramatic increase in the number and energy of accelerated electrons. Gordon, et al., used the same laser with an upgraded 20 J at 1 ps in a 4-mm helium gas jet. They observed electrons as high as 94 MeV, much larger than the predicted energy gain based on the dephasing length.

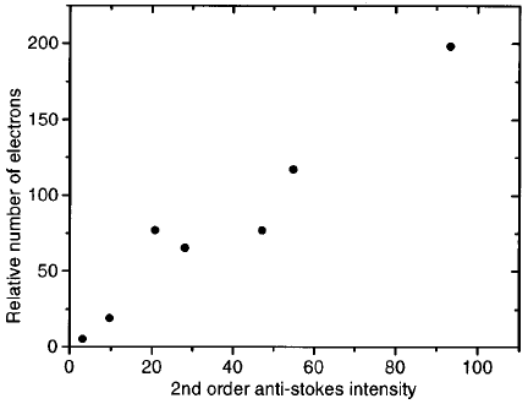

FIG. 11. The correlation between the second-order anti-Stokes signal and the number of high energy (>1 MeV) electrons

Figure 2.5: A figure from Ting, et al., demonstrating a positive relationship between 2nd-order anti-Stokes signal and accelerated electron yield

Other experiments and simulations detailed significant electron acceleration for peak plasma fields significantly below the 1D wavebreaking limit. Ting, et al., [74] observed plasma wakefields of amplitude roughly 0.1 to 0.3 which accelerated electrons to 30 MeV using NRL's 1.054-μm, 400-fs, 2-3 TW system to drive plasma of density 10^{19}

cm^{-3}. Subsequent simulations demonstrated the onset of significant electron trapping and acceleration when the wakefield amplitude was increased from 0.3 to 0.5.

Simulation work by Esarey, et al., [75] noted a similarly abrupt onset of electron trapping when the field was roughly 25% of the wavebreaking limit. Even the above Gordon work was not at the predicted wavebreaking electric fields. The measured wakefield amplitude was between 0.2 and 0.6. These results highlight a critical experimental idea: wakefields need not reach an amplitude of 1 to accelerate electrons. However, it does not provide a precise guide for when electron acceleration will begin.

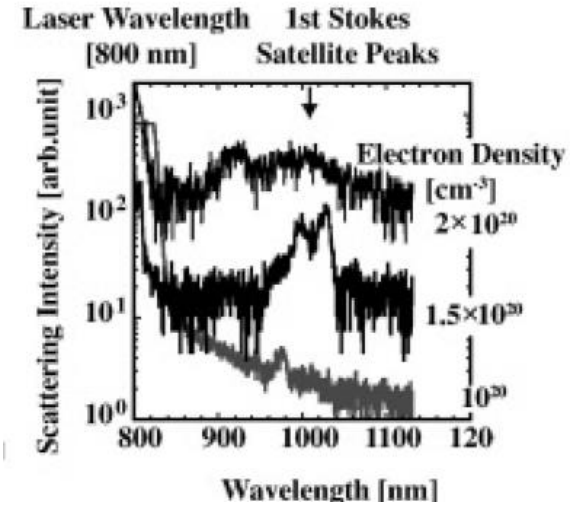

Figure 2.6: Pump beam Stokes signal evolution with increasing density. The spectral broadening of the Stokes signal is due to electron collisional broadening of the probe during wave breaking.

Spectral broadening of FRS sidebands has been observed when wave breaking occurs due to the spread in electron energies during the process. The formerly clear peak of the sideband becomes a noisy modulated spectral region. Figure 2.6 is taken from Koyama, et al. [76] and demonstrates the evolution of a Stokes signal with increasing density. At 10^{20} cm^{-3}, the peak is relatively weak. As the density rises to $1.5*10^{20}$ cm^{-3}, the

signal strength increases and a relativistic correction forms (see Section 4.4 for a discussion of their formation). Finally, at $2*10^{20}$ cm^{-3}, the location of shift changes and the spectrum broadens. Note that this result did not subtract the background signal.

3D SPACE simulations were performed at Stony Brook University to see if similar behavior was predicted under our experimental conditions. The gaseous density was taken in the range of 5e17 to 1e18 cm^{-3}. The peak intensity of the probe sideband signals for both Stokes and anti-Stokes were measured (Figure 2.7). As P_{cr} decreases with density, an increase in density will cause P/P_{cr} to rise. The Stokes signal is barely present ($P \leq P_{cr}$, at 5e17 cm^{-3}) before rising dramatically as self-focusing starts to dominate ($P \geq P_{cr}$, 7.5e17 cm^{-3}). As density increased further ($P >> P_{cr}$), the sideband signal strength dropped quickly.

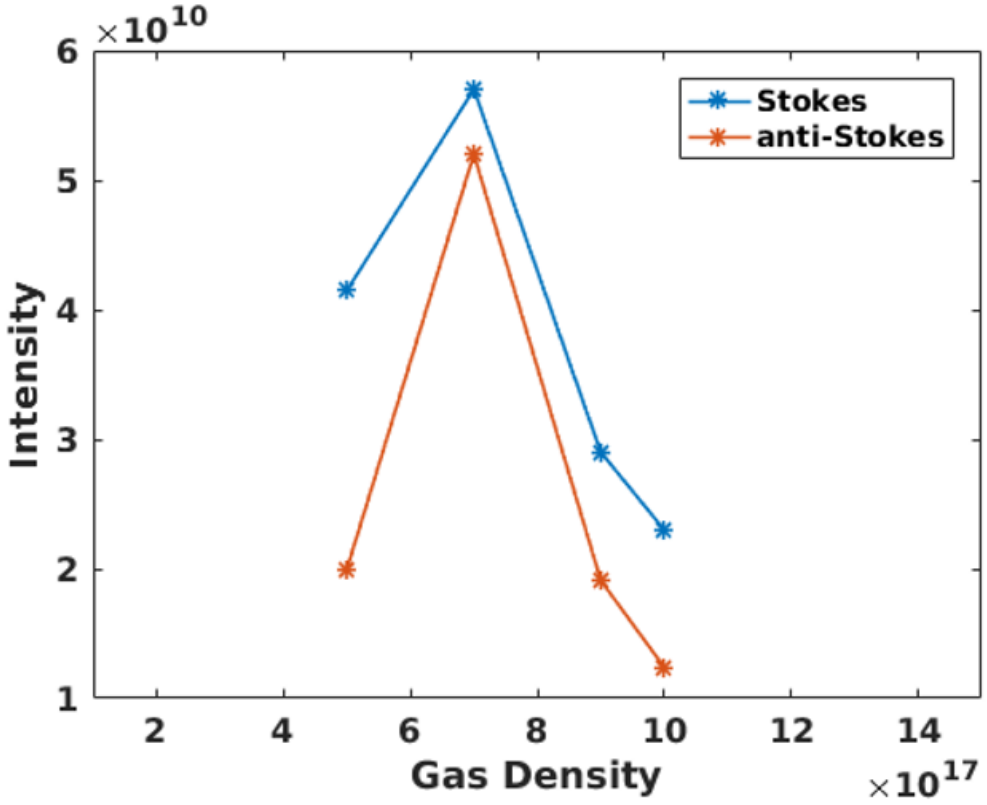

Figure 2.7: Simulation results demonstrating signal strength of Stokes and anti-Stokes sidebands at varying densities.

2.2.2 Transverse Wavebreaking

Due to ponderomotive effects pushing electrons around the plasma as well as other self-steepening effects, the plasma wake amplitude is able to reach and even surpass the natural maximum of 1. This leads to a highly nonlinear wakefield with a very steep plasma density gradient. For a Gaussian transverse profile, the on-axis ponderomotive forces are stronger than those at the edges, leading the center of the plasma wake to lag significantly behind the edges. The net result of these effects is the creation of "horseshoe" shapes in the plasma, consistent with the behavior discussed in the relativistic self-focusing section.

Bulanov, et al., performed a series of 2D simulations which demonstrated an alternative trapping mechanism, known as transverse wavebreaking [77]. In self-modulated laser plasma wakefields, multiple plasma oscillations can form sequentially. The curvature of the plasma waves due to effects such as radial nonlinear refractive index variation and self-focusing effects provide "cups" in each oscillation. When the radius of

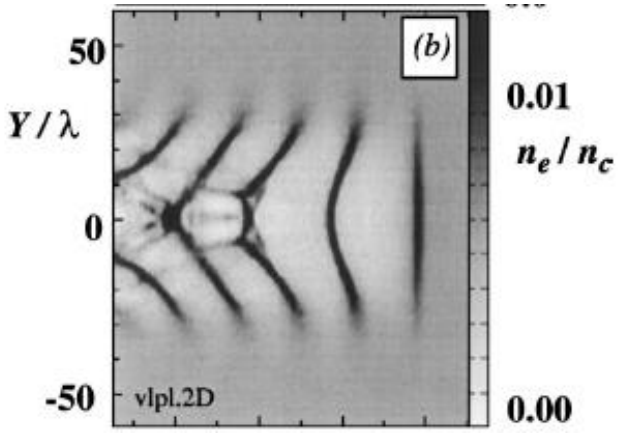

Figure 2.8: A simulation figure from Bulanov's paper displaying the density of plasma wave. The "horseshoe" curvature is visible, as is a region in which electrons are leaking from one wake to the next and being accelerated.

curvature of the trailing wake reaches the order of magnitude of the electron displacement,

the electrons from the leading wake can then get caught in the cup of the trailing wake and become accelerated. Repeated capture can lead to the breakdown of the forward wake. Figure 2.8 shows one of Bulanov's simulations, depicting the electron density with darker regions having higher densities [78]. A pronounced curvature is visible, as are electrons in between two wakes.

2.2.3 Raman Back Scattering Trapping

A third method of self-injection of electrons is possible from the back Raman scattering. As the fastest growing stimulated Raman scattering instability, the onset of the reflected light is quick compared to side and forward scattering [79]. The reflected light interferes with the primary pulse light, which leads to a slow-phase-velocity ($v_p \sim \omega_p/2*k_0 << c$) pulse. The ponderomotive force of this beat pulse drives a new smaller wake whose electrons start to heat. After reaching sufficient energies, these separate electrons can be captured by the primary wake and accelerated to even higher energies.

Moore, et al., observed electrons reaching 30 MeV when 1,054-nm laser with 400 fs and 1 J was focused into a helium plasma with an electron density of $1.4*10^{19}$ cm^{-3} [80]. The pump spectrum after the interaction region displayed numerous orders of anti-Stokes light, several of which displayed relativistic shifts. The lack of spectral broadening of these FRS orders was taken as a sign that wave breaking had not occurred in the acceleration and the back scattering trapping was capturing a significant number of electrons.

2.3 Electron Energy Gain Predictions

Electron energy gain predictions from a laser plasma accelerator go back to before Tajima and Dawson's original paper. Tajima and Dawson performed a relativistic electrodynamic analysis of the process. Their result, which found the peak electron energy gain occurred when an electron reversed its direction in the wave frame, was:

$$W_{max} = 2\gamma_p m_e c^2 \tag{2.13}$$

An alternative derivation method proves a more instructive for understanding the laser-plasma dynamics. Electron acceleration mechanisms are typically limited by either the depletion length – the distance before the laser energy is too low to drive the process – or the dephasing length – the distance before the electrons outrun the plasma wake. For high-intensity pulses, propagation is limited by the dephasing length, which is estimated as the distance an electron must travel before it slips the phase of the plasma wake by half of a wavelength, $\lambda_p/2$. The electrons are moving faster than the phase velocity of the plasma, so the dephasing length L_d is given by the difference by the ratio of the distance by the velocity mismatch:

$$L_d = \frac{\lambda_p}{2\left(1 - \frac{v_p}{v_z}\right)} \tag{2.14}$$

For highly relativistic electrons ($v_z \sim c$), the expression reduces the form

$$L_d \cong \gamma_p^2 \lambda_p \tag{2.15}$$

where γ_p again has the form ω/ω_p.

Given the expression for dephasing length, an approximate value for the maximum energy gain of a captured electron is the electric force provided of the plasma wake times this distance:

$$W_{max} = eE_{max}L_d \tag{2.16}$$

where E_{max} is the maximum electric field of the plasma wake. A simplistic use of the wavebreaking limit, E_0, can produce an estimate of the expression. Using

$$E_0 = \frac{cm_e\omega_p}{e} \tag{2.17}$$

the expression for W_{max} becomes:

$$W_{max} = e\left(\frac{cm_e\omega_p}{e}\right)\gamma_p^2\lambda_p = cm_e\omega_p\lambda_p\gamma_p^2 \approx 2\pi\gamma_p^2 m_e c^2 \tag{2.18}$$

by assuming the plasma wave phase velocity is close to c. This expression predicts a three-fold increase in the maximum energy gain compared to Tajima and Dawson. However, it also assumes acceleration through the entire dephasing length, which requires immediate capture and full dephasing length propagation to occur.

Esarey, et al., [70] mention that the inclusion of space charge effects due to self-channeling can lead to final energies as high as $4\gamma_p^2 m_e c^2$. Additional nonlinear effects can increase the energy gain by as much as a factor of 3. For the most favorable experimental values used in the work performed for this thesis and including all of the factors Esarey mentioned, the estimate for maximum electron energy gain over the entire dephasing length comes to 480 MeV. However, the dephasing length of 7.377 mm is much larger than the approximate 1-mm width of the gas jet. A revised estimate accounting for the length of the gas jet would put the upper limit closer to 65 MeV.

2.4 Investigation of Predictive Metrics for the Onset of Electron Acceleration

As detailed above, the estimates of the electron acceleration gain can vary by large factors, even orders of magnitude. Due to the highly nonlinear nature of the environment and the optimism of the assumptions, this is often much larger than observed energies. Consequently, correspondence between these estimates and experimentally determined electron energies is rarely found to match, with the theoretical estimates drastically overestimating the final energies in most cases. For example, the 2004 paper by Chen, et al., used an 810-nm laser in a He gas jet with a plasma wavelength of 7.9 μm. The dephasing length was calculated as 0.75 mm for a flat-top jet diameter of 1 mm with 250-μm ramps on either side. The estimated maximum energy gain for the metrics described above ($2\gamma_p^2$, $4\gamma_p^2$, and $12\gamma_p^2$) predicted respectively an electron energy gain of 97 MeV, 193 MeV, and 579 MeV, in contrast to the measured value of about 45 MeV.

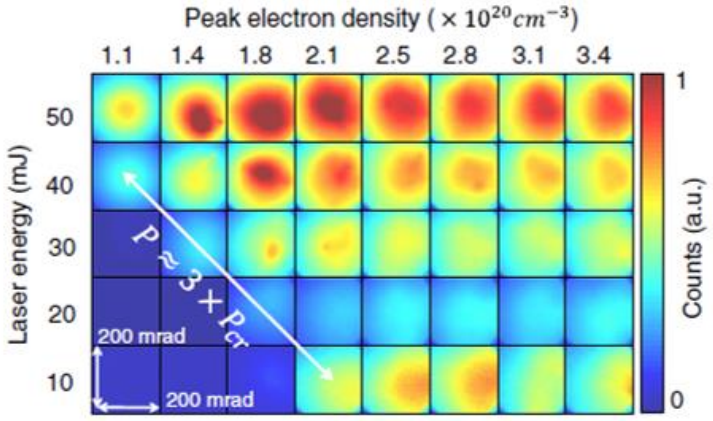

FIG. 2 (color online). Single shot electron beam images for energies >1 MeV for a range of laser energies and peak electron densities. The color palette was scaled up by 10× for the 10 mJ column. The onset laser power for detectable electron beam generation was $\sim 3P_{cr}$ across our range of conditions.

Figure 2.9: Figure from Goers, et al., demonstrating the onset of electron acceleration when the pump pulse power crossed the $3P_{cr}$ threshold. Note the electron spectrometer was limited to a range of 2 MeV to 12 MeV.

A review of 21 papers detailing self-modulated laser wakefield electron acceleration for comparison with the three metrics – the vast majority of which had dephasing lengths substantially less than 1 mm – found only two instances of any single metric being within 5% of the associated measured value (with the predicted value in the denominator). Even when the difference ratio threshold is increased to 50%, only one in six shots is actually within that range.

In addition to the lack of any consistent energy estimates, the conditions for the initial onset of electron acceleration are still not well understood. The practical difficulty of measuring the electric field of plasma wakes as it evolves or the temperature of ambient electrons in the plasma at different times impedes experimentalists' ability to determine which conditions will result in electron acceleration. A simple metric which determines whether a specific laser will see a drastic increase in self-modulated laser wakefield electron production at a specific plasma density would provide laser physicists with a useful method for determining whether their laser system is capable of performing S-M LWFA experiments.

Two potential metrics have been proposed in the literature. Goers, et al., [81] used a Ti:Sapphire laser with an f/9.5 off-axis parabola to explore the onset of electron acceleration in a hydrogen gas jet (Figure 2.9). A power threshold of $3*P_{cr}$ was determined to portend the onset of electrons. An important caveat to this work is that the electron energy spectrometer in this work appears to have a detection range of 2 to 12 MeV, so electrons outside that range would not have been observed. Additionally, in the figure above, several of the images below the critical line seem to display weak but visible signals. This metric is appealing for its simplicity and its independence of both plasma and laser wavelength.

Mori, et al., [82] used a Ti:Sapphire laser with an f/22 focus to study electron acceleration onset in argon gas. The metric they determined includes the laser and plasma wavelengths as parameters for the threshold vector potential:

$$a_{th} = 6.6\left(\frac{\lambda_L}{\lambda_p}\right)\sqrt{P_0(TW)} \tag{2.19}$$

The threshold parameter is appealing for its inclusion of two parameters that the Goers critical power ratio neglects, providing a contrasting perspective.

A historical literature search of past experimental results – the aforementioned 21 papers – was conducted to see how the metrics performed on real parameters where electron acceleration in gaseous media was measured. Care was taken to identify the specific parameters at the onset of electron acceleration as accurately as possible. Table 2.1 organizes the main findings as well as provides a useful reference for future historical analysis of self-modulated laser wakefield experiments. Of note is the lack of former experiments in this wavelength regime for gaseous media.

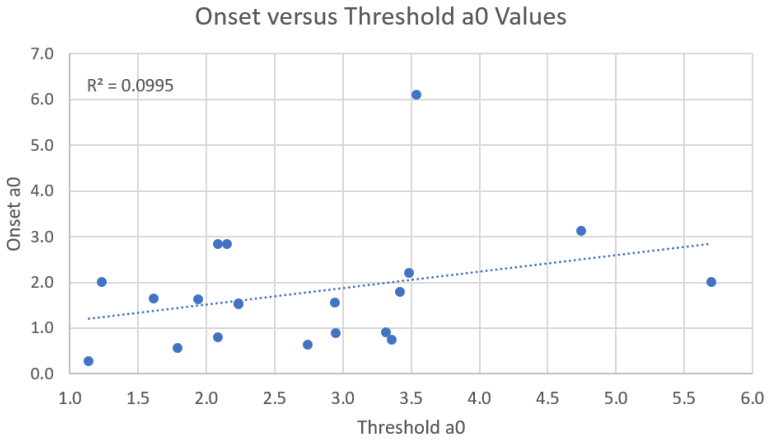

Figure 2.10: Graph of the electron injection onset a_0 values against the predicted threshold a_0 values.

The variation in methods used in these papers is non-trivial and were considered during review. The papers involved spanned a wide variety of parameters including multiple gas species [83] [84] [Leemans, Koyama, Albert] and less common species such as argon [M Mori] and nitrogen [85] [86] [87] [Masuda 2007, Ting 2005, Hafz 2006]; pulse durations between 35 fs and 1 ps [88] [V Malka, Gordon 1998]; densities between $4*10^{18}$ to $9*10^{20}$ cm^{-3} [89] [Najmudin, Goers]; laser powers between 2 and 150 TW [90] [Chen 1999, Albert]; Ti:Sapphire and Nd:glass laser wavelengths [91] [92] [Bobbili, Nakajima]; methods for enhancing electron acceleration such as prepulse gas ionization (Chen 2004); orders-of-magnitude variations in electron spectra and electron detector sensitivity ranges; exploration of the transitional region between self-modulated laser wakefield and resonant laser wakefield [93] [Masuda 2009]; various probing methods including shadowgraphy [94] [Koyama, Masuda 2007, Goers], side-scatter measurements [95] [96] [97] [Bobbili, Chen 1999 and 2004, Coverdale, Goers, Koyama, Masuda 2007, Moore, Rao, Wagner], and forward Raman scattering of either the pump [98] [Albert, Bobbili, Chen 1999 and 2004, Goers Koyama, Moore, Najmudin, Rao] or co-propagating probes [99] [Gordon 1998, LeBlanc]; and publication dates from 1994 to 2017 [Coverdale], which obscures the wealth of additional tools available to the later researchers. The availability of specific variable information such as transverse shape and profile differed between papers, which is information not included in any of the metrics. This variability between individual cases may have an influence on the validity of direct comparison.

The threshold laser parameter was quite poor at predicting electron onset. Most of the papers had a_0 values less than the predicted threshold value and there was little linear correlation between the two variables (Figure 2.10). The lack of trend held in subpopulations such as laser wavelength, gas species, similar electron density, and similar laser energy, as well as when the seeming outliers were removed. This metric is easily

dismissed as a cross-experimental metric but may still have some validity for a single experimental setup such as Mori, et al., used.

The power ratio provides a more nuanced picture. All but two of the experimental results had powers in excess of thrice the critical power. Rather than seeing numerous results clustering around a power ratio of three, the most frequent results appear near a power ratio of six. Some of these experiments, especially those by Albert and Malka, are far above these ratios with their lowest powers.

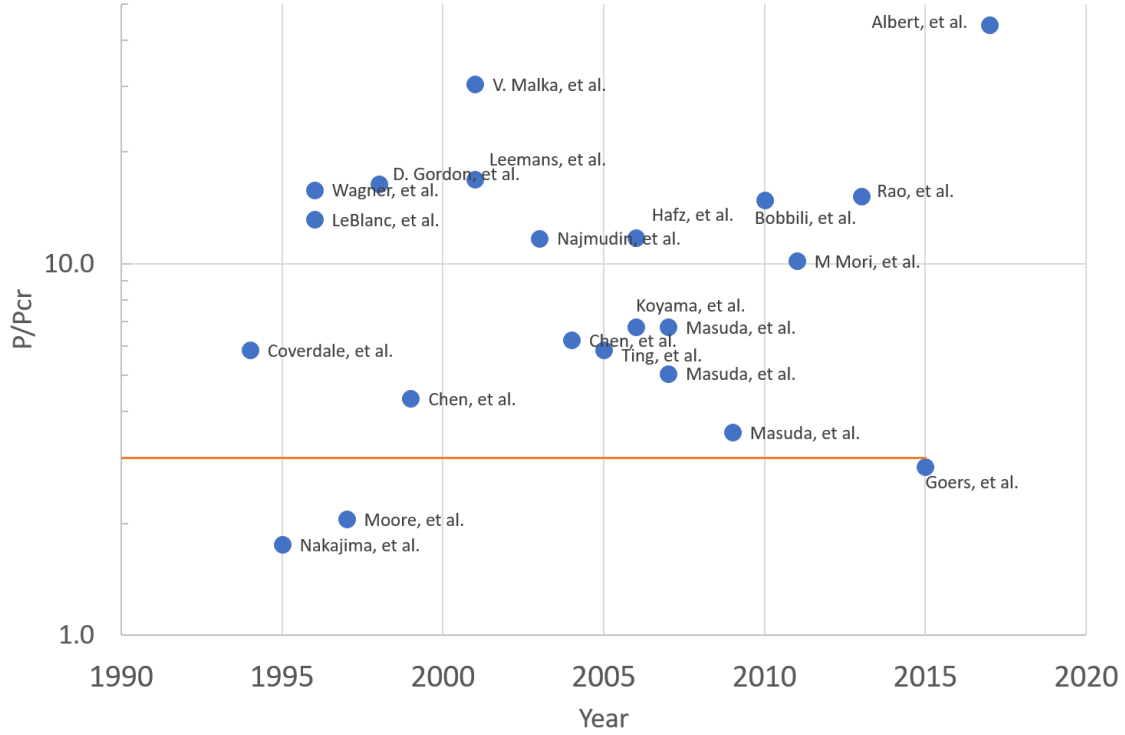

Figure 2.11: The measured P/P_{cr} values versus year. Note that the orange line representing $P = 3*P_{cr}$

A difference factor of two to four from the prescribed metric is not surprising in such a nonlinear regime. An integral over the two-dimensional Gaussian through a full-

width at half maximum yields a volumetric ratio of 0.58, which could easily account for a factor of two. An ordering by f/# shows that many experiments with the smallest f/# values had power ratios closer to six than 3. Additionally, “midrange” f/# values between 8 and 12 yielded the smallest P/P_{cr} ratios, which crucially including the Goers paper. This trend, taken with the undoubted importance of self-focusing, suggests a potential trade-off in traditional focusing and self-focusing effects for electron acceleration. For small f/# experiments, diffraction prevents the full beam energy from focusing as much, resulting in the threshold ratio being six or higher. For moderate f/# experiments, self-focusing has more time to focus and incorporate beam energy into the laser driving structure.

While the study did not conclude that the Goers metric was applicable across wavelengths and power regimes, the results do warrant further study on whether an appropriate power ratio combined with an appropriate f/# can determine the onset of electron acceleration.

Another interesting result is the electron energy versus pulse power. Between 1 and 10 TW, the measured electron energies were between 2 and 45 MeV. The graph does not account for the variation in laser wavelength, gas species, or density, but it does demonstrate the peak energies at each pulse power for historical note.

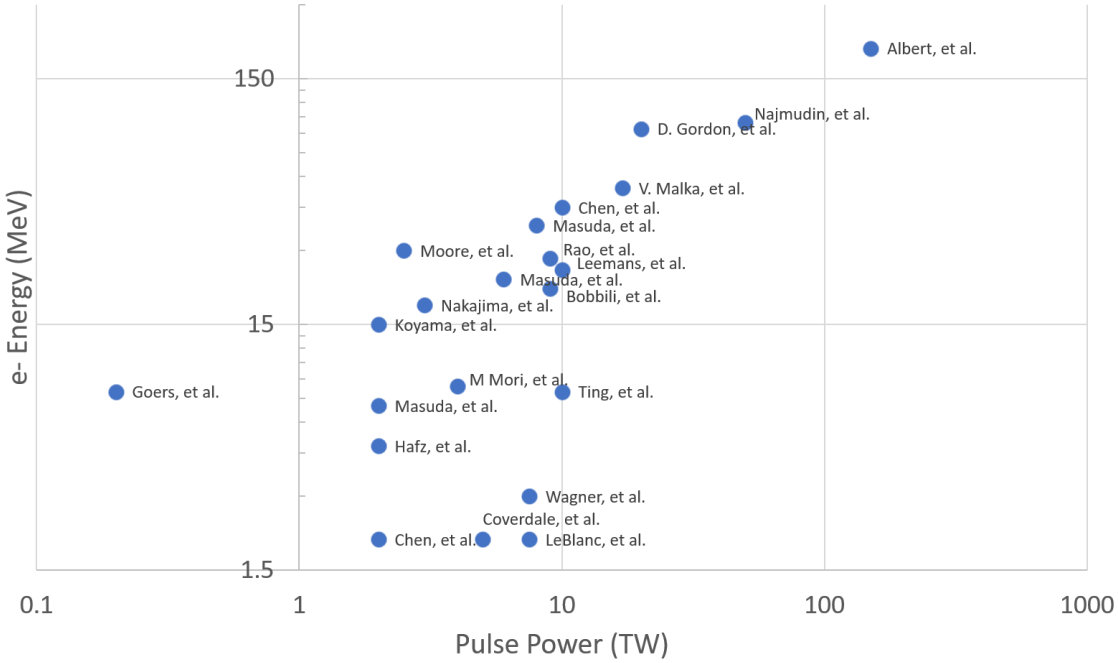

Figure 2.12: Accelerated electron energy versus pulse power

Table 2.1: Papers Detailing Self-Modulated Laser Wakefield Electron Acceleration

Authors	Year	Gas (Element)	λl (nm)	λ_p (nm)		n_{crit} (cm^-3)	n_e (cm^-3)
Albert, et al.	2017	He, He/N mixture	1053	14932		1.01E+21	5.00E+18
Goers, et al.	2015	H	800	1629		1.74E+21	4.20E+20
Rao, et al.	2013	He	800	4722		1.74E+21	5.00E+19
M Mori, et al.	2011	Ar	800	3850		1.74E+21	7.52E+19
Bobbili, et al.	2010	He	790	4722		1.79E+21	5.00E+19
Masuda, et al.	2009	He	800	9261		1.74E+21	1.30E+19
Masuda, et al.	2007	N	800	3339		1.74E+21	1.00E+20
Masuda, et al.	2007	He	800	6678		1.74E+21	2.50E+19
Koyama, et al.	2006	He, He/N mixture	800	3339		1.74E+21	1.00E+20
Hafz, et al.	2006	N2	1054	3339		1.00E+21	1.00E+20
Ting, et al.	2005	N	1053	10559		1.01E+21	1.00E+19
Chen, et al.	2004	He	810	7870		1.70E+21	1.80E+19
Najmudin, et al.	2003	H or He	1053	16695		1.01E+21	4.00E+18
Leemans, et al.	2001	H, He, and N	800	4722		1.74E+21	5.00E+19
V. Malka, et al.	2001	He	820	4722		1.66E+21	5.00E+19
Chen, et al.	1999	He	1053	5489		1.01E+21	3.70E+19
D. Gordon, et al.	1998	He	1053	8924		1.01E+21	1.40E+19
Moore, et al.	1997	He	1054	8924		1.00E+21	1.40E+19
Wagner, et al.	1996	He	1053	5565		1.01E+21	3.60E+19
LeBlanc, et al.	1996	He	1053	6096		1.01E+21	3.00E+19
Nakajima, et al.	1995	He	1052	10559		1.01E+21	1.00E+19
Coverdale, et al.	1994	He	1053	7466		1.01E+21	2.00E+19

Table 2.1 Continued: Papers Detailing Self-Modulated Laser Wakefield Electron Acceleration

Authors		E(mJ)	τ (fs)	P (TW)	w0 (um)	I0 (W/cm^2)		f/#	L_{deph} (mm)	E_{e-} (MeV)
Albert, et al.		150000	1000	150	6.7	5.00E+18		10.0	3.003	200
Goers, et al.		10	50	0.2	8.4	9.02E+16		9.5	0.007	8
Rao, et al.		405	45	9	5.1	1.20E+18		10.0	0.165	28
M Mori, et al.		160	40	4	11.2	9.00E+17		22.0	0.089	8.4
Bobbili, et al.		405	45	9	5.0	1.80E+18		10.0	0.169	21
Masuda, et al.		400	50	8	9.0	5.80E+18		17.7	1.241	38
Masuda, et al.		100	50	2	1.7	5.10E+18		3.3	0.058	7
Masuda, et al.		300	50	6	3.1	5.70E+18		6.0	0.465	23
Koyama, et al.		100	50	2	1.8	5.00E+18		3.5	0.058	15
Hafz, et al.		1400	700	2	2.0	1.00E+18		3.0	0.034	4.8
Ting, et al.		5000	500	10	1.3	1.00E+19		2.0	1.062	8
Chen, et al.		550	55	10	8.6	6.59E+17		16.7	0.743	45
Najmudin, et al.		50000	1000	50	10.0	3.00E+18		14.9	4.197	100
Leemans, et al.		500	50	10	8.0	8.00E+19		15.7	0.165	25
V. Malka, et al.		600	35	17	-	2.00E+19		-	0.157	54
Chen, et al.		1600	400	2	2.2	1.00E+19		3.3	0.149	2
D. Gordon, et al.		20000	1000	20	3.0	6.00E+18		4.5	0.641	94
Moore, et al.		1000	400	2.5	6.0	5.00E+18		8.9	0.640	30
Wagner, et al.		3000	400	7.5	2.7	4.00E+18		4.0	0.155	3
LeBlanc, et al.		3000	400	7.5	8.9	6.00E+18		4.0	0.204	2
Nakajima, et al.		3000	1000	3	8.0	1.00E+17		11.9	1.064	18
Coverdale, et al.		3000	600	5	8.2	8.00E+17		5.5	0.375	2

Table 2.1 Continued: Papers Detailing Self-Modulated Laser Wakefield Electron Acceleration

Authors	E_{e^-} (MeV)		Pcr (TW)	P/Pcr		a0	ath
Albert, et al.	200		3.4	43.9		2.0	5.7
Goers, et al.	8		0.1	2.8		0.2	1.4
Rao, et al.	28		0.6	15.2		0.7	3.4
M Mori, et al.	8.4		0.4	10.2		0.6	2.7
Bobbili, et al.	21		0.6	14.8		0.9	3.3
Masuda, et al.	38		2.3	3.5		1.6	1.6
Masuda, et al.	7		0.3	6.8		1.5	2.2
Masuda, et al.	23		1.2	5.1		1.6	1.9
Koyama, et al.	15		0.3	6.8		1.5	2.2
Hafz, et al.	4.8		0.2	11.7		0.9	2.9
Ting, et al.	8		1.7	5.9		2.8	2.1
Chen, et al.	45		1.6	6.2		2.8	2.1
Najmudin, et al.	100		4.3	11.7		1.6	2.9
Leemans, et al.	25		0.6	16.9		6.1	3.5
V. Malka, et al.	54		0.6	30.4		3.1	4.7
Chen, et al.	2		0.5	4.3		0.6	1.8
D. Gordon, et al.	94		1.2	16.4		2.2	3.5
Moore, et al.	30		1.2	2.1		2.0	1.2
Wagner, et al.	3		0.5	15.8		1.8	3.4
LeBlanc, et al.	2		0.6	13.2		2.2	3.1
Nakajima, et al.	18		1.7	1.8		0.3	1.1
Coverdale, et al.	2		0.9	5.9		0.8	2.1

Chapter 3: Wavelength Scaling

An overview of the wavelengths attainable by classic and modern lasers is presented. A comparison of the scaling of various laser characteristics with wavelength and energy is then made, and their applications to LWFAS described.

The operating principles of CO_2 lasers are covered. Lastly, the components and configuration of the Brookhaven National Laboratory (BNL) Accelerator Test Facility (ATF) CO_2 laser used in the experimental work are shown.

3.1 Wavelength Scaling Principles

To understand why wavelength scaling has sparked interest in the LWFA community, the achievements of the power scaling must first be discussed. As mentioned in Chapter 1, the advancements in ultrafast laser technologies have come from one of two laser engineering feats: increasing the energy in a pulse or decreasing the duration of a pulse. Each innovation and new design led to enhancements of power and intensity achievable by ultrafast lasers. However, a combination of characteristics – solid density, large gain profile, high damage threshold – makes the solid-state laser technology of Ti:Sapphire and Nd:Glass the most successful at exploring more extreme phenomena.

Continued enhancement of laser power has made sense, given the dependence of critical parameters on it. Returning to the expression from Chapter 1 for non-relativistic ponderomotive force, the expression appears in terms of the laser's angular frequency as:

$$\frac{d\boldsymbol{p}}{dt} = -\frac{e^2}{4m_e\omega_l^2}\nabla\overline{E^2} \tag{3.8}$$

Recall the common expression for intensity:

$$\bar{I} = \frac{\bar{E}^2}{2\mu_0 c} \tag{3.9}$$

A simple substitution expresses Equation 3.1 in terms of intensity:

$$\frac{d\boldsymbol{p}}{dt} = -\frac{e^2 \mu_0 c}{2m_e \omega_l^2} \nabla \bar{I} \tag{3.10}$$

Converting laser angular frequency to laser wavelength yields

$$\frac{d\boldsymbol{p}}{dt} = -\frac{e^2 \mu_0}{8\pi^2 m_e c} \lambda_l^2 \nabla \bar{I} \tag{3.11}$$

Integrating this quantity in space returns an alternative expression for the ponderomotive energy:

$$U_{pond} = \frac{e^2 \mu_0}{8\pi^2 m_e c} \lambda_l^2 \bar{I} \tag{3.12}$$

The ponderomotive force thus scales with the gradient of the intensity of the laser pulse while the ponderomotive energy scales linearly with intensity, while both quantities scale quadratically with laser wavelength. Thusly, both the rationale for the historical emphasis on increasing power, and by extension intensity, as well as the interest in long-wavelength lasers are justified simultaneously.

Ponderomotive force is critical for resonant wakefield acceleration to reach the bubble regime. Expulsion of electrons from the plasma volume occurs immediately behind the laser pulse is what allows the background ions to accelerate captured electrons to such high energies. Additionally, the dimensions of the bubble scale with the laser wavelength [100]:

$$r_B \sim \frac{2}{k_p} \sqrt{a_0} \sim \frac{2}{k_p} \sqrt{\lambda} \tag{3.13}$$

Current single-shot imaging methods such as frequency-domain streak cameras (FDSC) have had success in capturing the internal dynamics of resonant laser wakefield acceleration, but the bubble dimensions are often comparable to the spatial resolution limit of broad-spectrum FDSC probes. Longer wavelength pump lasers would create larger bubbles, improving not only the utility of existing image techniques but also providing a more stable bubble due to the reduced sensitivity to boundary variations during formation and evolution.

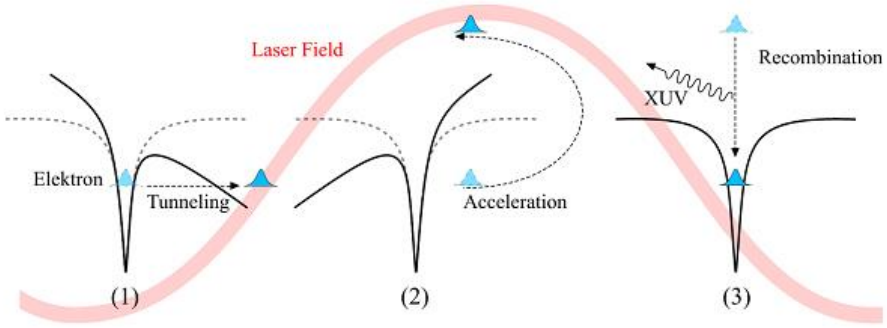

Figure 3.1: A depiction of the Coulomb barrier during a tunneling ionization harmonic generation cycle. Barrier suppression leads to electron tunneling (1), followed by electron acceleration by the laser pulse (2). The harmonics are emitted during the recombination phase (3).

The ponderomotive energy is often considered secondarily in laser wakefield applications to the ponderomotive force used to generate wakefields and reach the bubble regime. For ionization experiments, however, the ponderomotive energy predicts the time-averaged energy of electrons liberated through tunneling ionization [101] (Fig. 3.1). An electron which escapes the Coulomb potential of its atom will experience acceleration based on the electric field of the laser present at the time of escape. Consequently, it will undergo harmonic motion where the energy contained in the oscillation is given by the ponderomotive energy. These accelerated electrons may then recombine with atoms,

emitting harmonics while they are captured [102]. The harmonics have a maximum energy cutoff given in terms of the ionization potential and ponderomotive energy:

$$E_{max} = I_p + 3.17 * U_p \tag{3.14}$$

This expression demonstrates another potential use for long-wavelength lasers in generating higher harmonics.

The source of the benefits of longer wavelength laser is not immediately obvious from the wavelength-centric representation of these properties. However, another simple conversion is quite illuminating. Starting from the relationship between a laser's wavelength and frequency in free space, the oscillation time is merely the inverse of the frequency:

$$\lambda\nu = \frac{\lambda}{\tau} = c \rightarrow \lambda = c\tau \tag{3.15}$$

Hence, longer wavelengths are equivalent to longer oscillation times. Substituting this expression into the ponderomotive force equation yields:

$$\frac{d\boldsymbol{p}}{dt} = -\frac{e^2\mu_0 c}{8\pi^2 m_e}\tau_l^2\nabla\bar{I} \tag{3.16}$$

The source of the gains is now obvious. When all other properties are held constant, long wavelength lasers provide an electric force for a longer time than short wavelength lasers.

3.2 Wavelength Scales in LWFA

Wavelength scaling benefits laser wakefield acceleration in numerous ways. Ponderomotive forces are the primary drivers of wakefields in both self-modulated and resonant laser wakefield experiments. Achieving strong wakefields allow electron acceleration to MeV or even GeV energy scales in a single accelerating stage. The obvious benefits of long-wavelength lasers comes from creating strong wakefields at modest intensities compared to Ti:Sapphire and Nd:Glass systems.

Additional properties related to laser wakefield acceleration also scale with laser wavelength. The laser strength parameter, a_0, is often written in the following form:

$$a_0 = \frac{e\overline{|E|}}{m_e \omega_l c} \tag{3.17}$$

This expression normalizes the momentum than an electron gains from an oscillating field *E* during 1/2π of a cycle to the "rest momentum" of an electron, $m_e c$. Through substitutions similar to those performed above, the expression is converted to the following form:

$$a_0 = \frac{e\sqrt{\mu_0}}{\sqrt{2} m_e c^{\frac{3}{2}}} \lambda \sqrt{I} \tag{3.18}$$

A common modification is looking at the square of the laser strength parameter. Making such a change and converting to specific input formats provides the following expression:

$$a_0^2 = 7.3 * 10^{-17} * \lambda^2[\mu m] * I\left[\frac{W}{cm^2}\right] \tag{3.19}$$

Again, incrementing wavelength by some percentage increases this quantity faster than a similar percentage increase in intensity. The peak a_0^2 value with all other considerations staying fixed also yields a steeper gradient, which is critical for the wakefield generation expression derived in Chapter 2.

Here is the equation for critical power of relativistic self-focusing from Chapter 1:

$$P_{cr} \approx 17\left(\frac{\omega}{\omega_p}\right)^2 GW = 17\left(\frac{2\pi c}{\omega_p \lambda}\right)^2 GW \propto \frac{1}{\lambda^2} \tag{3.13}$$

Equation 3.13 demonstrates that longer wavelength lasers require a lower critical power, again due to the phase cycle duration of the laser pulse increasing linearly with wavelength and thus inducing larger refractive index changes in the medium within a single cycle. A smaller critical power allows the onset of self-focusing at lower pulse energies. For

example, consider the critical power for both a CO_2 laser at 10.6 μm and Ti:Sapphire laser at 800 nm in a gaseous medium of $5*10^{17}$ cm^{-3} (plasma frequency of 39.9 THz). The Ti:Sapphire laser requires 59.2 TW to achieve self-focusing in such a medium, while a CO_2 laser requires only 337 GW.

The dephasing length from Chapter 2 is expressible in terms of density and λ

$$L_d \cong \gamma_p^2 \lambda_p \propto \left(\frac{1}{n_e}\right)\left(\frac{1}{\sqrt{n_e}}\right)\left(\frac{1}{\lambda^2}\right) = \frac{1}{\lambda^2 n_e^{\frac{3}{2}}} \tag{3.14}$$

The density must decrease to compensate for the shortening of the dephasing length at a longer wavelength. Additionally, the expression for wavebreaking field $\mathbf{E}_0$ is can be written in terms of density

$$E_0 = \frac{c m_e \omega_p}{e} \propto \sqrt{n_e} \tag{3.1520}$$

By combining these two dependencies in Eq. 2.16, the scaling behavior of maximum electron energy gain is estimated as:

$$W_{max} \propto \frac{1}{n_e \lambda^2} \tag{3.216}$$

Consequently, lasers must focus in lower densities to increase the electron energies. To accelerate higher energy electrons thus requires a less dense acceleration region, which the CO_2 can achieve with lower pulse powers than the prevalent ultrafast lasers. Lower powers also reduce the likelihood of other loss mechanisms from significantly disrupting the propagation of the laser, potentially improving the stability and repeatability of the laser-plasma accelerator.

3.3 CO_2 Lasers

While the scaling of properties with laser wavelength has many potential advantages, achieving ultrafast pulses at relativistic intensities is not trivial. Creating a laser

at a sufficiently long wavelength is not as simple as choosing the size of drapes. The lasing medium must be able to sustain a population inversion capable of producing the wavelength as well as persist under the intensity of the amplified light. Additionally, since the engineering challenges of any laser are substantial, there is the concern that even if a laser *can* be created at the desired wavelength that the construction and operation of a Ti:Sapphire or Nd:Glass system with higher energy may be cheaper in the long run.

CO_2 lasers are well positioned to satisfy the necessary conditions for a long-wavelength, ultrafast, ultra-high-power laser. Invented by Chandra Kumar Naranbhai Patel in 1963 [103], it has also been used for numerous scientific and industrial applications, including electron acceleration experiments in the 1980s [104]. The laser remains popular in industry [105] for its affordability and simplicity, but recent advances in long-wavelength lasers is causing increased research into its suitability as an experimental tool, especially as a wakefield driver. CO_2 lasers produce light at either 9.6 or 10.6 μm, yielding

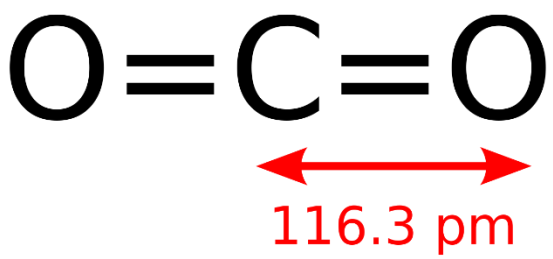

Figure 3.2: Diagram of bonds in a CO_2 molecule

a wavelength ratio of 10 compared to typical Nd:Glass lasers and 13.3 compared to typical Ti:Sapphire lasers. The resulting ponderomotive force gains are two orders of magnitude, translating into a 100 times lower intensity to achieve the same effect.

A detailed and helpful review of all aspects of CO_2 laser operation is provided by P. K. Cheo [106] from which the following discussion cites extensively.

CO_2 is a linear molecule consisting of an oxygen atom, a carbon atom, and another oxygen atom. In the ground state, the molecule holds the two oxygen at 180 degrees [107] [Fig. 3.2]. Linear molecules with N atoms possess $3N - 5$ degrees of freedom, in the form of the three translational dimensions and the remaining two rotational modes. These states

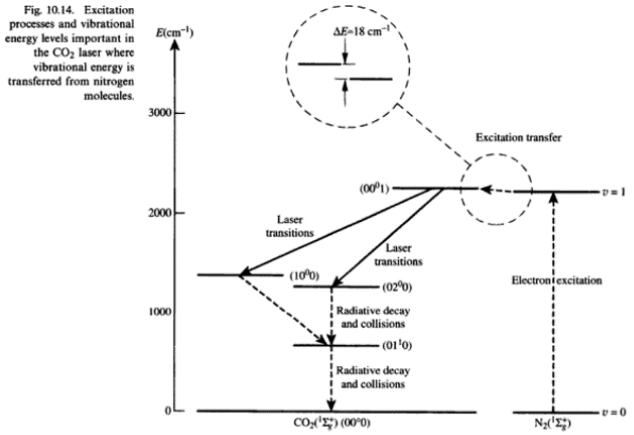

Figure 3.3: Population inversion diagram for the CO_2 laser system. N_2 molecules are excited by electron impact to the first vibrational state, which then exchange energy with CO_2 via collisions. The CO_2 asymmetric vibrational mode 00^01 decays into 10^00 for 10.6 μm light and 02^00 for 9.6 μm light. He atoms collide with the lower-state CO_2 to return them to the ground energy level.

are typically written in the Fermi resonance nomenclature of four numbers, $\nu_1 \nu_2^l \nu_3$, where ν_1 represents the symmetric vibrational mode, ν_2 represents the bending state with angular momentum number l, and ν_3 represents the asymmetric vibrational mode.

A common composition of the lasing medium of a CO_2 laser consists of a gas mixture of CO_2, N_2, and He. Electrons are discharged through the cathode across the gas mixture, which collide and excite the first vibrational state of nitrogen gas or the vibrational states of CO_2, although the former is the primary inversion mechanism. The excited nitrogen gas state is metastable due to the lack of a dipole moment necessary for spontaneous state transitions in homonuclear diatomic atoms, resulting in long relaxation

times. Excited nitrogen gas molecules can impact ground-state CO_2 molecules due to their similar energy levels, bringing them into the first asymmetric vibrational state 00^01 [108]. Laser transitions are made between the first symmetric vibrational state 10^00 (10.6 μm) and the second bending state 02^00 (9.6 μm), with the former being the strongest emission line and both states having lifetimes close to 4 ms. Both lower excited states have long relaxation times (~4.5 s). Ground-state CO_2 is recovered due to transitions from these lower excited states by collisions with He atoms. Helium atoms also mediate heat dispersal in the gas to prevent the formation of CO gas whose formation depletes the lasing medium over time and increase the effective lifetime of the 00^01 state of CO_2 due to energy transfer with the first vibrational state of CO. Many CO_2 lasers use a flowing gas medium to overcome these effects. Tuning of gas pressure, discharge current, and mixture composition are critical to excitation of the antisymmetric without exciting significant fractions of other states, but a discussion of these details is beyond the scope of this chapter.

The CO_2 laser is typically operated in a continuous fashion for industrial needs, but was used in a pulsed amplification stage for the experiments reported here. A more detailed account of the usage is covered in Section 3.4.

One of the greatest advantages of the CO_2 laser is the wall-plug efficiency, defined as the ratio of output pulse power to total incoming electrical power [109]. For a system designed for constant use with a high repetition rate, the cost of both the component parts as well as operating the laser are significant concerns, especially for lasers with multiple amplification stages. Gas lasers typically have high wall-plug efficiencies due to their design simplicity: an electrical discharge through inert gases in a contained space. By transferring energy to the medium with a minimal of efficient conversion operations, they reach actual wall-plug efficiencies between 5 and 25% depending on the specifics of the system. CO_2 lasers also tend to be robust due to the lack of an easily damageable medium

or expensive parts. These features are part of the reason for the popularity of CO_2 lasers in industry, although those are continuous rather than pulsed operations. Comparisons to the 3% wall-plug efficiency of flash-lamp-pumped Nd:YAG lasers, which also face significant probabilities of equipment deterioration and medium damage, are very favorable, although advancements in diode lasers may eventually cause this aspect to reach closer to that of CO_2 lasers. Ti:Sapphire lasers typically have still lower wall-plug efficiencies since they are pumped with other lasers in the green region of the visible spectrum, adding an additional layer of energy conversion.

3.4 BNL ATF CO_2 Laser

3.4.1 Laser Specifics

The pump laser used in the experiments presented here was the Brookhaven Experimental Supra-Terawatt Infrared at ATF (BESTIA), a CO_2 laser at Brookhaven National Laboratory (BNL)'s Accelerator Test Facility (ATF). It is one of two operational picosecond-duration CO_2 lasers, the other being UCLA's Neptune laser. ATF has a number

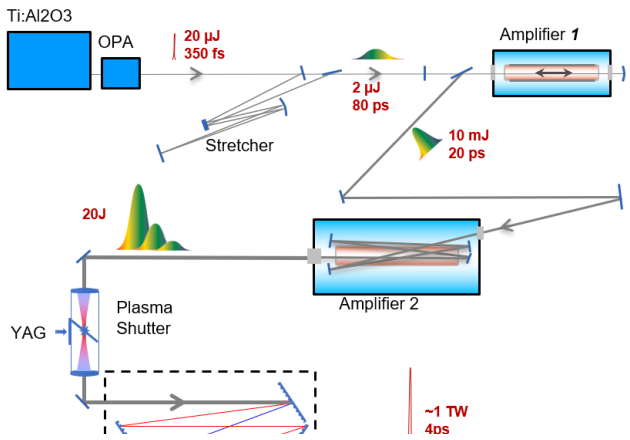

Figure 3.4: BNL ATF CO_2 laser configuration in April 2018

of other experimental instruments, such as an electron beam accelerator and Nd:YAG laser capable of being used in the same experimental hall.

Fig 3.4 depicts the configuration used in the April 2018 experimental run. The laser starts from an all-solid-state Ti:Sapphire system in the Master-Oscillator-Power-Amplifier (MOPA) configuration represented in Fig 3.5 [110]. A fiber-based oscillator and diode-pumped amplifier system are used before sending the pulse into a regenerative amplifier cavity that produces 7-mJ, 180-fs pulses at 785 nm heading towards the OPA stages [111]. Parametric down-conversion is performed in stages, beginning with transmission through a sapphire for white-light continuum production before entering a BiBO crystal for

amplification. A second BiBo crystal produces signal and idler pulses of 1.4-1.5 μm and 1.7 μm before the generation of difference frequency around 10 μm.

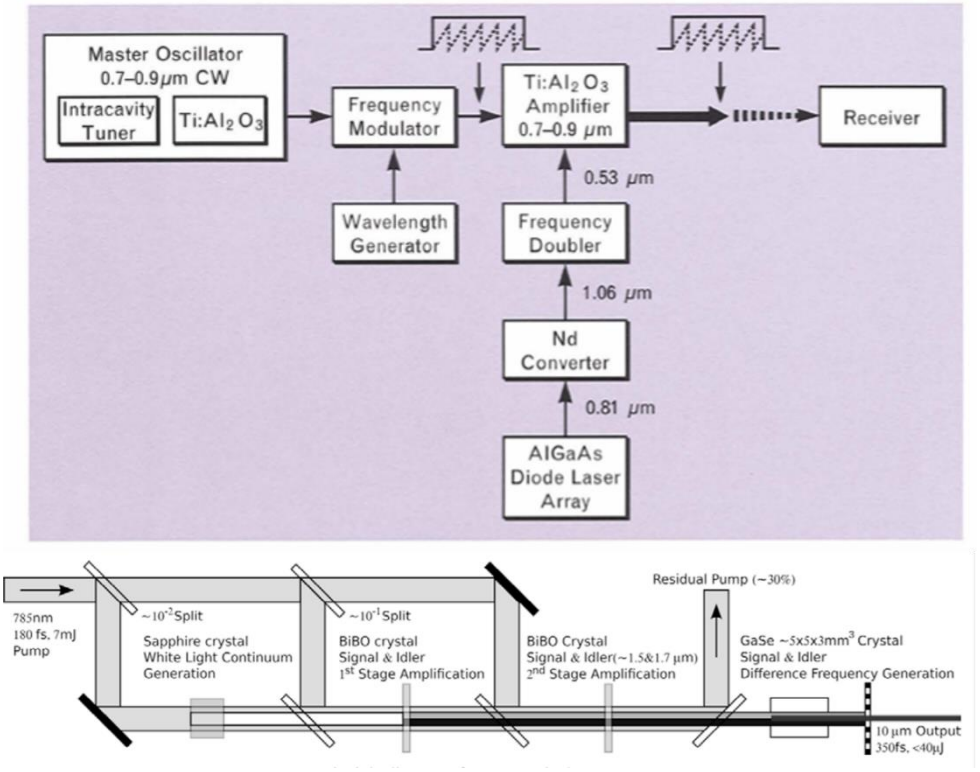

Figure 3.5: Block diagram of the MOPA configuration (top) and the OPA chain components (bottom)

The pulse is subsequently stretched for CPA on a grating which filters transmitted wavelengths outside the chosen rotational-vibrational branch (9R) of the gain medium. Fig. 3.6 demonstrates the transmitted wavelengths on the top with the gain profile for a 10-bar lasing medium with partial pressures for CO_2:N_2:He of 0.35:0.4:9.25 and equal split of O^{16} and O^{18} isotopes. The first amplification stage is a multi-pass regenerative amplifier with such a mixture, using a UV-preionized transverse electric discharge produce a gain of 10^4. Pulses exiting this stage have 10 mJ and durations of 20 ps.

The final amplification stage was one of the eventual three-chamber design, which is a single-pass transverse discharge chamber with windows large enough to prevent damage during the exiting pulse transmission. These pulses contain ~20 J of energy, which are transmitted through a plasma mirror to prevent back reflections. The plasma mirror mechanism is discussed in Chapter 5.

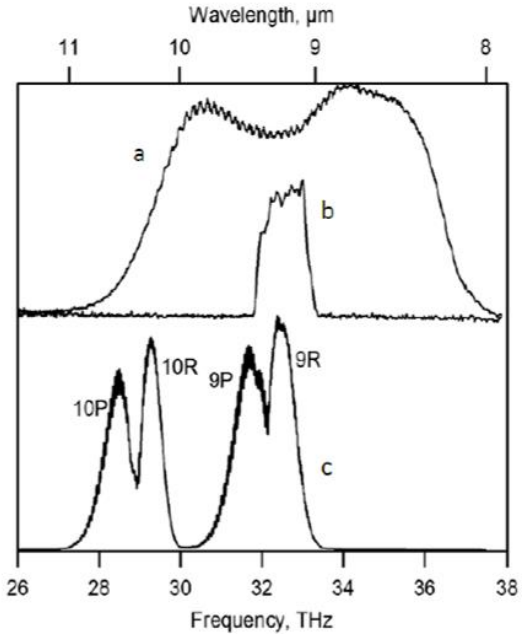

Figure 3.6: The BESTIA post-OPA spectrum (a) before and (b) after the stretcher. The corresponding CO_2 gain spectrum (c) highlights the rotational vibrational modes contained within the post-OPA spectrum.

The beam is compressed using gratings to a final pulse with 0.65 to 5.5 J and a duration of 4 ps. Fig 3.7 shows autocorrelation measurements of the CO_2 pulse duration at various energies. Below 5.5 J, the pulse duration is flat at 6 ps (the actual is reduced to 4 ps), but at higher energies begins to grow linearly with energy.

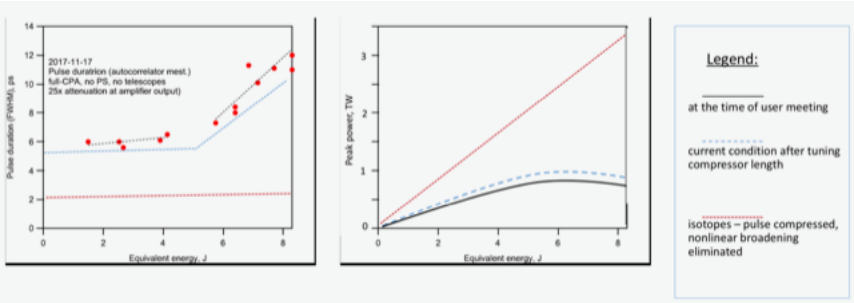

Figure 3.7: Pulse duration vs energy for BNL ATF CO_2 laser

Work in the spring of 2019 at BNL has demonstrated a pulse duration of 1.7 ps extending all the way through 14 J.

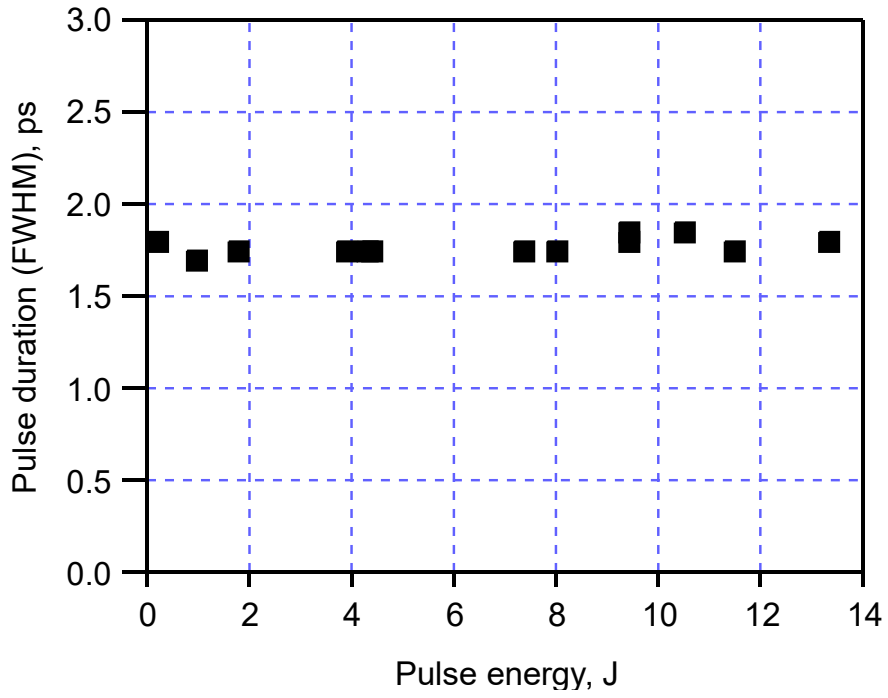

Figure 3.8: Pulse duration vs pulse energy for BNL ATF CO_2 laser in March 2019

3.4.2 Future Developments at ATF

An eventual goal for the BNL ATF CO_2 laser is to reach pulse durations short enough to stimulate resonant laser wakefield in a plasma. For a hydrogen plasma in the low-density range of the experiments presented here ($5*10^{17}$ cm^{-3}), a pulse duration of ~150 fs is necessary.

Collaborators at ATF are working to broaden the gain spectrum of the medium [112]. The aforementioned 50:50 O^{16}:O^{18} isotopic mixture increases the rotational line density by a factor of 4, smoothing the gain curve at lower gas pressures. If all the isotopes of C and O are included into the mixture, the spectral continuum spans 7 THz, corresponding to a transform-limited pulse duration of 100 fs. Additionally, gaseous pulse compression techniques can shorten the pulse close to the transform limit without introducing strong nonlinearities inherent in transmissive optics.

Chapter 4: Laser Wakefield Probing Techniques

Observing the properties of an electron plasma wave during its interaction with a laser pulse provides valuable insight into the details of the internal state. This chapter deals with the probing techniques used to measure electron density variations within an ionized hydrogen gas jet irradiated with a CO_2 laser. After discussing probing methods at large, special focus will be paid to collective Thomson scattering. Following that discussion, a derivation of a method utilizing the amplitude ratio of neighboring orders of probe spectral sidebands will demonstrate how wakefield amplitudes are measured.

4.1 Thomson Scattering Mechanisms

Light scattering from free plasma electrons is known as Thomson scattering. A common metric for the type of Thomson scattering that electromagnetic waves will experience in a plasma is the plasma parameter [113]:

$$\alpha = \frac{1}{k\lambda_D} \tag{4.22}$$

where k is the wavevector of the electromagnetic wave and λ_D is the Debye length of the plasma. A full expression for the Debye length of a plasma is given by the following:

$$\lambda_D = \sqrt{\frac{\epsilon_0 k_b / e^2}{\frac{n_e}{T_e} + \Sigma_j \frac{Z_j^2 n_j}{T_j}}} \tag{4.23}$$

where T_e is the electron temperature, Z_j is the charge of the *j*th ion, and T_j is the temperature of the *j*th ion. In circumstances where $T_e >> T_j$ for all j, the electrons move swiftly enough to account for the majority of the electrostatic behavior in the plasma. As such, Equation 4.2 simplifies to

$$\lambda_D = \sqrt{\frac{\epsilon_0 k_b T_e}{n_e e^2}} \tag{4.24}$$

When the scattering parameter $\alpha < 1$ – known as the non-collective Thomson scattering regime – the wavelength of the laser is smaller than the Debye length, allowing photons to interact with free electrons and thermal effects to be observed within a sphere with a radius of the Debye length [113]. The thermal characteristics of the electrons, which are described by a Maxwell-Boltzmann velocity distribution, imprint themselves on the photons. The result is a spectrum which is centered at the original electromagnetic wavelength broadened by an amount dependent on the temperature of the electrons (Figure 4.1, bottom image).

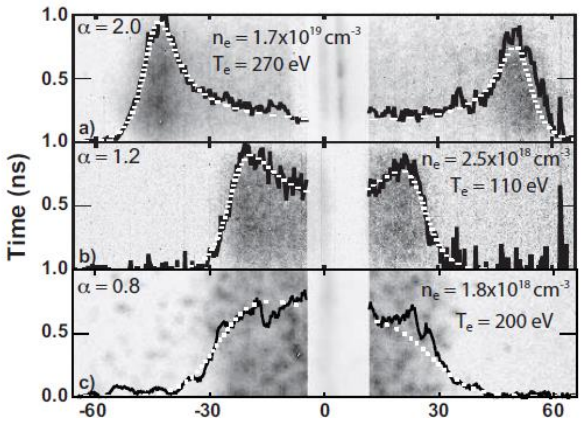

Figure 4.1: Thomson scattering from a plasma diagram by Froula showing various values of α. The top image is an example of collective Thomson scattering, with clear divisions of Stokes and anti-Stokes signals. The bottom section demonstrates a Maxwell-Boltzmann distribution of frequency shifts centers around the central probe value. The middle section demonstrates the transition between the two extremes.

As α increases above 1 – known as the collective Thomson scattering (CTS) regime – the laser wavelength becomes too large to interact directly with single electrons. Instead, the electron plasma oscillations appear as a grating in the plasma refractive index [114]

$$\eta(\boldsymbol{r},t) - \eta_0 = \sqrt{1 - \frac{n_e + \delta n_e(\boldsymbol{r},t)}{n_c}} - \eta_0 \approx \frac{2\delta n_e(\boldsymbol{r},t)}{n_c} \tag{4.25}$$

where η_0 is the background plasma refractive index, $\delta n_e(\mathbf{r},t)$ is the local difference from the background electron density n_e, and n_c is the critical density of the plasma. The approximate expression on the right side of Equation 4.4 is valid when $\omega_{pr} >> \omega_p$. The critical density is the electron density needed to achieve the plasma frequency. It demarcates at which frequencies electromagnetic waves are unable to propagate in the plasma.

The effect of the grating is phase-modulation of the probe, scattering the light with frequencies of $\omega_0 \pm \omega_p$ and wavevectors of $k_0 \pm k_p$. These are the satellite or sideband signals of collective Thomson scattering. The nomenclature for describing the shifts is taken from Raman spectroscopy, so down-shifted sidebands ($\omega_0 - \omega_p$) are known as Stokes signals and up-shifted sidebands ($\omega_0 + \omega_p$) are known as anti-Stokes signals. Due to continuous propagation of the light through the plasma, multiple orders of sidebands can occur from single-shifted light experiencing subsequent scattering events. Note that this scattering mechanism resembles the Forward Raman scattering instability. However, probe energies are tiny compared to the pump, so they do not affect the plasma and do not undergo a similar mutual modulation feedback cycle.

Collective Thomson scattering probes are clearly useful for density measurements of a plasma. The typical experimental parameter controlled to adjust plasma density is the gas jet backing pressure. The electron density of an ionized plasma varies approximately linearly with gas jet backing pressure. By combining Eqs. 2.7 with the equation for the plasma frequency, it is apparent that the CTS sideband shifts increase with the square root of the plasma density observed by the probe. A set of such measurements at varying pressure settings were performed at the start of each experimental run to confirm the proper operation of the laser and gas jet.

When the interaction between the probe and the electron plasma wave is transverse, the scattering angles of the probe is restricted to discrete angles [114]

$$\theta \approx \frac{|k_p|}{|k_0 \pm k_p|} \tag{4.26}$$

leading to spatially separated primary probe and scattered values. For $k_0 >> k_p$, the scattering angle is small and the light will propagate in a mostly forward direction. For the experiments reported here, the probe had a k_0 of $1.2*10^7$ m^{-1}. By comparison, the most extreme value of the plasma wavevector k_p occurred for the plasma density of $3*10^{18}$ cm^{-3}, which was $3.3*10^5$ cm^{-3}. The majority of shots were taken at much lower densities, which translates to much lower k_p values.

The scattering efficiency of probe light is dependent on numerous physical properties. Slusher and Surko [115] derived an expression for the proportion of the scattered light of an electromagnetic wave propagating in a plasma wake:

$$\frac{P_{scatter}}{P_0} = \frac{(\delta n_e)^2 r_0^2 \lambda_0^2 L^2 \sin(\Delta k L)^2}{4(\Delta k L)^2} \tag{4.27}$$

where $P_{scatter}$ is the power of the scattered light, P_0 is the initial probe power, δn is the plasma oscillation amplitude as a ratio of the ambient electron density, r_0 is the classical electron radius, λ_0 is the vacuum original laser wavelength, and L is the propagation distance in the medium. Δk is the wavevector mismatch defined as $\Delta k = k_0 - k_{scatter} \pm k_{plasma}$. The sinc-squared function is a common feature of phase-matching expressions for sum and difference frequency generation [116]. Equation 4.6 predicts a higher efficiency for anti-Stokes light at relatively small shifts, i.e. within the first zeros of the sinc-squared function. While this expression is useful for a theoretical description of scattering, both the plasma oscillation amplitude and length of propagation are often not known with precision in experimental situations, limiting the applicability in practice.

In addition to electron mobility, the ions move under the influence of an intense laser fields as well. An analogous ion plasma frequency for an ion of charge Z and mass

m_i is found by replacing the electron mass with the ion mass and the electron charge with Ze in Eq. 1.56:

$$\omega_{p_i} = \sqrt{\frac{n_i Z^2 e^2}{\epsilon_0 m_i}} \tag{4.28}$$

This frequency defines the lower limit of ion oscillation motion which is greater than the ion thermal motion. However, in the case where the Debye length of the plasma is small compared to laser wavelength (i.e. the CTS regime), the dispersion equation simplifies to resemble that of an acoustic wave for the ions [117]:

$$\frac{\omega}{k} \propto \sqrt{\frac{k_b T_e}{m_i}} \tag{4.29}$$

Note that the phase and group velocities of this wave are identical. For realistic electron temperatures, the group velocity of such waves is significantly slower than the electrons with a much smaller frequency. Even if a signal were present, the use of a notch filter on the central probe wavelength in the experimental setup would suppress it completely.

While the above description is sufficient for the work performed in this thesis, a more thorough treatise of Thomson scattering physics is available [118].

4.2 Determining Wake Amplitudes from Multi-Order Stokes/Anti-Stokes Sidebands

A crucial component of the scattering efficiency formula (Eq. 4.6) is the dependence on the square of the plasma wake amplitude, δn_e. Regions of large wake amplitudes scatter light more effectively, leading to stronger signals at sidebands wavelengths. As the wake amplitude approaches 1, the local power of 1st-order and 2nd-order CTS sidebands will become close to equal. This insight was used by Umstadter, et al., [119] to demonstrate a method for estimating wake amplitudes from measured sideband data.

Umstadter used harmonic analysis to construct wakefield amplitude estimates. As the wakefield amplitude increases, the linear description fails to capture all of the details of the dynamics. A nonlinear wakefield is representable by a Fourier decomposition of its component parts. These components give rise to the collective Thomson scattering of the various orders. The derivation of the appropriate expressions below follows this approach.

The harmonic amplitudes of a plasma wave can be expressed as the powers of the normalized wakefield amplitudes used in the following equation:

$$\frac{n_m}{n_0} = \alpha_m \left(\frac{n_1}{n_0}\right)^m \tag{4.30}$$

where n_0 is the background plasma density, n_1 is the amplitude of the linear wakefield, n_m is the amplitude of the *m*th harmonic, and α_m is the coefficient of the *m*th harmonic. The 2nd-harmonic corresponds to the scattering plasma wake responsible for the 1st-order Stokes or anti-Stokes signals, with equation:

$$\frac{n_2}{n_0} = \alpha_2 \left(\frac{n_1}{n_0}\right)^2 \tag{4.31}$$

Similarly, the 3rd-harmonic signal corresponds to the 2nd-order Stokes or anti-Stokes scattering from the plasma wake:

$$\frac{n_3}{n_0} = \alpha_3 \left(\frac{n_1}{n_0}\right)^3 \tag{4.32}$$

For a cold plasma, $\alpha_2 = 1$ and $\alpha_3 = 1.1$ respectively. By substituting Eq. 4.11 into Eq. 4.10, the combined term becomes:

$$\frac{n_3}{n_0} = 1.1 * \frac{n_1}{n_0} * \frac{n_2}{n_0} \tag{4.33}$$

Simple multiplication results in the expression:

$$\frac{n_1}{n_0} = 1.1 * \frac{n_3}{n_2} \tag{4.34}$$

By the scattering efficiency formula, the plasma density is known to be proportional to the square of the wake amplitude. Converting to scattered power ratios using Eq. 4.6 and changing the subscripts to reflect the sideband order, the final expression has a form:

$$\frac{n_1}{n_0} = \delta n_e \approx \sqrt{\frac{P_2}{P_1}} \tag{4.35}$$

where P_1 is the power of the 1st-order scattered light and P_2 is the power of the 2nd-order scattered light. This method is extendable to higher orders with knowledge of the appropriate coefficients. By finding the ratio of the power of two neighboring sideband orders, the linear wakefield amplitude is estimated. Not needing to specify the length of interaction makes Eq. 4.14 useful for practical measurement of wakefield amplitudes.

Previous experimental work used Eq. 4.6 to measure wakefield amplitudes. Ting, et al., [120] used a Ti:Sapphire/Nd:glass laser (λ = 1.054 μm) with duration 400 fs and energy of 800 mJ – reaching a peak intensity of $7*10^{18}$ W/cm^2 – to generate self-modulated laser wakefields in a gas jet of helium or hydrogen with densities in the range of 10^{19} cm^{-3}. A frequency-doubled probe with energy of 10 mJ and duration less than 1 ps propagated collinearly with the pump beam. The ratio of the scattered probe intensity to incident probe intensity was used to estimate wakefield intensity directly from the scattering efficiency equation, using the confocal parameter of the probe laser (200 μm) as an estimate of interaction length. The resulting measurements showed wakefield amplitudes as high as 10% of the background plasma density.

LeBlanc, et al., [121] utilized the power ratio approach in Eq. 4.14 instead. A Ti:Sapphire/Nd:glass system at 1.053 μm provided pulses of 3 J and 400 fs, with a peak intensity of $6*10^{18}$ W/cm^2. The pump pulse was focused into a supersonic helium gas jet with an electron density of $3*10^{19}$ cm^{-3}. Approximately 20% of the initial pulse energy was frequency doubled, then copropagated with the pump pulse as a probe with 15 mJ in 300 fs. The resolution of the time overlap was 100 fs using frequency domain interferometry. Measured plasma waves amplitudes varied between 8% and 40% of the plasma density. In the region where these amplitudes were observed, a collimated beam of 2 MeV electrons

was emitted in the propagation direction. Fig. 4.2 shows a) a waterfall plot of the Stokes and anti-Stokes signal as a function of delay and b) the outline of a plasma wakefield constructed by measuring the estimated wakefield amplitudes from both Stokes and anti-Stokes light at different delays. The signal strength of the sidebands increases in 4.3a as the delay between the pump and the probe decreases. Note the qualitative agreement in 4.2b between the Stokes and anti-Stokes profiles of the plasma wake. One possible reason for the disparity are lack of corrections due to variation in the detector sensitivity based on wavelength, especially if a CCD camera was used.

4.3 Practical Probe Considerations

Theoretical estimates of the conditions under which self-modulated laser wakefields will capture, trap, and accelerate electrons are challenging due to the highly nonlinear processes involved. Injection occurs close to the wavebreaking field, as discussed in Chapter 2, and the onset of strong Stokes/anti-Stokes signals is a precursor to observation of accelerated, self-injected electrons. The wavebreaking electric field calculations assumes a 1D cold plasma as the medium. The experimental results by LeBlanc imply that either the threshold for significant electron acceleration is lower than the wavebreaking field or considerations of the probe details must adjust the measurements. Tzeng, et al., [122] performed full PIC simulations to observe the dynamics of wavebreaking in detail. They observed a substantial number of trapped electrons for electric fields as low as 25% of the wavebreaking limit, implying that injection occurs far below the approximate metric.

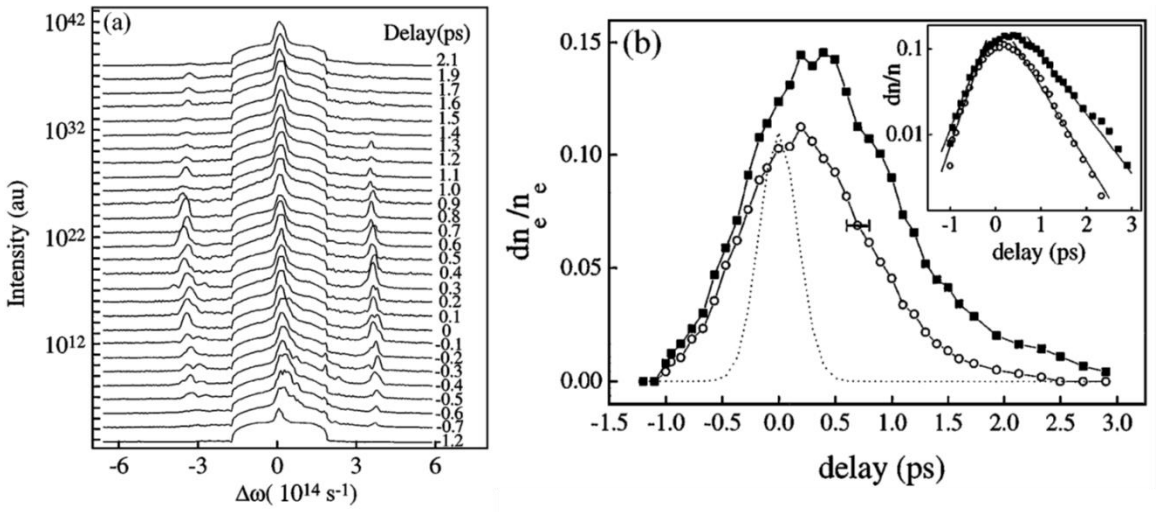

Figure 4.2: Pictures from LeBlanc. a) Waterfall diagram of intensity versus frequency showing the primary probe pulse (center) along with the Stokes (left of center) and anti-Stokes (right of center) shifts as a function of delay. b) Normalized amplitude measurements using the Stokes (black squares) and anti-Stokes (white circles) signals. The probe pulse is modeled with the dashed line. The inset displays exponential fitting of the wakefield growth and decay.

There are several practical considerations that adjust the estimates of the sideband powers in an experiment. A spatially large probe beam will scatter light over the entire wake region. In the experimental setup used for the work in this thesis, the cross-section of the probe is an order of magnitude larger than the pump to ensure the entire spatial dimension of the interaction region was included in each shot regardless of pump jitter. Since linear wakes propagate beyond the transverse extent of the pump, it is reasonable to expect a larger absolute signal of 1st-order sidebands due to increased opportunities for scattering. The region in which higher-order sidebands is efficiently generated may constitute a small portion of the probe volume, reducing the observed power ratio.

An ideal probe will also have a short duration since the probe accumulates signal based on its longitudinal extent. A linear wake persists for a long time after the laser pulse

(measured to be on the order of 10 ps in our experiments; see Chapter 6 for more details). The probe duration for the work performed in this thesis was nearly identical to the pump duration (~4 ps), with the preferred temporal offset to achieve the largest sideband signals coming when the probe slightly trailed the front section of the pump.

Additionally, a spatially and temporally extended probe has a lower energy density throughout the region. While the spectrometer camera had a high sensitivity and all probe wavelengths were near the peak of the quantum efficiency curve (~95% QE), the spectral region also exhibited a strong plasma continuum background. While efforts were made to correct for this signal, it effectively lowered the signal-to-noise ratio of the probe. Consequently, the measured 2^{nd}-order sideband power is reduced or even completely obscured by these artifacts.

The combined effects of the large spatial and temporal extent of the probe as well as spectrally broad plasma continuum noise near 532 nm indicate that taking the absolute power ratios of 1^{st}-order and 2^{nd}-order light will underestimate the wakefield amplitudes unless the contribution of background light sources is properly subtracted from the data. However, the observation of higher-order sidebands that are a significant fraction of 1^{st}-order sidebands is still likely to correlate with the injection and acceleration of electrons. A 2^{nd}-order Stokes signal that has 1% of the power of the 1^{st}-order Stokes signal which is visible above the noise floor with our experimental parameters indicates significant secondary scattering in the volume, implying a non-trivial wakefield.

4.4 Spectral Splitting of CTS Signals

For high-power lasers, the transverse acceleration of the electrons due to the laser electric field can cause the background electrons to gain relativistic mass. This mass gain is reflected in a correction to the plasma frequency:

$$\omega_p = \sqrt{\frac{n_e e^2}{\epsilon_0 \gamma m_e}} \tag{4.36}$$

where γ has the form

$$\gamma = \sqrt{1 + \frac{a_0^2}{2}} \tag{4.37}$$

The resulting frequency shift of a collective Thomson scattered photon also changes:

$$\omega' = \omega \pm \frac{\omega_p}{\sqrt{\gamma}} = \omega \pm \frac{\omega_p}{\sqrt[4]{1 + \frac{a_0^2}{2}}} \tag{4.38}$$

From the formula, it is apparent that this effect is only noticeable when the laser is sufficiently relativistic ($a_0 \geq 1$). Spatially large and temporally long probe pulses like the ones used in the Fall 2016 and April 2018 experiments will often acquire linear and nonlinear (i.e., relativistic) CTS signals simultaneously due to their integration of all signals along the propagation path. These signals will be discussed further in Chapter 6.

Chapter 5: Experimental Setup

The experimental setup at BNL's Accelerator Test Facility is described in detail. Attention is paid to the probe beam modifications before and after the vacuum chamber. In-depth diagrams and pictures of the experimental setup are provided where possible. Figure 5.1 displays a useful simplified model of the experimental setup.

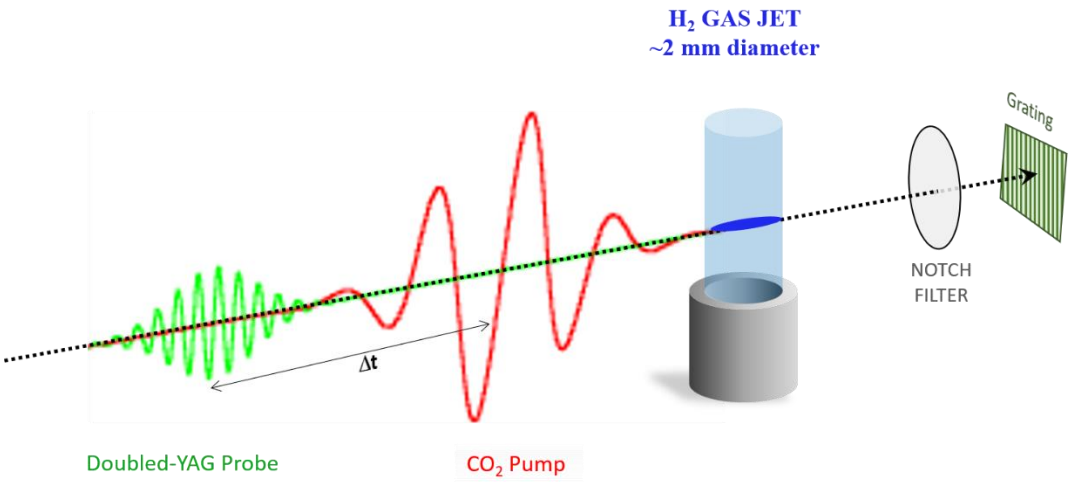

Figure 5.1: Experimental setup conceptual diagram.

5.1 CO_2 Pump Beam Transport

The 10.6-μm CO_2 pump beam was capable of achieving between 650 mJ and 5 J, measured using a power meter, while maintaining a pulse duration of 4 ps FWHM. Intensities at the focus of a f/3 off-axis parabolic mirror ranged from $1.3*10^{16}$ to 10^{17} W/cm^2 with a beam waist of 20 μm. A practical repetition rate of one shot in one to two

minutes was achievable when operating with one person operating the pump laser and two to three people managing the experimental setup.

During preliminary runs, the CO_2 was transported directly to the chamber via copper mirrors, being compressed by four gratings shortly before entrance. However, at high pressures, the lowest frequencies of the pump spectrum were below the plasma frequency of the ionized gas jet, resulting in significant back reflections which were then amplified when passing back through the CO_2 amplifiers. The amplified beam damaged upstream optics, causing problems for continued operation.

Inclusion of a plasma mirror was introduced to stop back reflections as the maximum pump energy was increased from 2 J to 5 J. The initial solution involved the use of a silicon wafer which was transparent to the CO_2 laser. After the CO_2 beam passed through, a separate YAG laser was used to excite electrons into an upper state which then blocked the reflections. However, the transmission of the CO_2 beam through a flat surface resulted in beam distortions which caused non-normal pump modes at the gas jet. To remedy this issue, the CO_2 beam was focused in vacuum and passed through a tungsten pinhole. The second YAG laser was then used to generate a plasma plume out of the tungsten, which prevented back reflections.

A CO_2 beam profile was recorded from the reflection light using a pyrocamera on the majority of shots, capturing ~7% of the pump light. The profiles were used to observe changes in beam shape between different shots as well as to measure the centroid jitter and pump energy. The centroid was fairly stable over the course of a day. Summed profile energy was linear with the recorded pump energy measurements as expected, achieving coefficients of determination around 0.9 for each day (Figure 5.2).

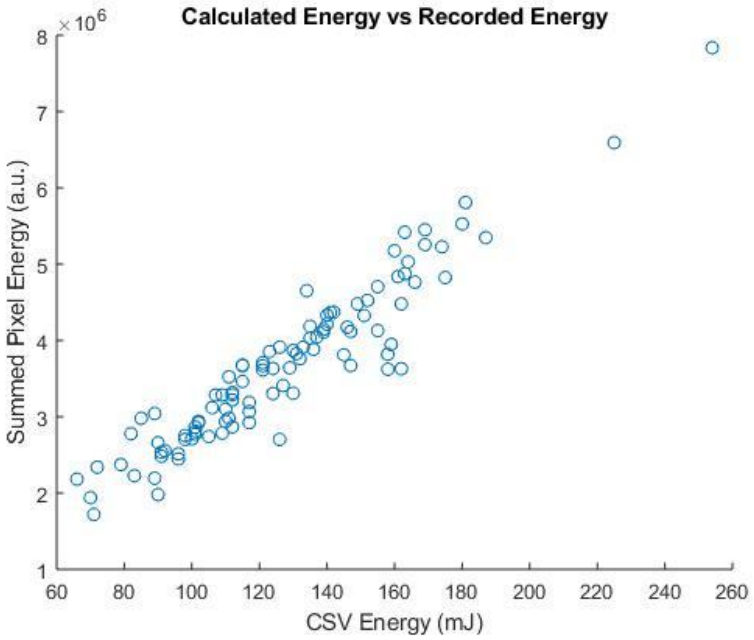

Figure 5.2: Correspondence between camera summation CO_2 energy values and power meter reported energy values

Noticeable changes to the pump beam shape were observed when the pump energy increased significantly above 1 J. Fig. 5.3 shows what the CO_2 pump profile looks like for various energies. All the pictures use the same scale. As the measured pump energy increases, the profile undergoes asymmetric increases in energy, likely due to the pump not being centered on the plasma mirror aperture.

The software used to examine the experimental data simultaneously displayed the pump and probe profiles as well as the probe spectrum of each shot in a single window. When the spectral characteristics of a higher-energy shot were modulated strongly, it was not uncommon to see a heavily asymmetric CO_2 profile. This additional spatial dependency of energy added to the difficulty of making reasonable analysis of high-energy shots.

After the interaction region, the remaining energy of the CO_2 pump is dispersed in the exit port window.

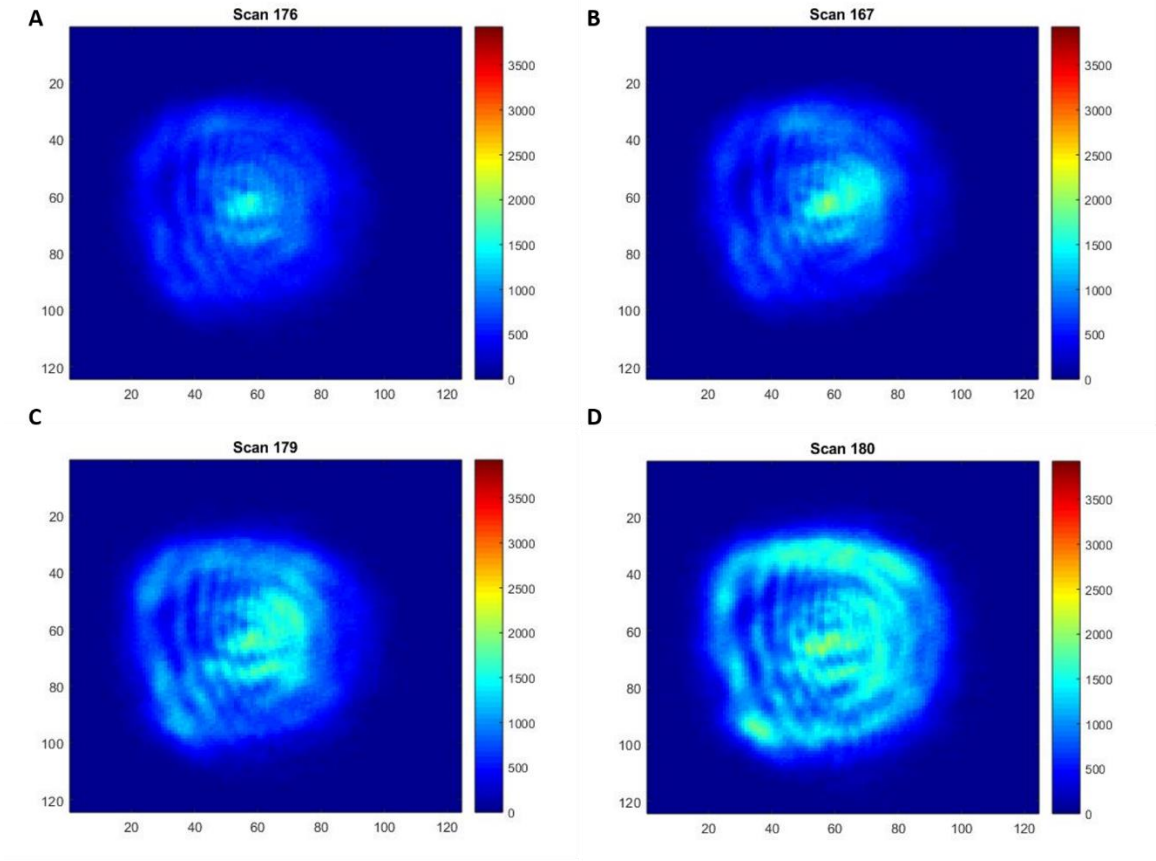

Figure 5.3: CO_2 pump profiles for increasing energies a) 1,044 mJ, b) 1,380 mJ, c) 1,668 mJ, and d) 3,168 mJ. While the first pulse is fairly symmetric, each energy increase corresponds with the development of more structure.

5.2 YAG Probe Beam Modification and Transport

The initial YAG pulse generated in the ATF YAG facility had energy of several mJ when entering the room. It underwent double-pass amplification in a Nd:YAG crystal encased in a housing for flashlamps, bringing its energy to 30-40 mJ, before undergoing frequency doubling.

The primary purpose for amplification of the YAG is to reach intensities necessary for nonlinear phase matching, in which the fundamental beams are depleted [123]. Typical

amplification voltages of 1600 V were to generate frequency-doubled pulses. A KDP crystal is used for type-II phase matching which compresses the initial 14-ps YAG beam into a 4-ps doubled-YAG pulse. Before the crystal, the probe enters a beam splitting configuration to decompose it into ordinary and extraordinary polarizations. A delay is introduced between the polarizations. The crystal's birefringence allows the retarded wave to overcome the leading wave within the crystal. In the frame of reference moving at the group velocity of the generated second harmonic, the two polarizations move in opposite directions. The second harmonic is generated from the overlap at the entrance of the crystal, quickly extracting energy from the fundamental pulses. Once the depletion of one of the short temporally overlapping regions of the pulses is total, second harmonic generation ceases. Proper choice of entrance angles leads to optimal walkoff speeds to produce a temporally shortened pulse. Fig. 5.4 shows simulated input profiles as well as an output profile.

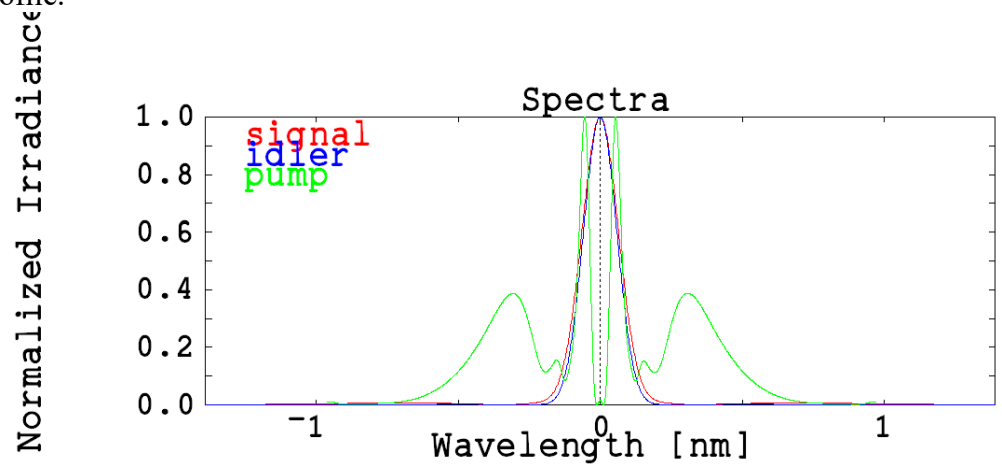

Figure 5.4: Simulation of the frequency doubling signals.

The doubled-YAG (532 nm) copropagating probe beam is then transported to an f/62.5 lens to achieve a beam waist of ~50 μm based on measurements at the focus in

vacuum. The probe energy at the focus was typically between 1 and 2 mJ, decreasing slowly during the day as fluctuating parameters caused drift in the beams entering the doubling crystal. The energy standard deviation was typically between 5 and 7% over an average of fifty shots.

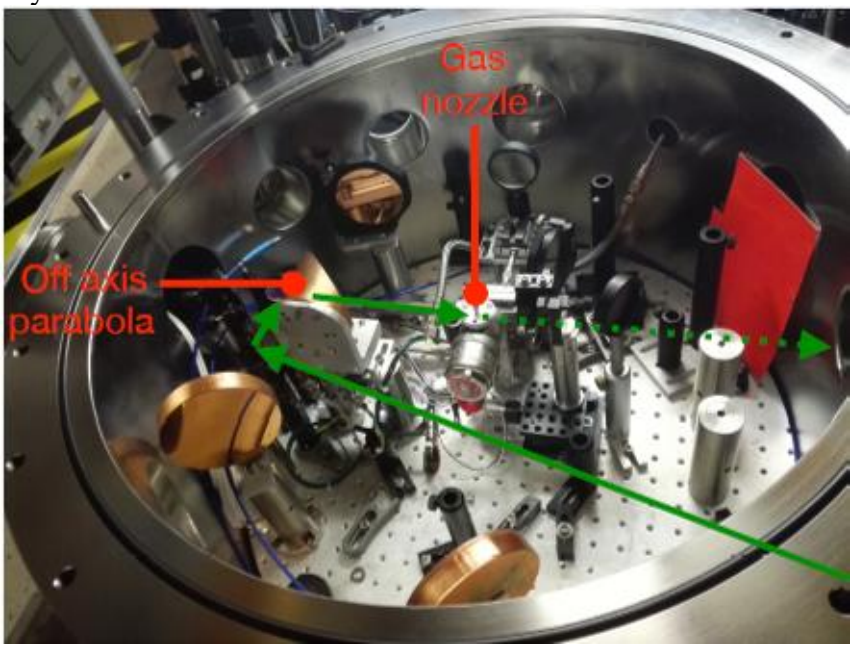

Figure 5.5:Gas chamber picture

5.3 Vacuum Chamber and Gas Jet

The vacuum chamber was maintained at 1e-5 torr for the experiments.

The CO_2 pulse entered the chamber through a salt window, being directed to an off-axis parabola for the pump that had a hole in which the probe was able to propagate through. The gas jet was movable under vacuum by remote control in the vertical direction and at roughly 45 degrees to the direction of propagation. An exit port led to the optics for directing the probe to the spectrometer.

The probe clearly subsumed the pump pulse, with focuses as spatially and temporally close as was reasonable to achieve. Both the pump and probe were spatially centered on a tungsten wire of 60 um diameter. The CO_2 pump would start sparking when significant portions hit the wire. Approximate lateral and transverse positioning of the probe was subsequently found. Temporal overlap was determined using a silicon wafer.

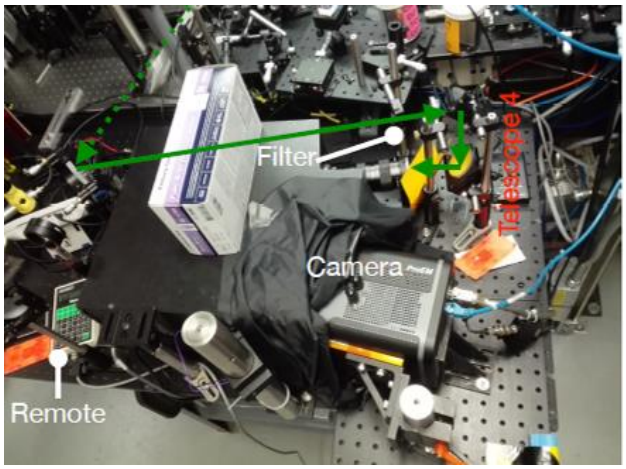

Figure 5.6: a) Probe exit path from the vacuum chamber, focusing and redirecting the beam. b) Beam splitter sends 10 percent of the energy to a profile measurement camera and 90 percent to the spectrometer

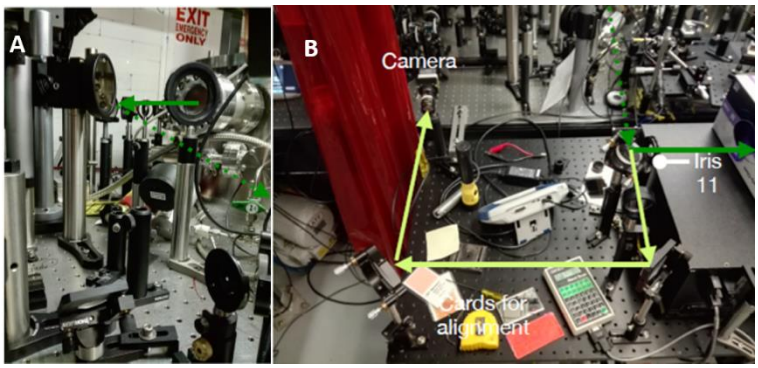

Figure 5.7: An image of the beam path to the entrance of the spectrometer. A notch filter blocks the primary probe beam before it is positioned by a telescope onto the entrance slit of the spectrometer.

Exposure to the doubled YAG laser caused a short-lived plasma plume to block any CO_2 light, allowing relative time delay within a few ps to be found.

5.4 Post-Chamber Optics, Imaging Spectrometer, and Probe Profile Camera

After the vacuum chamber were a focusing lens and a mirror used to transmit the probe to the imaging diagnostics (Figure 5.6a). The scattered probe light is transmitted approximately 2 meters to a 90/10 mirror (Figure 5.6b) The majority of the light is brought to a SPEX 270M imaging spectrometer with a Princeton Instruments ProEM 1024B camera (Figure 5.7). The grating yielded a spectral region spanning 37 nm around 532 nm.

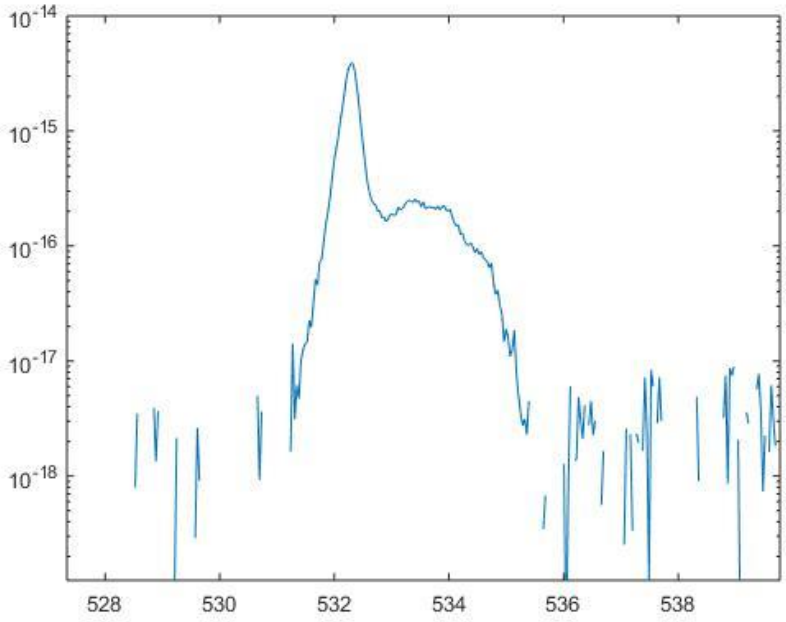

Figure 5.8: A spectral image of the primary probe on the slope of the notch filter in vacuum. The central peak remains clearly visible while its edge undergoes modulations from the changing optical density with wavelength.

A notch filter with peak optical density of 6 and a 14-nm FWHM centered at 532 nm was placed before the probe entered the spectrometer. Rotation of the notch filter from

normal led to a blue shift of several nm. Even with the notch filter, the primary probe pulse was observable in the spectrum for the last run due to this blue shift. In these shots, the probe lies on the notch filter slope (see Figure 5.8).

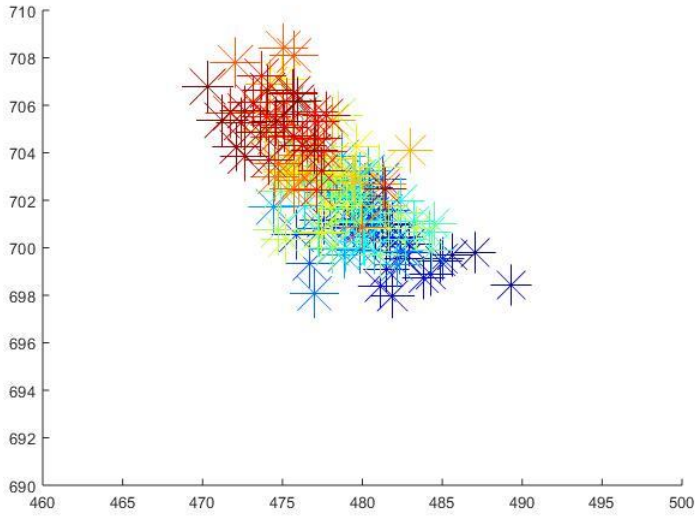

Figure 5.9: Pixel locations of probe centroid over the course of a day. The color spectrum goes from red to purple to indicate the time evolution, detailing the slow drift over the course of the day.

The remaining light was brought to a camera approximately a meter away to observe the final probe profile. Neutral density filters between 5 and 6.5 OD were placed in front of the camera to prevent damage while still allowing profile detail to be measured. The centroid of each shot within a day was measured and compared to the others to see the stability of the output. The color of each point in Fig. 5.8 is used to determine the order in which it was taken, with red corresponding to the start of the day and purple being the end. There was a drift over the course of the day, corresponding to approximately 15 diagonal pixels of 6.45 μm squares or ~130 μm total. Given the 3-meter propagation length, such a drift corresponds to a small shift at the focus.

Attempts at measuring electrons were performed in Fall 2016 using a EJ-260 scintillating material. In the few shots that were taken, no scintillation was observed. The scintillating properties indicate that a 1-MeV electron would produce 9,200 photons, far above the 14-photon sensitivity of the camera. As such, no electron acceleration measurements are reported in any of these experimental runs.

Chapter 6: Experimental Results and Discussion

This section discusses the results observed from two experimental runs at the Accelerator Test Facility at Brookhaven National Laboratory, one in the fall of 2016 and one in the spring of 2018. An overview of the observed collective Thomson scattering (CTS) probe spectral structure is given to help the reader identify the key features. Discussion begins with the results of the CTS density probing method. The CTS probe spectra allow observation of changes in structure and evolution of the plasma wave. Detailed consideration of the probe signals of nonlinear wakefields follow.

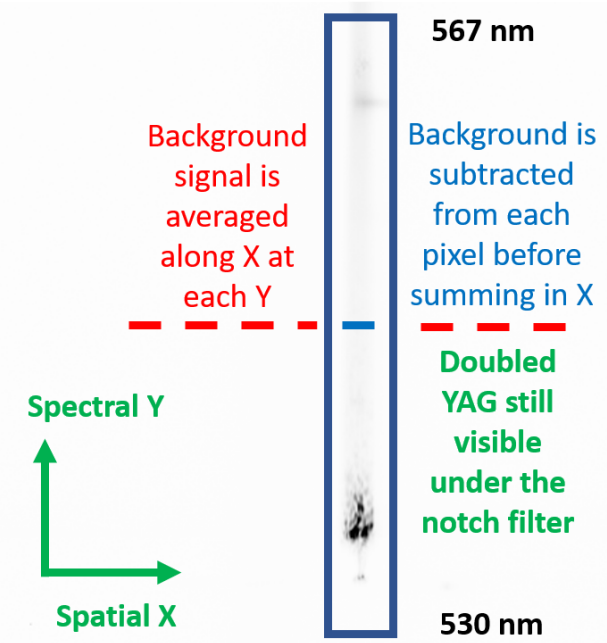

Figure 6.1: Raw spectrometer data. The background signal is averaged horizontally (red dotted lines), then subtracted from each pixel at the same Y value. The averaged pixel signals at each Y value within the blue box are plotted versus

Chapter 6.1 CTS Probe Measurements

The primary analysis tool for this experiment was the co-propagating CTS probe. After initial alignment and testing procedures were completed, roughly 500 shots were taken in the Fall 2016 run and 750 were taken in the April 2018 run. The best available spectrometer grating provided a 37-nm spectral region around 532 nm. Spectral lineouts were constructed by calculating a background average of pixels along each line perpendicular to the spectral output, subtracting it from each active pixel in the region, then summing the active pixels along this axis. An example of the raw spectrometer output is display in Figure 6.2.

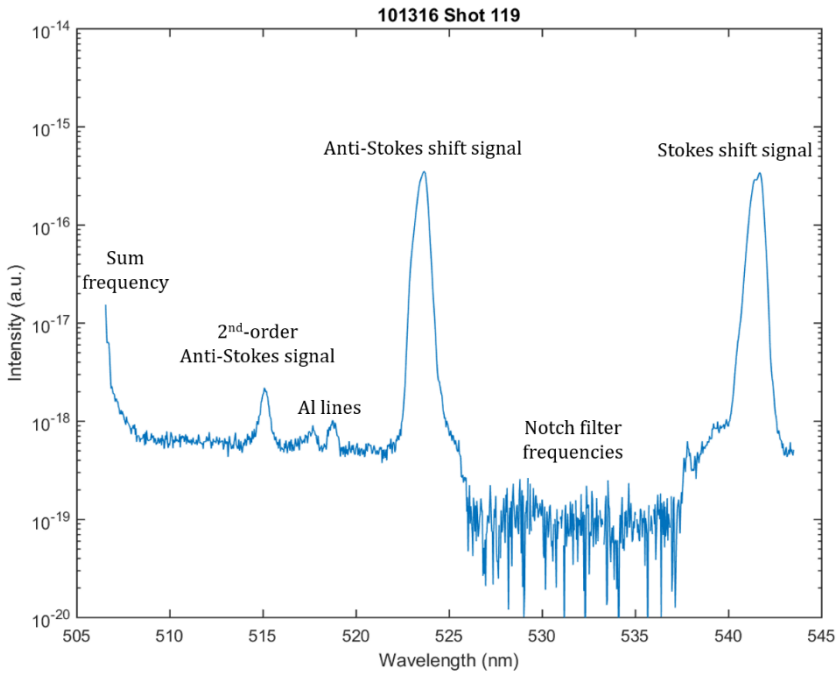

Figure 6.2:A diagram of the features in the spectral region observed by doubled-YAG CTS probes

A sample spectrum, taken at 1.77 bar backing pressure with pump energy of 1.86 J, in this range is shown on a logarithmic scale in Figure 6.1. The pixels with suppressed

signal indicate the spectral range (527 nm to 537 nm) of the notch filter, hiding the primary probe pulse. A plasma emission background is present at all wavelengths in this region, raising the noise floor. The Stokes and anti-Stokes sidebands display clean, unmodulated peaks near 540 and 522 nm respectively. The second-order anti-Stokes shift located at 514 nm is identified by the wavelength separation from the primary pulse. The maximum pixel value is used to determine the CTS wavelength shift, while the energy in the peak is integrated after subtracting a plasma background average from each pixel (not performed on this image). Aluminum oxide lines are located at 516 and 518 nm. They appear when the pump energy strikes the gas jet nozzle. To avoid confusion with anti-Stokes orders, the majority of the probe shots focused on the spectral region containing the notch filter and multiple Stokes order. At the left edge of the image, half of a peak at the pump-probe sum frequency is observed at 506.5 nm. A corresponding difference signal is observed near 560 nm (not shown in Fig. 6.1). Both signals increased in strength as the temporal overlap between the probe pulse energy and the wakefield increased.

Typical shot diagnostics included simultaneous display of the CO_2 transverse spatial profile, raw spectrometer data, raw spectral lineout, and corrected (camera-background-subtracted) spectral lineouts to see if there were any obvious complications, such as a large background light streak across the spectrometer image, that would invalidate the spectral output. Spectral modulation of many of the features was observed in numerous shots, as discussed below.

Inspection of the parameter space involved exploring several independent variables – plasma density, pump power, time delay between pump and probe, and focal plane of the pump – to determine how they affected the observed probe signal.

Chapter 6.2 Dependence of Probe Sidebands on Gas Backing Pressure and Density

Nearly all of the probe shots in regions satisfying the conditions for self-modulated laser wakefields generated at least one order of CTS sidebands. To our knowledge, these are the first self-modulated laser wake measurements in a gaseous plasma using a CO_2 laser to drive the plasma oscillations.

After initial configuration of the experimental setup, we confirmed the expected relationship between the gas density and the probe sideband wavelength shift discussed in Section 4.1. The shots recorded to test this relationship were performed with the gas jet held at a fixed height while the backing pressure was varied. All calculated densities are derived from the observed wavelength shifts, which was measured to the nearest 0.1 nm. Shifts were measured by taking the difference between the wavelength value of the peaks of the Stokes/anti-Stokes sideband signal and the primary probe signal.

A wavelength-shift average was taken over all shots at a particular backing pressure setting to explore the functional relationship. Both Stokes and anti-Stokes curves were measured in Figure 6.3. Fig. 6.3 show the expected functional relationship, $\Delta\lambda \propto \sqrt{n_e}$. Depending on the location of the pump pulse in the gas jet, the coefficients of the functional relationship changed due to higher local pressure, but the functional form remains.

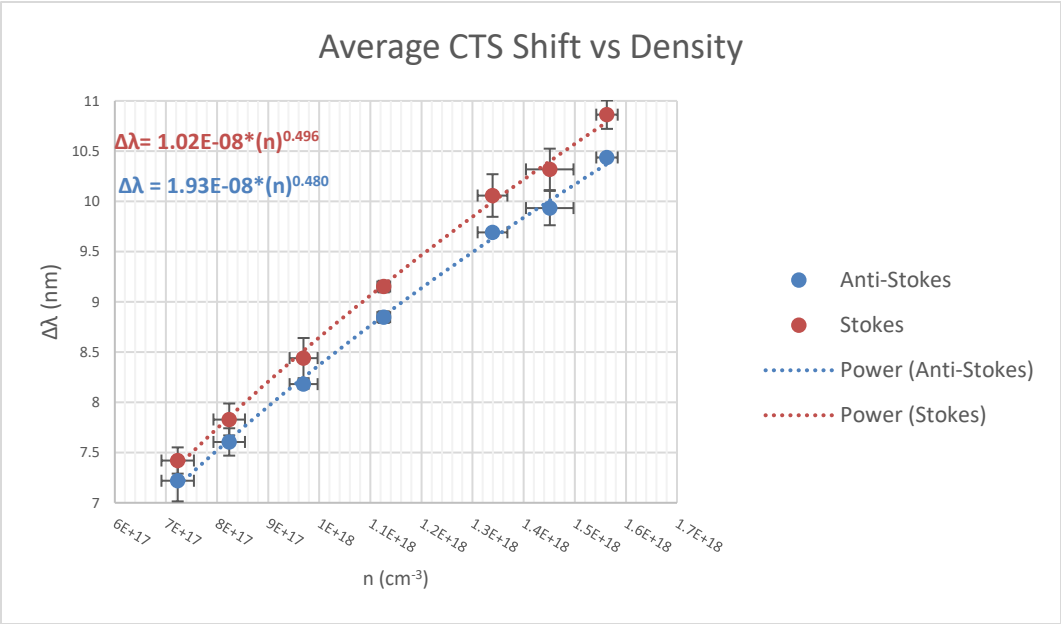

Figure 6.3: Average Stokes and anti-Stokes measure wavelength shift vs density

Chapter 6.3 Dependence of Probe Sidebands on Pump-Probe Time-Delay

The dependence of the CTS probe amplitude on the temporal delay Δt between the pump and probe was explored. Both probe and pump are approximately 4 ps long. The time delay was moved in steps of 3.3 ps on the pump delay line. The maximum pixel strength of each Stokes sideband was measured, then several shots were averaged for each time delay and their standard deviations calculated. The resulting diagram in Figure 6.4 details the observed behavior as the pump delay was scanned at 1e18 cm^{-3} and 0.5 to 3 J.

One important detail is what this time delay value means. The time delay was found roughly using the silicon wafer method described in Section 5.1. However, the absolute temporal alignment between the probe and pump is difficult to measure for such short pulses. After scanning the time delay settings, the location of peak CTS signal was set as Δt = 0 ps. Peak signal does not occur when pump and probe overlapped perfectly, but

rather when the peak energy of the probe overlaps with the wakefield peak (see Eq. 4.6). Simulations indicate that the wake is generated in the front half of the laser, so the probe starts to trail the pump slightly after $\Delta t = 0$ ps.

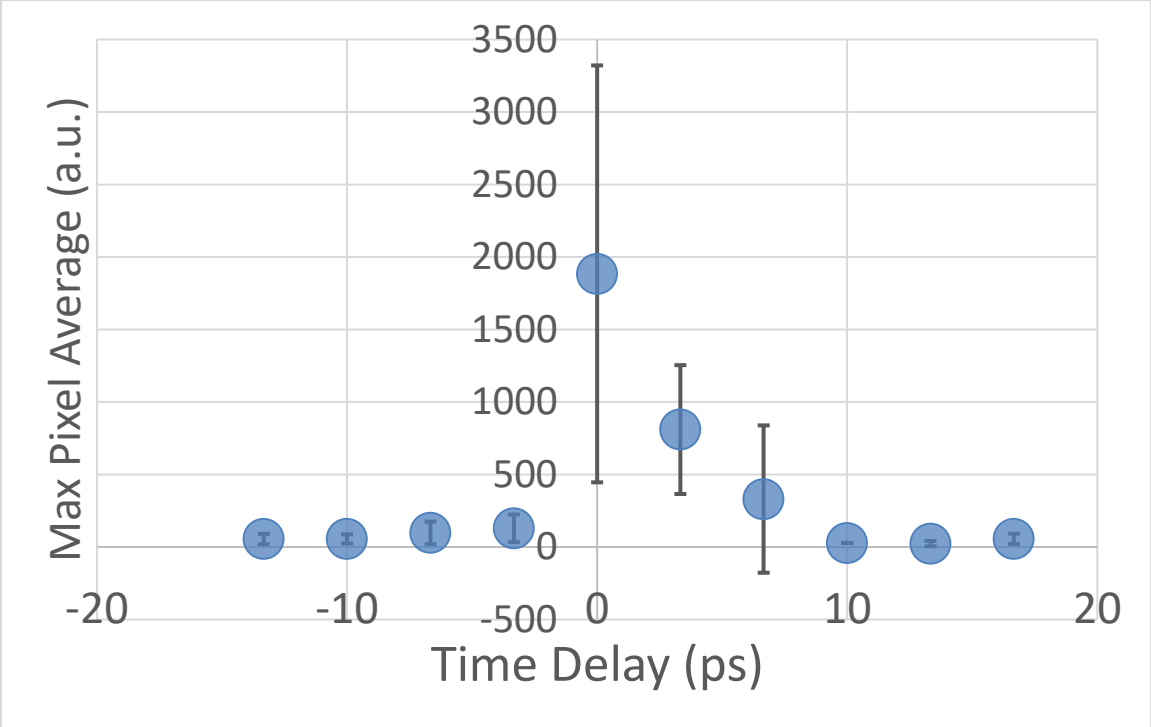

Figure 6.4: Averages of max Stokes sideband pixel signal vs time delay between pump and probe

The following description moves from the left to the right of Figure 6.4. When the probe leads the pump by more than the duration of both pulses ($\Delta t \leq$ -10 ps), there is no sideband signal since the probe does not observe a wakefield. As the time delay is further reduced (-6.7 ps $\leq \Delta t \leq$ 3.3 ps), the trailing edge of the probe begins to overlap with the front edge of the pump. In both of these regions, the standard deviations of the observed values are small.

The sideband strength rapidly increases as the temporal delay decreases to 0 ps. The rise time of the plasma wakefield is smaller in duration than the 4-ps duration of the pump pulse. This is expected, considering that the amplitude of the wake can only grow while the pump is providing it with energy. The shot-to-shot variation in CTS signal

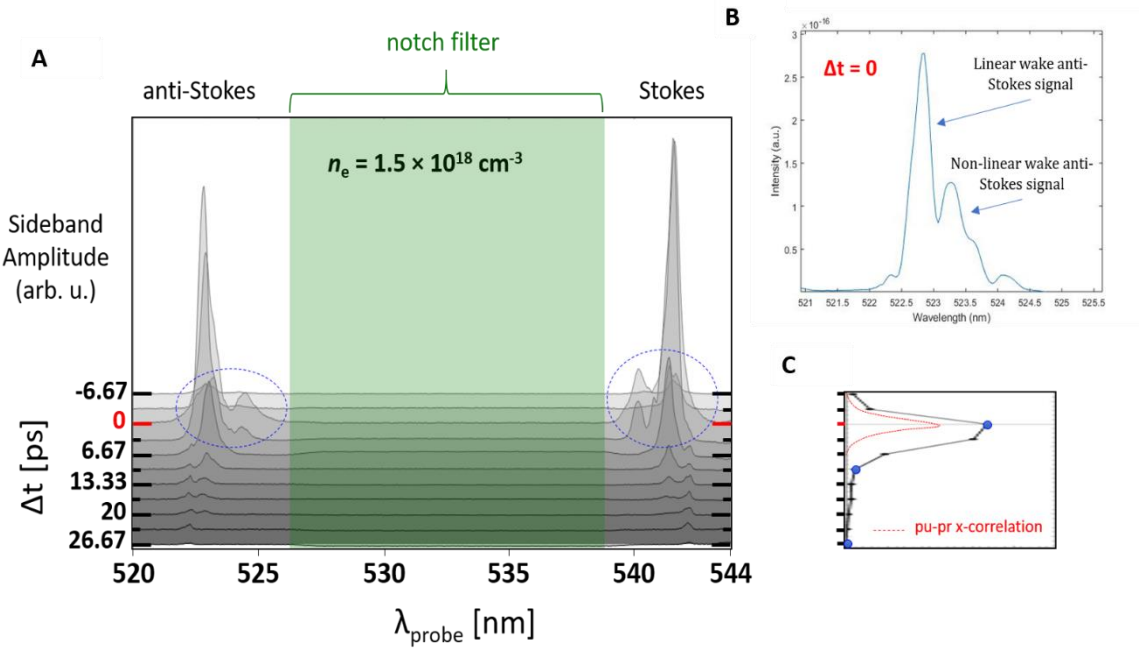

Figure 6.5: a) Waterfall plot demonstrating the change in sideband signal strength as a function of time delay. b) A zoom on a linear and nonlinear anti-Stokes signal at maximum signal time delay. c) A diagram showing the temporal profile of the probe (red) relative to the temporal profile maximum signal amplitude (black).

amplitude in this region is quite large due to the sensitivity of this highly nonlinear process on pump energy, probe energy, and density.

Transitioning past the peak signal ($\Delta t > 0$ ps), the observed sideband signal decreases quickly as the overlap between the wake and probe energy begins to lower. Shot-to-shot variations also become smaller. The measurements indicate a decay time for the

wake of 10 ps or greater. In simulations presented in Section 6.5 (Figure 6.20), ion cavitation is observed in the region several ps behind the pump pulse. This ion movement is consistent with the significant initial drop in the CTS probe signal.

Figure 6.5a shows a separate measurement of the probe spectrum as function of delay in a waterfall plot, taken at 1.5e18 cm^{-3}. The temporal overlap was determined using the same procedure detailed above with the pump energies between 0.5 and 2 J. The probe signal is negligible when the probe leads the pump significantly (-infinity < $\Delta t \leq$ ~4 ps), followed by a sharp increase in signal when the bulk of the probe energy overlaps the wakefield. Sideband signals were also observed out to 20 ps as well, providing evidence for long-lived wakes. These wakes oscillate on the periphery of the ion cavitation region, where a restoring force still acts on the electrons.

The circles superimposed on Figure 6.5a and expanded in Figure 6.5b highlight another important feature in these measurements: spectral splitting of the Stokes and anti-Stokes sidebands near $\Delta t = 0$ ps. This nonlinear shift, which is calculated in section 4.3, follows the expected wavelength formula within five percent. A detailed discussion of such signals is held in Section 6.4.2.

Chapter 6.4 Dependence of Probe Sidebands on Pump Power

The relationship between the pump power and the CTS amplitude at constant pressure falls into three regions with distinct effects on the CTS spectral sidebands. The regions are separated by the power of the pump laser relative to the critical power:

I) $P < P_{cr}$

II) $P \geq P_{cr}$

III) $P >> P_{cr}$

The first two regions have a clear dividing line, while the third has a gradual onset. It is worth reminder the reader at this point in the discussion that P_{cr} is a measurement of the power needed at focus so that self-focusing exactly equals divergence. P_{cr} also scales as $n_e^{-\frac{1}{2}}$, meaning that higher-density regions have a lower critical power.

The first region occurs when the pump power is less than the critical power. The tunnel ionization intensity for hydrogen is approximately 10^{14} W/cm^2. A pulse with even 0.5 J of energy with the experimental CO_2 focusing geometry reaches intensities of 10^{16} W/cm^2 at focus. This focusing geometry also produces a Rayleigh range of 120 μm. Without self-focusing, the laser intensity will drop by as much as two orders of magnitude over the length of the gas jet, preventing wakefield formation and even ionization inside the gas jet for low-energy pulses.

In region I, small-amplitude wakefields are generated by the pump laser. The corresponding CTS sideband amplitudes are weak to non-existent. P/P_{cr} values as low as 0.2 were observed to have CTS sidebands, but not every shot had a visible CTS signal.

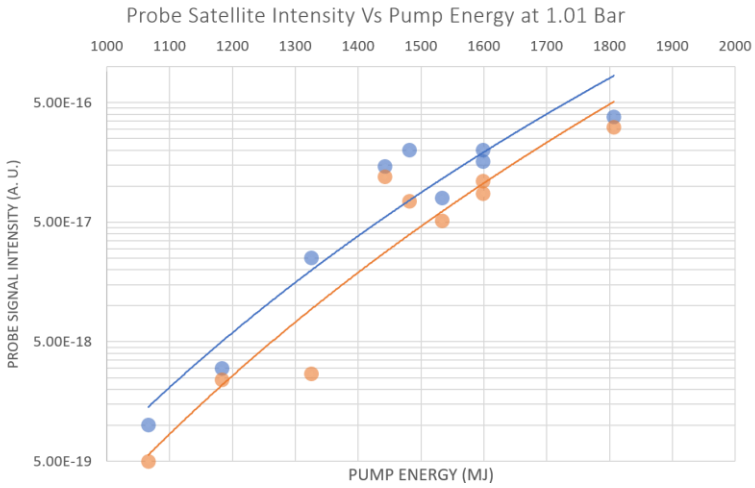

Figure 6.6: Intensity of the Stokes and Anti-Stokes signals as a function of pump energy at fixed pressure setting of 1.01 bar and fixed time delay $\Delta t = 0$ ps.

The second region is reached once the pump energy rises above the critical power of the plasma. The strength of the probe sideband signal rapidly increases as the pump power passes the critical power before reaching an upper limit. Figure 6.6 shows this behavior in both Stokes and anti-Stokes signals at a constant pressure of 1.01 atm. The pump pulse duration did not change appreciably between shots, so pump energy and pump intensity are used interchangeably. A larger pump energy translates into a larger gradient of the laser parameter a_0, which drives a stronger wakefield. Stronger wakefields have higher scattering efficiencies of probe light (Eq. 4.6), leading to an increase in the sideband signal strength measured on the spectrometer. Additionally, this region is where the nonlinear sidebands are observed for the first time. Such signals are not always present.

In the third region, the sidebands spectrally broaden before eventually the wake becomes chaotic and we observe that the coherent probe signal weakens. This region has a less distinct onset compared to the transition between the first and second. Signal strength generally increases with pump intensity. However, at some large intensity, the plasma wake will grow too quickly and break up before collective Thomson scattering sidebands are

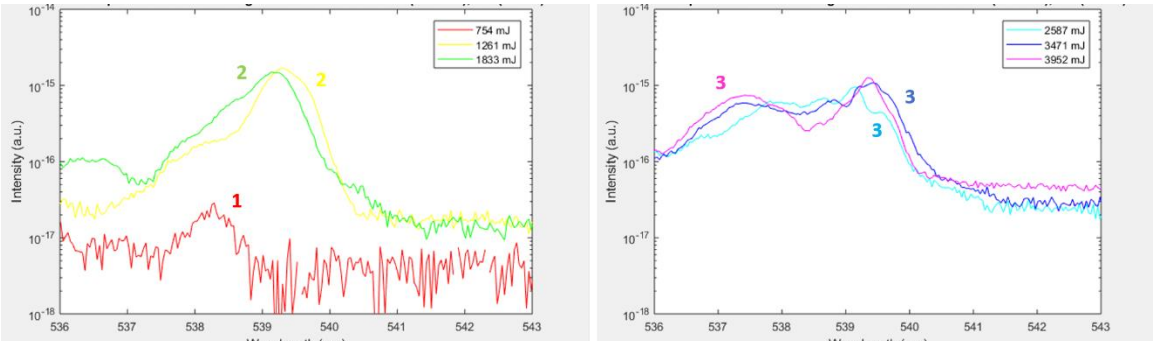

Figure 6.7: (Left) Spectral lineouts of CTS probe shots in Regions I and II. The red line ($P < P_{cr}$) was produced at the same pressure setting. The significant increase in CTS signal strength is evident in the transition from red to yellow. (Right) Several shots in Region III. Note the spectral broadening common in lineouts at high powers.

generated appreciably. Note the similarity between this description and the sideband behavior with increasing density detailed in Section 2.2.1.

Figure 6.7 shows multiple Stokes shifts at increasing pump powers and a constant pressure setting of 0.23 bar. Fig. 6.7a displays a sharp increase in sideband amplitude as pump power transitions from region I (red line, $P/P_{cr} = 0.85$) to region II (yellow and green lines, $P/P_{cr} = 1.31$ and 1.86). The green line has a nonlinear shift due to the relativistic intensity ($a_0 = 1.7$) of the laser beam which is peaked at 356.7 nm, within 0.1 nm of its predicted wavelength.

Fig. 6.7b has only shots in region III. Spectral broadening has increased the signal in lower wavelengths next to the peak of the linear Stokes shift in the cyan line ($P/P_{cr} = 2.6$) and blue line ($P/P_{cr} = 3.7$). The nonlinear shift in the magneta line ($E = 3.95$ J, $P/P_{cr} = 4.23$, $a_0 = 2.5$) is lower than the predicted shift based on the pump power (see discussion in

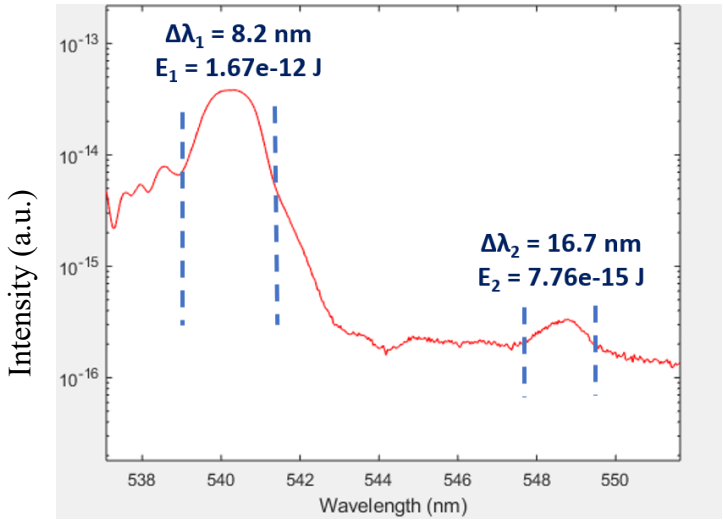

Figure 6.8: Spectral lineout of a CTS shot demonstrating the integration limits of 1st- and 2nd-order Stokes light for wakefield amplitude estimates. The integration time of the camera far exceeds the duration of the pulse, so the energy measured is proportional to power.

Section 6.3.2) and also displays significant spectral broadening. At such a low density ($6.7*10^{17}$ cm^{-3}) , the subsequent decrease of the CTS sidebands which is observed in simulations and at higher densities is not seen up to 4 J.

Chapter 6.4.1 Estimations of Wakefield Amplitudes

The wakefield amplitude estimation technique discussed in Chapter 4 was applied to the spectrometer images. Two neighboring orders of Stokes or anti-Stokes CTS sidebands were observed in many shots. In accordance with Eq. 4.14, the square root of the ratio of the two sideband powers was taken to estimate the wakefield amplitude. To prevent overestimating the sideband powers, the background plasma continuum power was

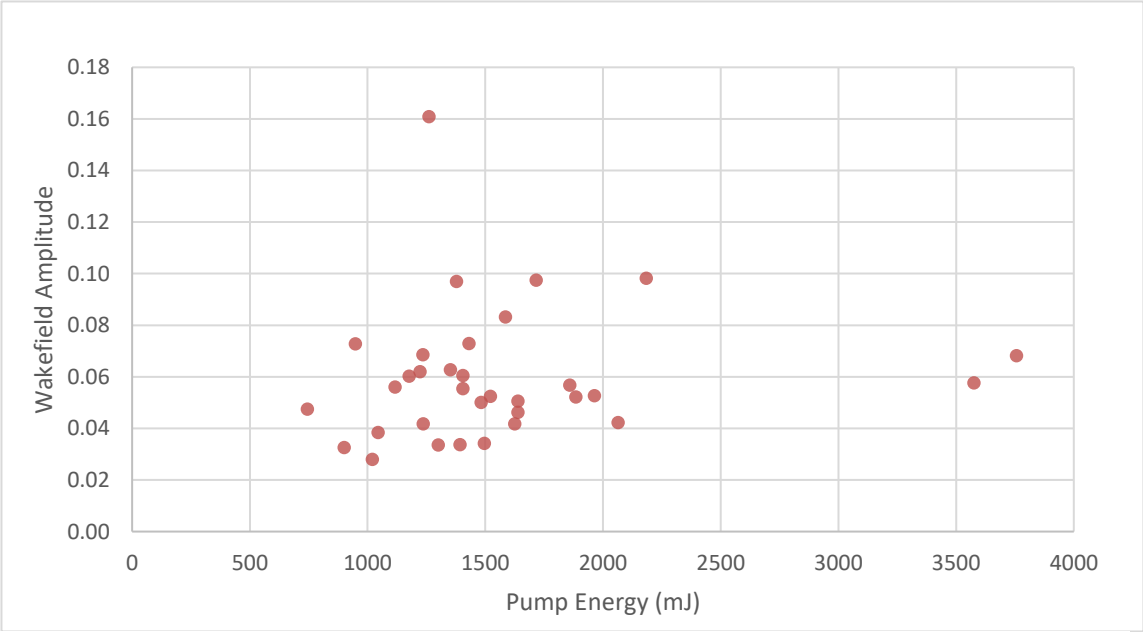

Figure 6.9: Wakefield amplitudes calculated from all shots containing more than one order of Stokes/anti-Stokes sidebands

averaged and subtracted from each pixel in the lineout. Data were taken at the time delay corresponding to peak probe signal amplitude ($\Delta t = 0$ ps).

Figure 6.8 displays a typical wakefield shot. The first- and second-order Stokes shifts are displayed after the plasma background average was subtracted from all pixels. The vertical lines indicate the limits of the energy summation. Second-order Stokes sidebands are emitted as soon as first-order Stokes sidebands are generated, so the ratio of energy is used for power. The square root of the two values yields a calculated wakefield amplitude of 0.07.

The majority of the shots are clustered in a corner of the parameter space. All but one of the wakefield shots had densities between 6.6e17 and 1.2e18 cm^{-3}, with pump energies between 700 and 3,700 mJ (corresponding to 0.18 to 0.93 TW). The other shot had a density of 1.9e18 cm^{-3} with a pump energy of 1.2 J (0.3 TW). This configuration produced the largest measured amplitude. The calculated wakefield amplitudes from all shots with two orders of sidebands are plotted in Figure 6.9.

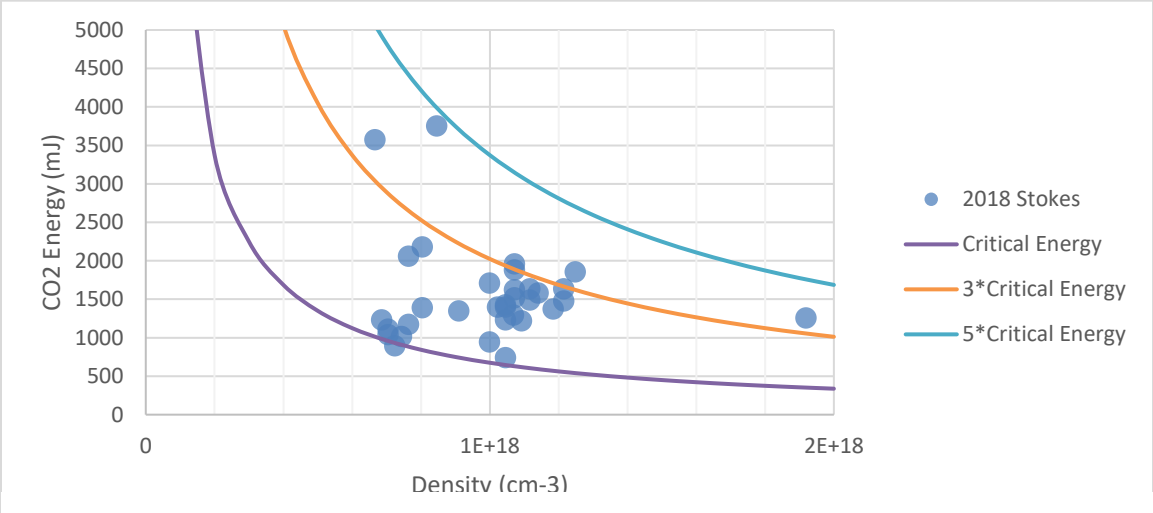

Figure 6.10: Shots with two orders of CTS signals in pump energy/density parameter space. Contours of odd integers of critical energy are drawn to demonstrate the ranges

The same measurements shown in Fig. 6.9 are plotted on a graph of pump energy versus density (Figure 6.10). Contours corresponding to integer multiples of critical power are drawn on this figure. No shots with multiple orders of Stokes or anti-Stokes sidebands were observed below the $1*P_{cr}$ line, highlighting how important self-focusing is for large-amplitude wakefield generation. A contour indicating $5*P_{cr}$ was included to bound the region in P/P_{cr} space, but does not demonstrated any obvious significance

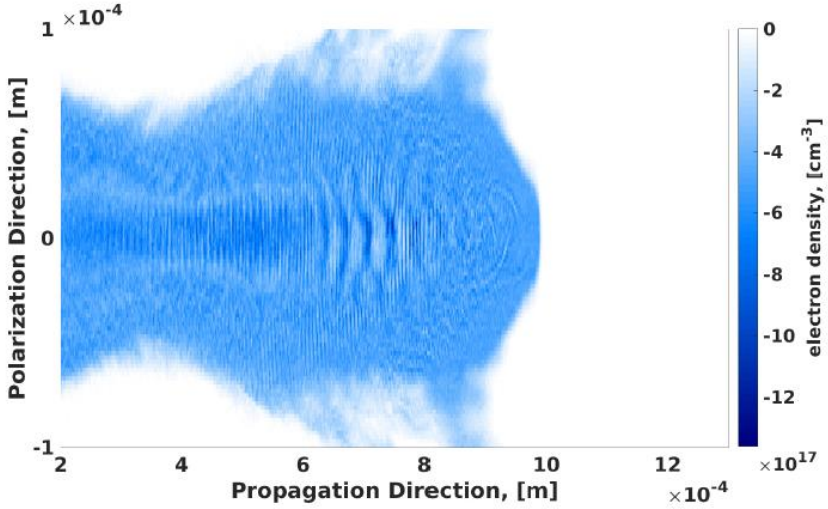

Figure 6.11: 3D SPACE simulations of wakefields generated in $5*10^{17}$ cm^{-3} using a CO_2 driver pulse of 1 J and 2 ps. The density at the peak is close to 10^{18} cm^{-3}, corresponding to a wakefield amplitude of 2.

As discussed in Section 4.3, the calculated wakefield amplitudes are underestimates due to the probe's large spatial and temporal extents. Simulations performed by collaborators at Brookhaven National Laboratory (1 J, 2 ps, $5*10^{17}$ cm^{-3}) under similar conditions to the experiment produced wakefield amplitudes at or above 1 (Figure 6.11) [124]. Previous experiments by LeBlanc used Ti:Sapphire probes, which are ten times shorter than the 4-ps doubled-YAG probe pulse used in this experiment. The longer probes used in this experiment averaged over a larger volume in space. This volume encompasses

regions of small-amplitude linear wakes which only produce 1st-order sidebands at appreciable energies, leading to artificially lowered wakefield amplitudes by oversampling the 1st-order signal. Decreasing the temporal and spatial dimensions of the probe would increase the observed wakefield amplitude by reducing the observed volume and thus the extra 1st-order sideband power, but would require more precise overlap with the large-amplitude wake. Alternative probing methods such as frequency-domain streak camera (FDSC) [125] and electron diffraction probes [126] would provide more detailed and localized information about the wakefield structure, avoiding the distortions introduced by averaging over the entire propagation length in CTS probes.

To illustrate the underestimation of the wakefield amplitudes using the CTS sidebands method, we refer to simulations performed by collaborators at Stony Brook University. A CO_2 driving pulse with 9.2-μm wavelength, 4 J, and 2 ps was propagated through an un-ionized hydrogen gas medium [127] (The lower wavelength is in anticipation of upcoming design changes to the BNL CO_2 laser). The simulation assumed a uniform background plasma density of $7.5*10^{17}$ cm^{-3}. Figure 6.12a shows the plasma density distribution snapshot during propagation while 6.12b shows the spectral intensity of the entire pump pulse after exiting the plasma. Note that the pulse duration was shortened due to computational constraints.

The peak wakefield density in 6.12a is approximately $3.5*10^{18}$ cm^{-3}, corresponding to an amplitude of $\frac{\Delta n}{n_0} = \alpha = 4.7$. If we apply the same wakefield amplitude estimation calculation, we predict a wakefield amplitude of 0.33, an order of magnitude less than the simulated amplitude. It should also be noted that the CTS wakefield amplitude measurement method has a practical maximum of 1 since 1st-order sidebands must be generated before 2nd-order sidebands can occur, yet the observed amplitude of 4.7 is much

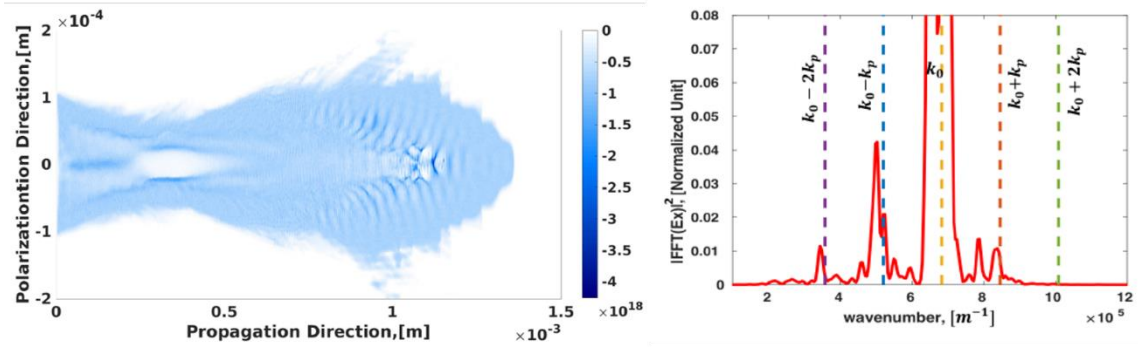

Figure 6.12: (Left) SPACE simulation of 2-ps, 1-J CO_2 pulse in a 1.5-mm region of hydrogen gas ($n_e \sim 7.5*10^{17}$ cm^{-3})
(Right) Spectral intensity of the CO_2 pump pulse after exiting the plasma, exhibiting two orders of Stokes signals

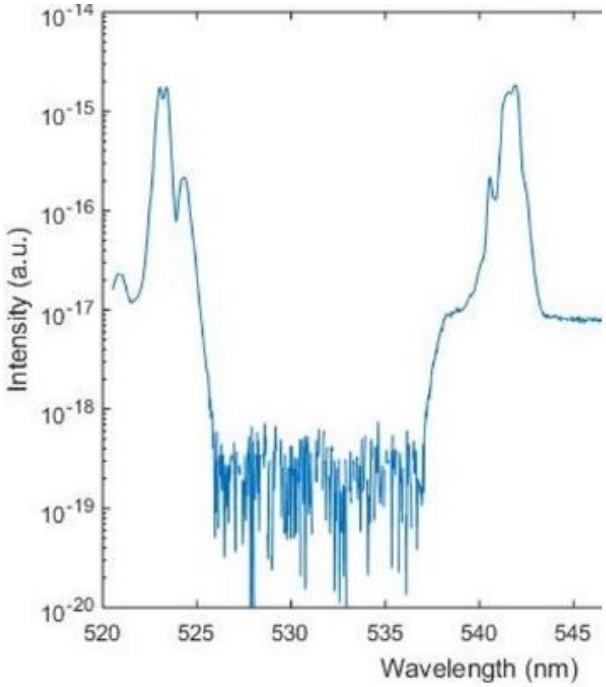

Figure 6.13: Probe spectrum displaying both Stokes and anti-Stokes linear and nonlinear shifts (the nonlinear shifts are closer to the notch filter depression).
Nonlinear shifts are expected to be closer to the fundamental frequency than the linear shifts due to the relativistic corrections to the electron mass.

higher. It is clear that this method cannot accurately reproduce the actual wakefield amplitudes when the wakefield is evolving and strongly nonlinear.

Chapter 6.4.2 Spectrally Distorted Probe Sidebands

When the pump energy is high enough to generate nonlinear wakefields ($P > P_{cr}$), the nonlinear shift described in Section 4.4 is often noticeable in the probe spectrum. Numerous shots displayed spectrally double-peaked signals for both Stokes and anti-Stokes sidebands (Figure 6.13). For a fixed pulse duration and diameter, the decrease in the frequency shift as a function of energy can be estimated as demonstrated in Section 4.4. For example, given the 4-ps duration and 20-um vacuum beam waist of the pump pulse, the threshold energy to cause a 10%-shorter nonlinear Stokes/anti-Stokes shift compared to the linear Stokes/anti-Stokes shift is 600 mJ.

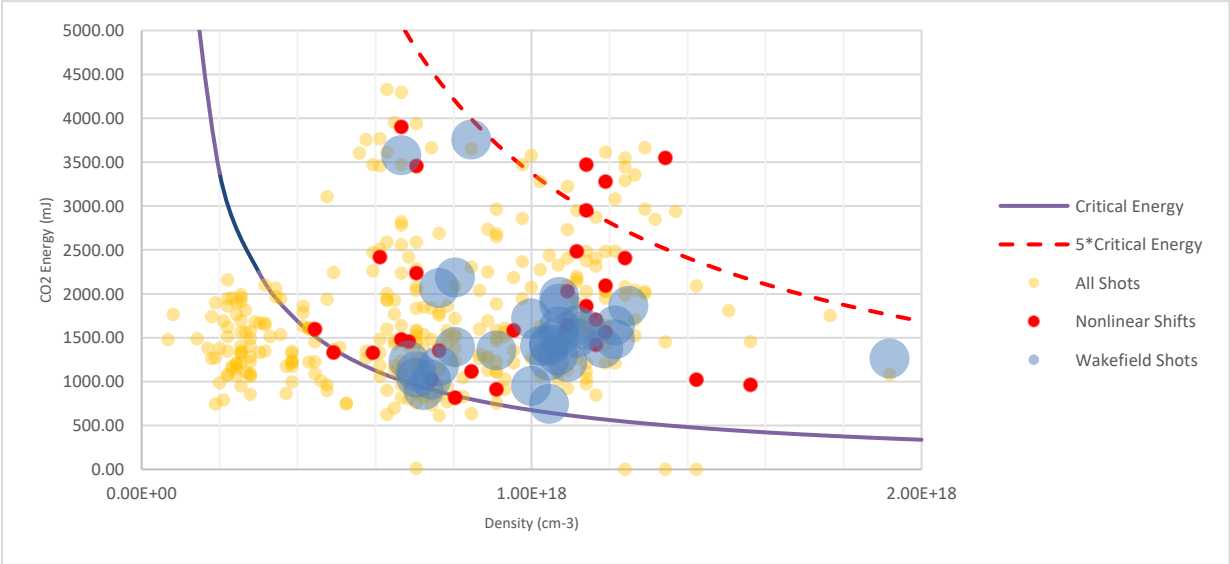

Figure 6.14: Combined wakefield estimates and nonlinear shots against a background of all shots with Stokes shifts observed

These shifts did not occur in every shot which displayed linear CTS signals. Of the 320 shots which demonstrated a Stokes shift in one experimental run, only 30 had an observable nonlinear shift. All shots with observed linear CTS shifts had vacuum-focus a_0 values between 1 and 2.65. The shots with nonlinear shifts had vacuum-focus a_0 values between 1.15 and 2.5. Nearly all the shots were taken with the focal plane before the gas jet or on the entry ramp of the gas jet. Additionally, half of the 30 shots had the pump-probe delay such that the probe was leading the pump by as much as 6.7 ps.

Figure 6.14 contains data which had linear and nonlinear shifts. The pump energy and plasma density of all the shots in which a linear CTS shift was observed are shown as yellow circles. All spectrally doubled-peaked (aka nonlinear) shots (red circles) and all shots where two CTS sidebands were used to estimate the wakefield amplitude (blue circles) are presented.

Not all CTS shots have nonlinear shifts, despite having sufficient power. This failure to observe a nonlinear shift in the probe could be a consequence of the highly nonlinear propagation and wakefield generation dynamics. The laser pulse profile is imperfect. Despite nominally having sufficient energy to reach relativistic intensity in vacuum, the presence of a plasma may disrupt the focusing geometry, preventing the pulse from achieving this intensity in-situ. Alternatively, if the nonlinear wake is relatively small, then the nonlinear shifted light may be hidden due to the plasma continuum background or only a small volume of the probe overlapping the nonlinear wake.

As with multi-order CTS signal generation, no nonlinear shift is observed below the critical power line. This once again highlights the importance of self-focusing in producing strong wakefields which scatter probe light efficiency. The vertical column of nonlinear sidebands with densities between 1 and $1.4*10^{18}$ cm^{-3} had the probe leading the

pump by the largest amount, indicating nonlinear wakefield formation in the front portion of the pump for high powers (0.4 to 0.9 TW).

The predicted nonlinear shift was compared to the measured value to see how well the prediction performed. Three shots drastically "overperformed" prediction by having a smaller shift (i.e., a higher observed a_0) than predicted from the pump power by least 1 nm. Other shots "underperformed" prediction by having larger wavelength shifts than expected.

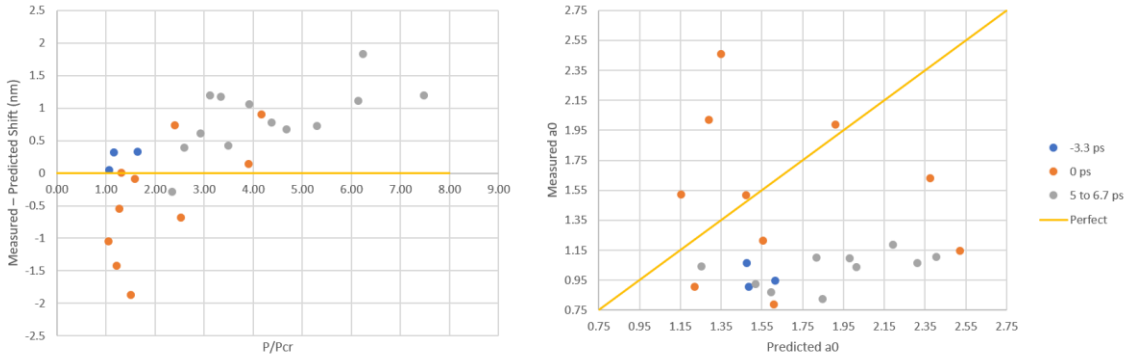

Figure 6.15: (Left) Nnonlinear CTS shifts measured – predicted shifts in nm versus P/P_{cr}. (Right) Measured a_0 (from the observed shift) vs predicted a_0 (from the pump power)

Figure 6.15a shows the difference between the measured and predicted nonlinear shifts at different pump-probe time delays as function of P/P_{cr}. The probes which trail the pump (blue circles; Δt = 3.3 ps, 0.32 bar) were all taken at $1 \leq P/P_{cr} \leq 2$ and are quite close to the predicted value. Probes which led the pump pulses (grey circles; Δt = -6.7 to -5 ps, 0.62 bar) were taken at slightly higher pressure. Most of these probes "underperformed", leading to weaker shifts. In these shots, the probe is only overlapping a small portion of the front of the wake. In such a region, the pump intensity seen by the probe is lower than the estimate, which uses the pump's peak intensity. This is likely the reason for the reduction in observed nonlinear shift.

The most interesting probes have the optimal time delay (orange circles; $\Delta t = 0$ ps), have low critical power ratios, and display larger shifts than predicted (i.e., the "overperforming" region). These three shots were taken with a moderate pressure setting (0.24 bar) and correspond to a measured plasma density of 7e17 cm^{-3}. All three shots had pump energies close to 1 J.

To understand how this may occur, consider the dynamics of a low-energy, moderate-density, temporally-long shot with $\Delta t = 0$ ps. As the pulse propagates through the gas, it ionizes the medium with ease but does not drive wakefields too dramatically. Instead, self-focusing is allowed to continue for a significant distance, constantly increasing the pump intensity by allowing transverse (due to self-focusing of the radial pump profile) and temporal (due to the refractive index delay of the peak portion of the pump) energy to focus along the pump axis. Gradually, the pump ponderomotive energy gradient can grow past the initial a_0 estimate (which was based on the peak intensity of the initial pump beam), leading to larger nonlinear mass accumulation by the plasma electrons.

This result points to a potentially useful parameter space region. Lower energy (around 1 J) pump pulses are easier to achieve, opening the door for more investigators to explore the space. Additionally, the estimated electron energy for self-modulated wakefield scales as $n_e^{-\frac{1}{2}}$, meaning that lower densities should produce more energetic electrons. By looking back at Fig 6.14, moderate-density shots (around $7*10^{17}$ cm^{-3}) with energies between 1 and 1.5 J, just above the critical power, also produced a large number of wakefield amplitude measurements. All of these characteristics are suggestive of an electron acceleration region without significant modulation effects and low chance of rapid plasma breakdown. Future investigators would be wise to carefully explore this region first (0.75 to 1.5 J, 5e17 to 8e17 cm^{-3} for a 4-ps pump duration).

Chapter 6.5 Dependence of Probe Sidebands on Pump Focal Plane

The focal plane of the pump pulse was varied with respect to the longitudinal (i.e., z-axis) position of the gas jet to observe the changes in the CTS signal. The gas jet nozzle output was assumed to be roughly Gaussian.

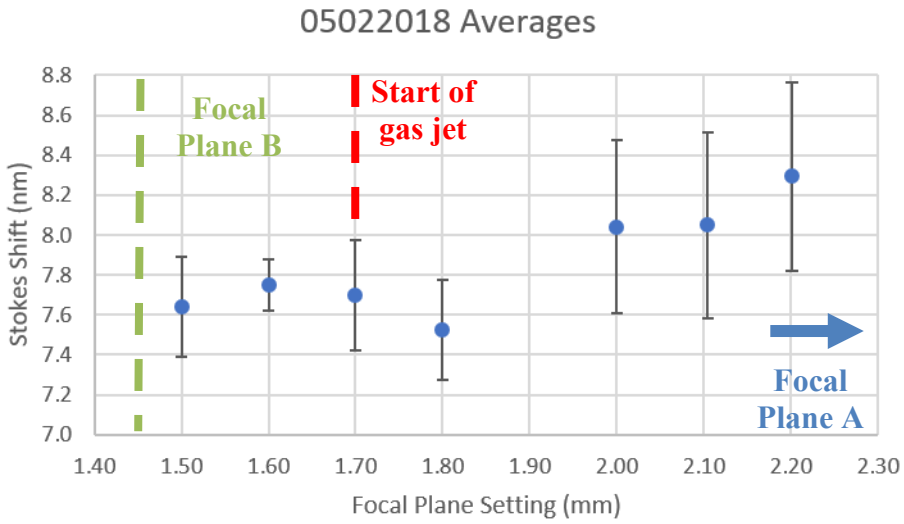

Figure 6.16: Stokes wavelength shift as the focal plane is adjusted (lower numbers mean farther into the gas jet). This is a low-pressure scan at $\Delta t = 0$ ps

A focal plane run was performed at a gas jet nozzle pressure setting of 0.27 bar. The scan was performed at the maximum probe-pump signal setting ($\Delta t = 0$ ps). Smaller numbers indicating the focal plane moving farther into the gas jet and larger numbers indicating the focal plane moving away from the gas jet. Each setting averaged 4 to 6 shots to produce the value and the standard deviations used for the error bars. The variability in the pump pulse energy was roughly constantly for all of these shots and equal to +/- 20% from shot to shot.

The focal plan scan data in Figure 6.16 has two distinct regions. Focal planes closer to the gas jet center yield smaller Stokes wavelength shifts. Focal planes farther from the gas jet yield larger Stokes shifts. Note that the setting 1.7 corresponds to the edge of the gas jet. Given the size of the error bars, it is unclear whether any perceived curvature in the

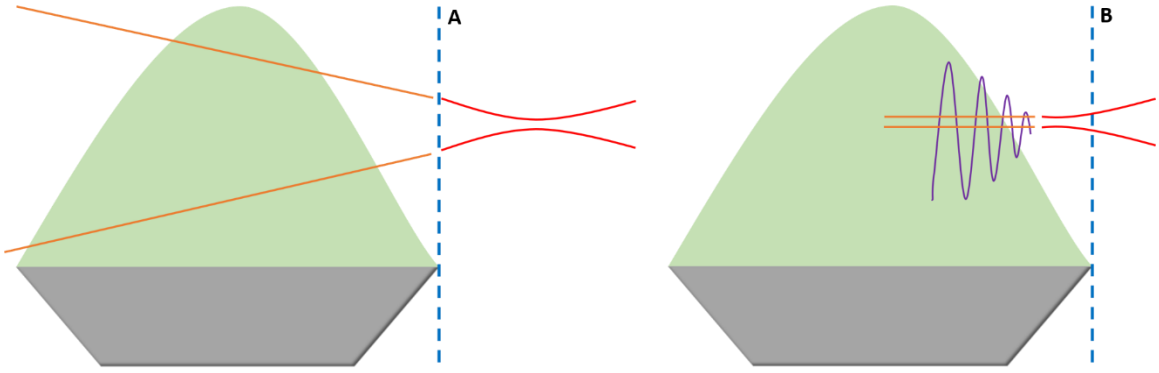

Figure 6.17: Pump dynamics for two focal plane locations, one before the gas jet (a) and one on the gas jet ramp (b). The blue dashed line indicates the start of the gas jet, and pump propagates from right to left. The left figure shows the case where the divergence is too great to be overcome by self-focusing, although it does keep the beam smaller inside the gas. The right figure shows self-focusing occurring on the slope of the gas jet, generating a wake at a lower-than-peak density.

figure is a true feature. However, the variation at farther-away focal planes (≥ 2) is nearly twice as large as the variation at closer focal planes (≤ 1.8). This implies a large drop in sensitivity to the pump energy when the focus is close to the edge and inside of the gas jet.

The behavior being observed in this figure is related to two optical considerations: a) the self-focusing due to a combination of gas density and pump power, and b) beam divergence. The gas density has an assumed Gaussian shape along the z-axis. For focal planes distant from the edge of the gas jet (Figure 6.17a), the pump beam will focus to its beam waist before entering the gas jet. A low-power pump beam or insufficiently dense

gas jet will not provide enough self-focusing to overcome the divergence, allowing the beam to continue its expansion unabated.

If the focal plane is moved forward (Figure 6.17b), then the beam diverges less before it encounters the gas density ramp. With less divergence to overcome but the same density profile, the local intensity at each time step will also be higher, meaning the self-focusing strength is larger as well. Consequently, the focusing effects produce a pulse with a pondermotive profile capable of initializing a wakefield earlier. The observed density of the CTS probe will thus drop as the focal plane moved closer to the gas jet.

Collaborators at Stony Brook University performed 2D OSIRIS simulations using a Cartesian window with moving geometry. The CO_2 pump pulse was modeled as a Gaussian with 4-ps FWHM duration, 1 J, and a_0 of 2.1 (Figure 6.18). The plasma jet was modeled using an un-ionized H_2 gas medium with mobile ions, which were found to correspond best to real data in previous simulations. The gas jet region was modeled as a 2-mm flat region with 500-um linear ramps on either side, with peak density of $7.5*10^{17}$ cm^{-3}. This region sits between 0.25 cm and 0.55 cm in the upcoming figures.

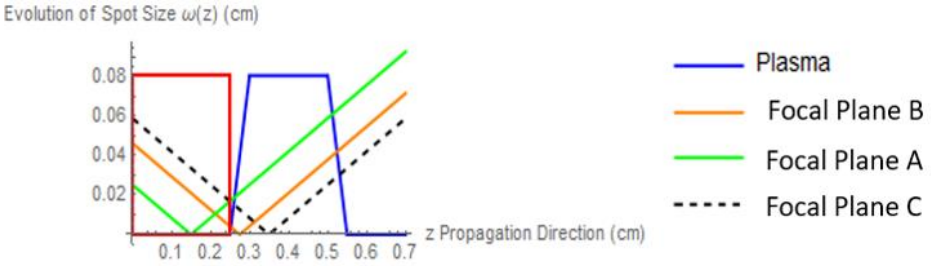

Figure 6.18: Conceptual drawing of the focal plane locations of the pump beam in 2D OSIRIS simulations. The red box is the moving Cartesian window. The plasma has linear ramps as opposed to a Gaussian shape. Note that Focal Plane C is neither discussed nor depicted in the following sections.

Two focal positions were chosen: 1 mm before the plasma starts (Focal Position A) and one in the middle of the plasma ramp (Focal Position B) (Figure 6.19). The

experimentally measured data examines the transition region between Focal Planes A and B, so only those two simulation results are shown.

For Focal Plane A, the beam focuses in vacuum before the gas jet ramp begins (1) and starts diverging before entering the gas jet (2). Upon entering the gas jet, the beam

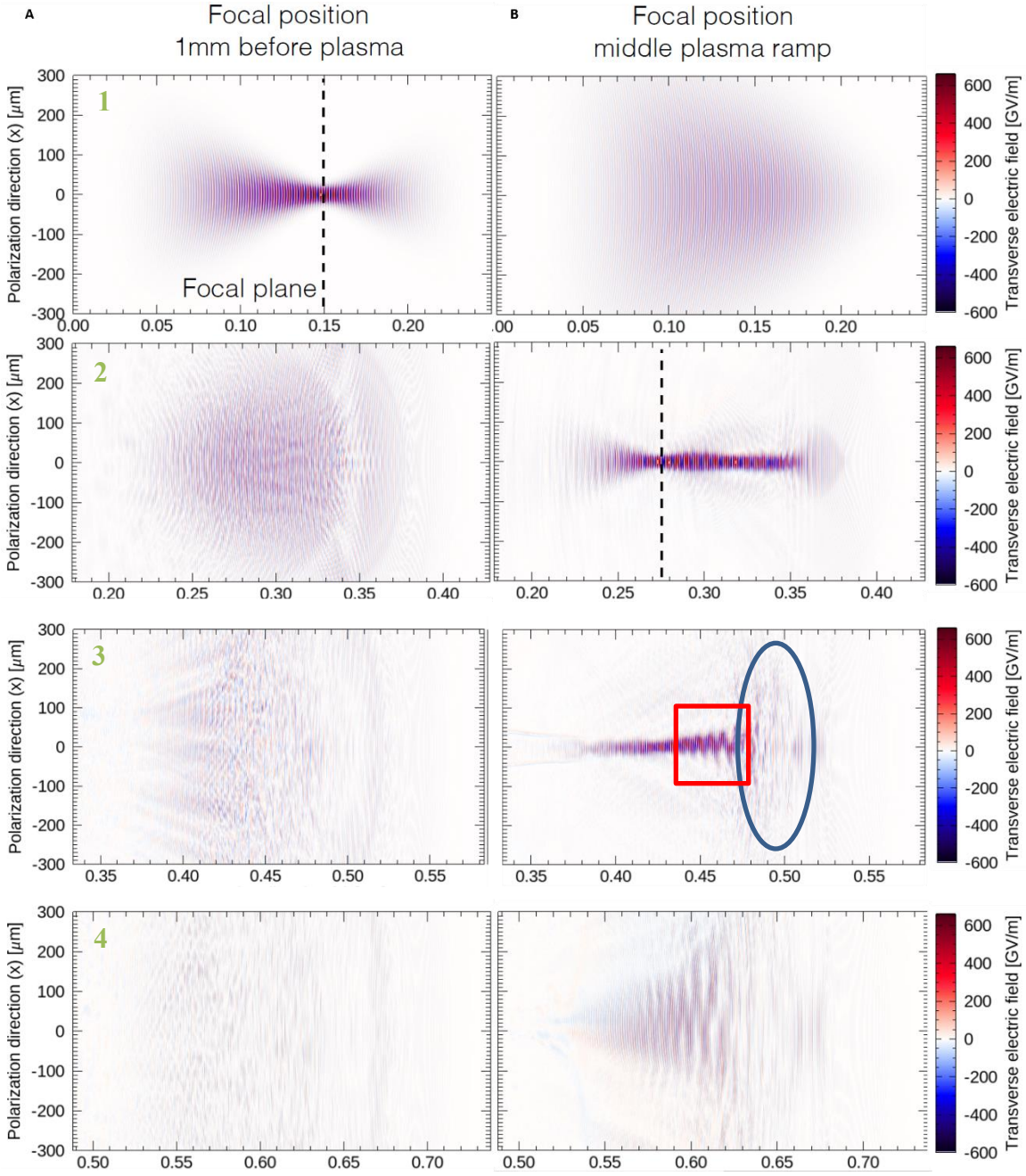

Figure 6.19: Transverse electric field evolution of pump beams with Focal Planes A and B. The blue oval highlights that diminished energy of the front and the red box highlights hosing of the midsection of the laser in panel 3.

continues to diverge (3-4) since the self-focusing is insufficient to overcome diffraction.

This is evident by the curved wave fronts in panels 6.19b and 6.19c. However, since the transverse size of the pulse in the plasma is much larger than the plasma wavelength, as it propagates, it becomes transversely unstable. This is apparent in the transverse modulation

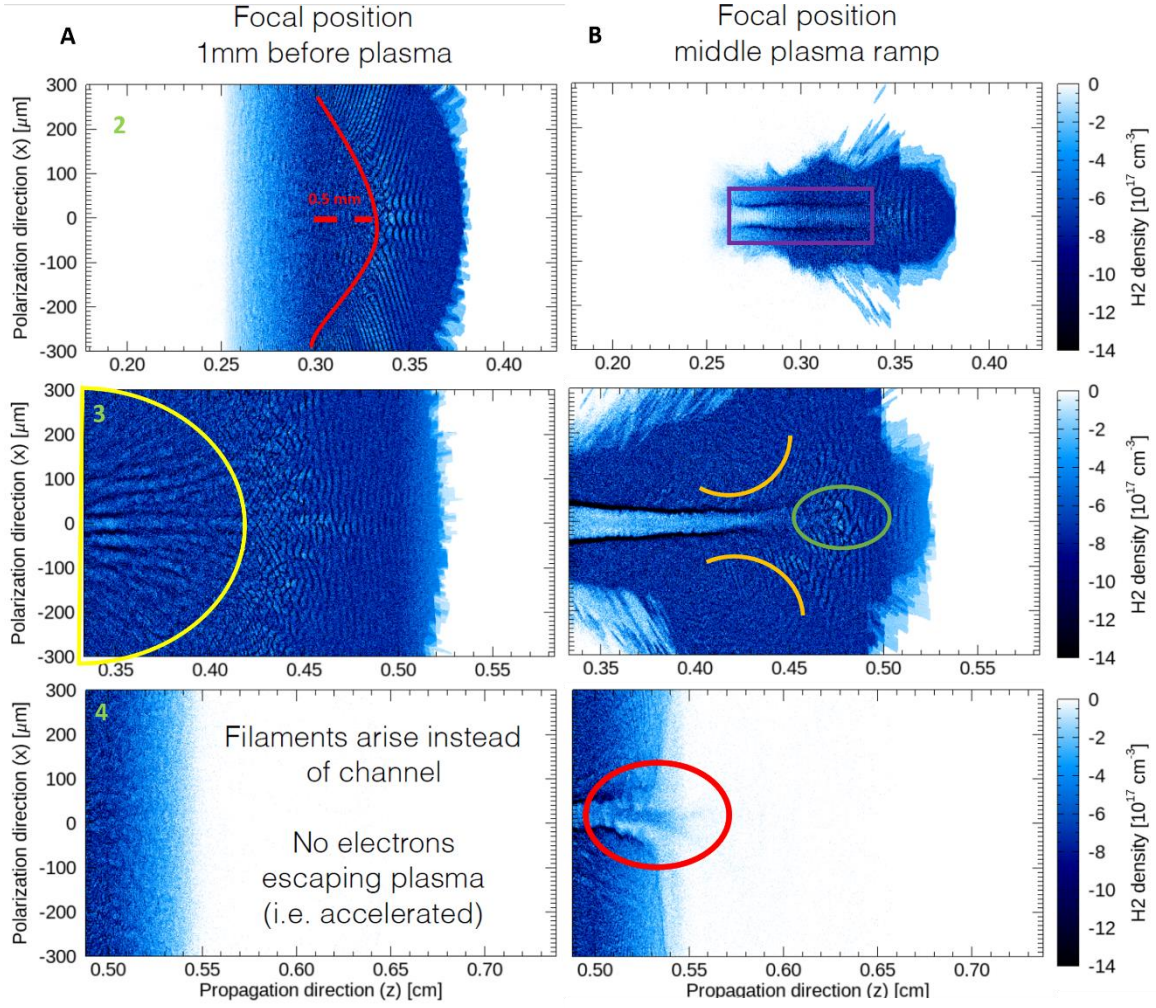

Figure 6.20: Electron density during propagation for both focal planes.

of the field in 6.19c and 6.19d.

For Focal Plane B, the beam is converging as it enters the gas jet (1). It reaches its focus in the middle of the gas jet ramp (2) and then sustains a small transverse size for at

least 2 mm due to self-focusing (2-3). After another 1.5 mm of propagation, the front portion of the pulse no longer has enough power to self-focus (blue oval in 3) while the midsection of the pulse undergoes hosing (red box in 3). The back portion of the pump pulse remains stable due to trapping in a radial plasma channel that trails the pump. The pulse then resumes diverging after the gas jet ends (4).

An inspection of the electron (Figure 6.20) densities for these simulation runs (corresponding to panels 2, 3, and 4 in Figure 6.19) is also instructive. A similar plot of ion densities shows the same behavior at smaller amplitudes. For Focal Plane A, individual wakes start to form in a semi-circular pattern with a radius of 0.5 mm from the end of the gas jet ramp (red curve in 2). The transverse size of the beam is larger than a plasma wavelength, leading to instabilities which generate wakefields. Small-amplitude wakefields are observed in the densest region of the plasma (yellow half circle in 3). These wakefields are the source of the low-energy CTS sidebands generated in a plasma when $P < P_{cr}$. The largest wake is generated in the middle of the gas jet (where the density is highest) by the transverse center of the pump pulse (where the power is highest). These wakes form then diminish in amplitude rapidly due to the divergence of the pump beam (right side of 3). No electrons are accelerated out of the plasma (4).

Comparatively, Focal Plane B shows a laser filament forming a single plasma channel all along the gas jet ramp and into the central density region, expelling both electrons and ions (purple box in 2). The first panel shows a self-modulated laser wakefield generated by the front section of the laser. Because the pump pulse is 4 ps long, significant ion motion can occur within its duration. Due to this, within a single pulse, we observe the formation of both an electron wake and an ion wake (2 and 3). The fast-moving electrons form a wake in the early portion of the laser pulse (depressions to the right of the purple box) while the slow-moving ions form a transverse wake trailing the front half of the pulse.

The reduction in a sufficiently uniform and dense plasma prevents large-amplitude wake formation in the trailing region and thus CTS sideband generation. The drop in CTS signal in Figure 6.4 as the probe begins to trail the wake ($\Delta t > 0$ ps) is likely due to the decrease in volume in which a wakefield is present.

Local density variations with a wavelength characteristic of the CO_2 laser are observed in the region of highest pump power and trailing behind it (inside the purple box in 2). The phase variation in the electric field can cause alternating regions of high and low density. These variations are likely the source of the CTS sum and difference frequencies, appearing when probe light scatters off of the variations and shifts the light by the characteristic frequency.

The panel labeled 3 in Figure 6.20 shows the wake growing highly nonlinear as evidenced by the U-shaped curvature of the plasma wave fronts near the front and at the edges of the laser pulse (orange curves highlight the locations). This is caused by the radial variation in relativistic mass associated with the transverse variation in laser intensity. The region between 4.5 and 5.5 mm displays a very chaotic and broken wake (green circle in 3). Ion wakes form in the trailing region, leading to almost complete cavitation in the radially expanding plasma channel. The panel labeled 4 in Figure 6.20 shows accelerated electrons, which are visible exiting the plasma as a columnated beam in the final panel (red circle in 4).

Differences exist between these simulations and the experimental conditions used in collecting the data displayed in Figure 6.16. The experimental gas jet has a circular nozzle opening of approximately 1 mm in diameter and a roughly Gaussian radial density distribution. The 2-mm central region in the simulations is longer and flatter than the curved peak region of a Gaussian. Additionally, Focal Planes A and B are located at positions outside the experimental data, showing what happens at the two extremes of focal

plane positioning. Note that Focal Plane A is closest in physical situation with the region on the right-hand side of the Figure 6.4 and Focal Plane B is closest in physical situation with the region on the left-hand side.

How do the simulations compare then to the experimental data? For Focal Plane A, the semi-circular pattern of small-amplitude wakes demonstrates the pulse must travel deeper into the gas jet before separate regions of the pulse can self-focus (due to a drop in P_{cr} and the flattened wave fronts not diverging as much, both of which are necessary to achieve $P \geq P_{cr}$ locally) and produce a wakefield. The deeper regions of the gas jet have higher densities, which will lead to larger CTS sideband wavelength shifts. This is similar to far-away focal plane behavior in Figure 6.4.

Conversely, Focal Plane B produced an evacuated plasma channel on the gas jet ramp, indicating the pulse's capacity to drive wakes as soon as it reaches the gas jet entrance. The wakefield starts to form earlier than for Focal Plane B, which is consistent with the lower observed CTS wavelength shifts on the left side in Figure 6.4. However, in order for the CTS sidebands to have a smaller sideband wavelength shift at Focal Plane B (i.e., observe only densities smaller than those observed with Focal Plane A), no large-amplitude wakefield can form in the densest region of the gas jet. The midsection of the pulse undergoes hosing, while the back section of the laser travels through an evacuated plasma channel. These effects prevent a large-amplitude secondary wake from being generated. The simulations show a drastic energy drop in the front of the laser pulse by the time it reaches the central density region, due to some combination of energy loss from ionization, wakefield generation, and scattering effects. We postulate that the front of the laser is sufficiently reduced by the time the pulse reaches the peak density region of the gas jet that it can no longer generate a large-amplitude wakefield and that the remaining

sections of the pulse are also unable to generate a large-amplitude wakefield due to the other mentioned effects.

Lastly, the variations of the two regions in Figure 6.4 are strikingly different. For Focal Plane A shots, the pulse must travel deeper into the gas jet before wakefields can be produced. For a gas jet with linear ramps and a long, flat peak density region, the variation would not be very large. However, a curved density profile such as a Gaussian will cause greater variation in where small-amplitude wakefields will form due to local variability in power and density. It may also produce wider CTS sidebands than shots with Focal Plane B, but there were not enough data to explore this possibility appropriately.

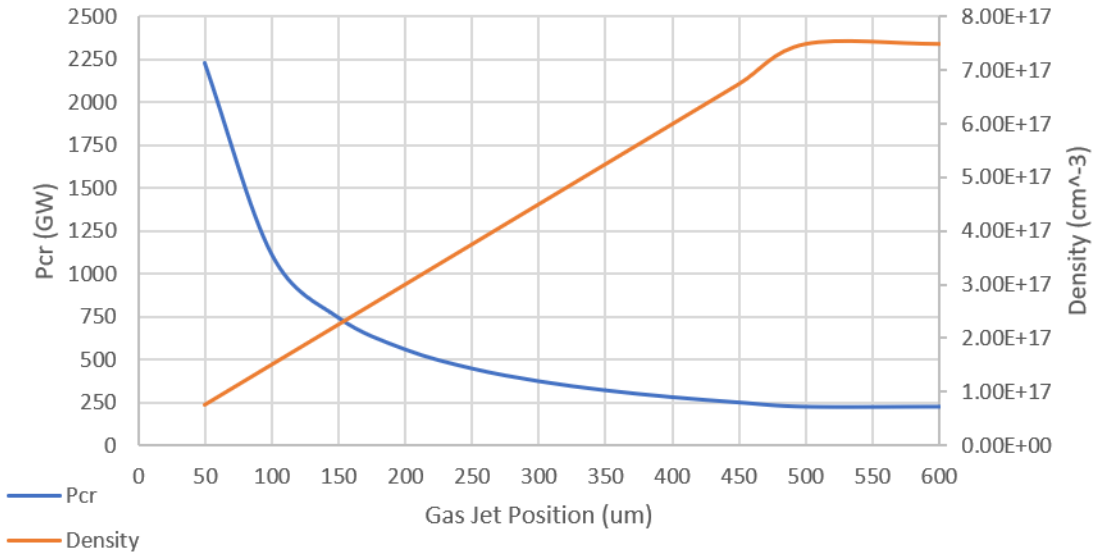

Figure 6.21: Critical power and density in the simulation gas jet. The critical power changes rapidly on the front ramp, making the location where wakefields start to form more consistent

The lower variation in shot-to-shot CTS sideband wavelength for shots with Focal Plane B is sensible for pulses focused onto a gas jet ramp. P_{cr} has the expected $n_e^{-\frac{1}{2}}$ dependence, which shows the critical power decreasing as the gas density increases. On

the entrance ramp of a gas jet, a small change in longitudinal position will correlate with a large increase in gas density. Correspondingly, the locations where P/P_{cr} reaches 1 for a range of pulse powers will be close together. In Figure 6.21, both critical power and density are shown for the first 600 μm of the simulation gas jet environment. Within the first 250 μm, the critical power decreases nearly a factor of ten from 2,250 GW to 350 GW. This wide range of powers all start self-focusing in roughly the same position. Wakefields form readily when $P/P_{cr} \geq 1$, so a wide range of pump powers will generate wakefields at roughly the same longitudinal position in the gas jet. Thus the CTS probe will observe less varied density and CTS wavelength shift.

Chapter 6.6 Discussion of Results and Potential Electron Acceleration

Three behaviors explored here are instructive for future exploring this regime. The pump power directly causes increased sideband signal strength due to scattering efficiency effects off of stronger wakefields, but only until the growth rate of the wake is too fast for sustainable electron acceleration. Identifying the appropriate parameters for electron acceleration requires finding the right balance of self-focusing based on the gas jet density and geometry.

The temporal effects observed by the probe depend on the relative delay between the two items. Maximum signal occurs with a slight delay of the probe relative to the pump, aligning the maximum probe energy region with the maximum wakefield amplitude region. Examination of the nonlinear wakefield properties requires being near this overlap position, as both nonlinear and multi-CTS-order shots were only observed close to this position.

Lastly, the location of the focal plane has a dramatic effect on where in the gas jet the wakefield is produced. Improper focal plane choice leads to a region which either cannot produce wakefields for a given intensity or focuses the gas jet to a wakefield-producing ponderomotive profile on the gas jet slope, neither of which are experimentally ideal. Proper choices of this plane will lead to lower shot-to-shot variations and more reproducible outcomes, thus allowing more generalizable results.

No accelerated electrons were measured during these experiments, but is there evidence that electron acceleration likely occurred? As a researcher who came to the field to make electrons fly, this question is an important personal matter if not necessarily of use to the rest of the scientific community. To answer this, consider the results of previous wakefield experiments utilizing the CTS wakefield measurement method. Numerous studies, such as LeBlanc [128] and Tzeng [129], detail electron generation for measured amplitudes substantially below 1 (0.08 to 0.4 for LeBlanc, as small as 0.0625 for Tzeng). The higher end of our experimental measurements fell into this region. Additionally, while LeBlanc's CTS probe extends over approximately 6 plasma periods, our probe extends over an order of magnitude more plasma periods. Given this extended temporal averaging, the wake amplitude in the current experiment is likely significantly underestimated compared to LeBlanc.

The low-power, high-density shot sustained the largest wakefield amplitude, which would also correspond to a gradual focusing beam. The high-power, low-density shots by contrast had fairly average wakefield measurements and would likely break down the wakefield with a sufficiently long propagation length. If electrons were accelerated during these experiments, the low-power, high-density shot is the best candidate.

There is other evidence that electrons are already being accelerated. Simulation results by collaborators at Stony Brook University using a similar laser-plasma

configuration (2 ps, 1 J, $7.5*10^{17}$ cm^{-3}) observed injected electrons, producing 65.5 pC of charge at 7.3 MeV ejected beyond the plasma boundary [127]. Currently, preparations are underway at BNL for a new experimental campaign which will include electron detection. During radiation safety testing of the new experimental configuration, electron radiation was detected emerging from a 2-mm gas jet at $2*10^{18}$ cm^{-3} with a 4-J, 2-ps CO_2 pump pulse driving the plasma wave.

Chapter 7: Conclusions

In conclusion, self-modulated laser wakefields were observed in a gaseous medium using a CO_2 laser for the first time. Wakefield amplitude measurements were made using multiple orders of CTS sidebands, which were comparable in amplitude to previous experiments using shorter wavelengths. Higher-resolution simulations in both 2D and 3D were performed to compare to the experimentally observed data. A thorough exploration of the changes in measured CTS sideband wavelength shifts with focal plane position in a sloped gas jet demonstrated how wavelength shifts can reflect differences in focusing dynamics.

It is unlikely that this work will be extended in the near future, considering the substantial progress accomplished by the researchers at BNL in decreasing the pulse duration and incorporating new isotope species into the CO_2 medium. However, upcoming experimental work in electron diffraction experiments will use the CO_2 laser under similar conditions as were used for the work in this dissertation, raising the possibility of analyzing results in a neighboring parameter space.

REFERENCES

[1] F. E. Rutherford, "The Scattering of α and β Particles by Matter and the Structure of the Atom," *Philosophical Magazine,* pp. 669-688, 1911.

[2] R. J. V. D. Graaff, "A 1,5000,000 Volt Electrostatic Generator," *PROCEEDING of the AMERICAN PHYSICAL SOCIETY,* 1931.

[3] K. T. C. a. L. C. V. A. R. J. Van de Graaf, "The Electrostatic Production of High Voltage for Nuclear Investigations," *Rhys. Rev.,* p. 149, 1933.

[4] L. R. H. A. O. D. M. A. TUVE, "High Voltage Technique for Nuclear Physics Studies," *Physical Review,* p. 315, 1935.

[5] J. D. C. a. E. T. S. Walton, "Experiments with High Velocity Positive Ions.—(I) Further Developments in the method of obtaining High Velocity Positive Ions.," *Proc. Roy. Soc.,' A,,* p. 477, 1930.

[6] J. D. C. a. E. T. S. Walton, "Experiments with High Velocity Positive Ions. II.—The Disintegration of Elements by High Velocity Protons.," *Proc. Roy. Soc.' A ,* p. 658 , 1931.

[7] "The Nobel Prize in Physics 1951," [Online]. Available: https://www.nobelprize.org/prizes/physics/1951/summary/.

[8] "Crooks Tubes - 1870," [Online]. Available: https://nationalmaglab.org/education/magnet-academy/history-of-electricity-magnetism/museum/crookes-tube.

[9] G. Ising, "Prinzip einer Methode zur Herstellung von Kanalstrahlen hoher Voltzahl," *Arkiv för matematik o. fysik,* 1924.

[10] T. M.N. Martins, "Electron accelerators: History, applications, and perspectives," *Radiation Physics and Chemistry,* 2012.

[11] D. Kerst, "A 20-million-electron-volt betatron or induction accelerator.," *Rev. Sci. Instrum. ,* p. 387–94, 1942.

[12] V. Veksler, "A New Method of Accelerating Relativistic Particles," *Dokl. Akad. Nauk SSSR ,* p. 346–348, 1944.

[13] e. a. A. Chao, Handbook of Accelerator Physics and Engineering, 2nd edition, World Scientific, 2013, p. 61.

[14] S. Belomestnykh, "Superconducting RF for storage rings, ERLs, and linac-based FELs. Lecture 1 Introduction: advantages and limitations of SRF technology," Cornell University, 2009.

[15] e. a. T. Behnke, "The International Linear Collider Technical Design Report - Volume 1: Executive Summary," arXiv, 2013 .

[16] W. K. H. PANOFSKY, "Evolution of Particle Accelerators & Colliders," *Beam Line,* 1997.

[17] M. N. P. a. W. D. K. I. V. Pogorelsky, "Mid-infrared lasers for energy frontier plasma accelerators," *PHYSICAL REVIEW ACCELERATORS AND BEAMS,* 2016.

[18] S. Myers, "The LEP Collider, from design to approval and commissioning," 1991.

[19] e. a. Hiroaki Aihara, "The International Linear Collider: A Global Project," *arXiv,* 2019.

[20] O. M. A. A. C. W. S. C. S. M. M. W. G. Xiaa, "Collider design issues based on proton-driven plasma wakefield acceleration," *arXiv,* 2014.

[21] T. H. Maiman, "Stimulated Optical Radiation in Ruby," *Nature,* 1960.

[22] D. S. a. G. MOUROU, "COMPRESSION OF AMPLIFIED CHIRPED OPTICAL PULSES," *OPTICS COMMUNICATIONS,* 1985.

[23] P. F. Moulton, "Spectroscopic and laser characteristics of Ti:Al203," *J. Opt. Soc. Am. B,* 1986.

[24] J. D. Lawson, "LASERS AND ACCELERATORS," *IEEE Transactions on Nuclear Science,* 1979.

[25] L. S. X. D. Y. H. Q. K. P. W. David Cline, "First Observation of Acceleration of Electrons by a Laser in a Vacuum," *Journal of Modern Physics,* 2013.

[26] T. T. a. J. M. Dawson, "Laser Electron Accelerator," *PHYSICAL REVIEW LETTERS,* 1979.

[27] D. Griffiths, " Introduction to Electrodynamics," p. Chapter 5.1.2.

[28] R. Fitzpatrick, "Motion of Oscillating Fields," in *Plasma Physics Book*.

[29] C. B. S. a. W. P. L. E. Esarey, "Physics of laser-driven plasma-based electron accelerators," *REVIEWS OF MODERN PHYSICS,* 2009.

[30] B. Q. a. P. Mora, "Theory and simulation of the interaction of ultraintense laser pulses with electrons in vacuum," *PHYSICAL REVIEW E,* 1998.

[31] C. J. C. D. a. D. U. C. E. Clayton, "Relativistic Plasma-Wave Excitation by Collinear Optical Mixing," *PHYSICAL REVIEW LETTERS,* 1985.

[32] T. M. T. M. K. S. K. M. K. M. K. N. H. A. K. A. T. H. T. a. S. N. Y. Kitagawa, "Beat-Wave Excitation of Plasma Wave and Observation of Accelerated Electrons," *PHYSICAL REVIEW LETTERS,* 1992.

[33] P. S. J. K. a. A. T. Eric Esarey, "Overview of Plasma-Based Accelerator Concepts," *IEEE TRANSACTIONS ON PLASMA SCIENCE,* 1996.

[34] T. T. a. J. M. D. C. Joshi, "Forward Raman Instability and Electron Acceleration," *PHYSICAL REVIEW LETTERS,* 1981.

[35] A. T. E. E. a. P. S. J. Krall, "Self-Modulated-Laser Wakefield Acceleration," *PAC,* 1993.

[36] e. a. A. Modena, "Electron acceleration from the breaking of relativistic plasma waves," *Nature,* 1995.

[37] C. I. M. K. K. C. M. E. E. P. S. R. H. H. R. B. R. F. a. M. B. A. Ting, "Plasma wakefield generation and electron acceleration in a self-modulated laser wakefield accelerator experiment," *Phys. Plasmas,* 1997.

[38] M. C. D. R. W. S.-Y. C. A. M. G. M. a. D. U. S. P. Le Blanc, "Temporal Characterization of a Self-Modulated Laser Wakefield," *PHYSICAL REVIEW LETTERS,* 1996.

[39] e. a. A. J. Gonsalves, "Petawatt Laser Guiding and Electron Beam Acceleration to 8 GeV in a Laser-Heated Capillary Discharge Waveguide," *PHYSICAL REVIEW LETTERS,* 2019.

[40] e. a. X. Wang, "Quasi-monoenergetic laser-plasma acceleration of electrons to 2 GeV," *NATURE COMMUNICATIONS,* 2013.

[41] P. S. J. K. a. A. T. Eric Esarey, "Self-Focusing and Guiding of Short Laser Pulses in Ionizing Gases and Plasmas," *IEEE JOURNAL OF QUANTUM ELECTRONICS,* 1997.

[42] J. D. Jackson, "Section 9.6," in *Classical Electrodynamics, Third Edition*, 1998, p. 425.

[43] A. Siegman, "7.3 The Paraxial Wave Equation," in *Lasers*, 1986.

[44] "Lens Power Formula," http://universalphotonics.com/Portals/0/ReferenceLibrary/lenspowformulaRL.pdf.

[45] S. Karsch, "Generation of high-intensity laser pulses," 2000.

[46] A. Z. E. Hecht, "Harmonic Waves," in *Optics*, 1979, p. 14.

[47] J. D. Jackson, in *Classical Electrodynamics, Third Edition*, p. pg 325.

[48] "Part II - Interaction of Single Atoms," [Online]. Available: (http://www.fz-juelich.de/cae/servlet/contentblob/1076022/publicationFile/26070/SPLIM_Lecture02.pdf.

[49] D. S. D. D. M. S. L. C. a. H. E. S. Augst, "Tunneling Ionization of Noble Gases in a High-Intensity Laser Field," *PHYSICAL REVIEW LETTERS,* 1989.

[50] P. N. Lebedev, "IONIZATION IN THE FIELD OF A STRONG ELECTROMAGNETIC WAVE," *SOVIET PHYSICS JETP,* 1965.

[51] A. M. A. Couairon, "Femtosecond filamentation in transparent media," *Physics Reports,* 2007.

[52] R. Boyd, in *Nonlinear Optics, Third Edition*, p. 579.

[53] J. D. Jackson, "Classical Electrodynamics, Third Edition," p. 313.

[54] A. R. N. a. A. H. F. M. R. Jafari Milani, "Ponderomotive self-focusing of Gaussian laser beam in warm collisional plasma," *Phys. Plasmas,* 2014.

[55] E. O. Y. C. L. a. P. G. Guo-Zheng Sun, "Self-focusing of short intense pulses in plasmas," *The Physics of Fluids,* 1987.

[56] E. E. A. T. a. G. J. P. Sprangle, "Laser wakefield acceleration and relativistic," *Appl. Phys. Lett. 53,* p. 2146, 1988.

[57] T. T. a. J. M. Dawson, "Laser Electron Accelerator," *PHYSICAL REVIEW LETTERS,* pp. 267-270, 1979.

[58] W. L. Kruer, Physics of Laser Plasma Interaction, Westview Press, 2003, p. 73.

[59] T.-Y. C. C.-H. L. J.-Y. L. J. a. S.-Y. C. W.-T. Chen, "Optically Controlled Seeding of Raman Forward Scattering and Injection of Electrons," *PH YSICA L R EV I EW L ET T ERS,* 2004.

[60] W. B. M. a. T. Katsouleas, "Ponderomotive Force of a Uniform Electromagnetic Wave in a Time Varying Dielectric Medium," *PHYSICAL REVIEW LETTERS,* p. 3495, 1992.

[61] M. C. D. R. W. S.-Y. C. A. M. G. M. a. D. U. S. P. Le Blanc, "Temporal Characterization of a Self-Modulated Laser Wakefield," *Phys. Rev. Letters,* p. 5381, 1996.

[62] S. K. Y. K. S. L. M. D. J. Koga, "Optical field ionization effects on the generation of wakefields with short pulse lasers," *Nuclear Instruments and Methods in Physics Research A,* pp. 499-504, 1998.

[63] B. H. P. S. R. F. H. J. R. P. a. W. B. M. D. F. Gordon, "Seeding of the forward Raman instability by ionization fronts and Raman backscatter," *PHYSICAL REVIEW E,* p. 046404, 2001.

[64] W. B. M. a. T. K. C. D. Decker, *Phys. Rev. E,* 1994.

[65] W. B. M. T. K. K.-C. Tzeng, "Self-trapped electron acceleration from the nonlinear interplay between Raman forward scattering, self-focusing, and hosing," *PHYSICS OF PLASMAS,* p. 2105, 1999.

[66] R. Fitzpatrick, "Plasma Physics by Richard Fitzpatrick," 2019. [Online].

[67] S. M. Hooker, "Developments in laser-driven plasma accelerators," *NATURE PHOTONICS,* p. 775, 2013.

[68] C. B. S. a. W. P. L. E. Esarey, "Physics of laser-driven plasma-based electron accelerators," *REVIEWS OF MODERN PHYSICS,* 2009.

[69] J. M. DAWSON, "Nonlinear Electron Oscillations in a Cold Plasma," *The Physical Review,* 1959.

[70] B. H. R. H. a. A. T. E. Esarey, "Trapping and Acceleration in Self-Modulated Laser Wakefields," *Phys. Rev. Letters,* 1998.

[71] E. E. B. A. S. a. W. P. L. C. B. Schroeder, "Trapping, dark current, and wave breaking in nonlinear plasma waves," *Phys. Plasmas 13,* 2006.

[72] e. a. A. Modena, "Electron acceleration from the breaking of relativistic plasma waves," *Nature,* 1995.

[73] K. C. T. C. E. C. A. E. D. V. M. K. A. M. A. M. W. B. M. D. Gordon, "Observation of Electron Energies Beyond the Linear Dephasing Limit from a Laser-Excited Relativistic Plasma Wave," *Phys. Rev. Letters,* 1998.

[74] C. I. M. K. K. C. M. E. E. P. S. R. H. H. R. B. R. F. a. M. B. A. Ting, "Plasma wakefield generation and electron acceleration in a self-modulated laser wakefield accelerator experiment," *Physics of Plasma,* 1997.

[75] B. H. R. H. a. A. T. E. Esarey, "Trapping and Acceleration in Self-Modulated Laser Wakefields," *Phys. Rev. Letters,* 1998.

[76] M. A. E. M. S. K. S. M. T. W. A. O. A. M. T. K. KOYAMA, "Monoenergetic electron beam generation from a laser-plasma accelerator," *Laser and Particle Beams,* pp. 95-100, 2006.

[77] F. P. a. A. M. P. S.V. Bulanov, "Two-Dimensional Regimes of Self-Focusing, Wake Field Generation, and Induced Focusing of a Short Intense Laser Pulse in an Underdense Plasma," *PHYSICAL REVIEW LETTERS,* p. 710, 1995.

[78] F. P. A. M. P. a. A. S. S. S. V. Bulanov, "Transverse-Wake Wave Breaking," *PHYSICAL REVIEW LETTERS,* p. 4205, 1997.

[79] P. e. a. Bertrand, *Phys. Plasma 2,* p. 3115, 1995.

[80] A. T. K. K. E. E. R. F. H. B. H. H. R. B. C. M. a. P. S. C. I. Moore, "Electron Trapping in Self-Modulated Laser Wakefields by Raman Backscatter," *PHYSICAL REVIEW LETTERS,* p. 3909, 1997.

[81] G. A. H. L. F. B. M. F. S. J. K. W. a. H. M. M. A. J. Goers, "Multi-MeV Electron Acceleration by Subterawatt Laser Pulses," *PHYSICAL REVIEW LETTERS,* 2015.

[82] e. a. Michiaki Mori, "Condition of MeV Electron Bunch Generated from Argon Gas-Jet Target in the Self-Modulated Laser Wakefield Regime," *J. Phys. Soc. Jpn.,* 2011.

[83] N. L. J. L. S. B. B. P. C. G. W. S. A. M. S. K. A. M. A. P. J. E. R. J. L. M. L. D. A. R. F. S. H. G. J. D. M. a. C. J. F. Albert, "Observation of Betatron X-Ray Radiation in a Self-Modulated Laser Wakefield Accelerator Driven with Picosecond Laser Pulses," *Phys. Rev. Letters,* 2017.

[84] D. R. P. E. C. G. F. C. G. R. G. E. E. B. A. S. G. J. H. B. J. v. T. S. C. J. S. W. L. A. M. R. D. S. D. R. S. K. L. B. R. D. e. a. W. P. Leemans, "Laser wakefield accelerator experiments at LBNL," *AIP Conference Proceedings,* 2001.

[85] E. M. K. K. S. K. M. A. T. W. K. T. a. M. T. S. Masuda, "Energy scaling of monoenergetic electron beams generated by the laser-driven plasma based accelerator," *Phys. Plasmas,* 2007.

[86] D. K. D. F. G. R. F. H. a. P. S. A. Ting, "Generation and measurements of high energy injection electrons from the high density laser ionization and ponderomotive acceleration," *Phys. Plasmas,* 2005.

[87] G. H. K. C. K. H. S. N. HAFZ, "GENERATION OF GOOD-QUALITY RELATIVISTIC ELECTRON BEAM FROM SELF-MODULATED LASER WAKEFIELD ACCELERATION," *International Journal of Modern Physics B,* 2007.

[88] J. F. J. R. M. F. A. J. P. R. S. R. J. P. C. Z. N. B. W. P. M. a. A. S. V. Malka, "Characterization of electron beams produced by ultrashort (30 fs) laser pulses," *Physics of Plasmas,* 2001.

[89] K. K. E. L. C. S. P. D. M. B. W. A. E. D. S. F. V. M. E. L. D. G. F. S. T. a. C. J. Z. Najmudin, "Self-modulated wakefield and forced laser wakefield acceleration of electrons," *Physics of Plasmas,* 2003.

[90] M. K. A. M. R. W. a. D. U. S.-Y. Chen, "Detailed dynamics of electron beams self-trapped and accelerated in a self-modulated laser wakefield," *Physics of Plasmas,* 1999.

[91] A. M. P. A. N. a. P. D. G. Sanyasi Rao Bobbili, "Generation of a highly collimated, mono-energetic electron beam from laser-driven plasma-based acceleration," *New Journal of Physics,* 2010.

[92] e. a. K. Nakajima, "Observation of Ultrahigh Gradient Electron Acceleration by a Self-Modulated Intense Short Laser Pulse," *Phys. Rev. Letters,* 1995.

[93] S. M. a. E. Miura, "Generation and analysis of quasimonoenergetic electron beams by laser-plasma interaction in transitional region from the self-modulated laser wakefield to bubble acceleration regime," *Phys. Plasmas,* 2009.

[94] E. M. K. K. a. S. K. S. Masuda, "Energy scaling of monoenergetic electron beams generated by the laser-driven plasma based accelerator," *Phys. Plasmas,* 2007.

[95] S.-Y. C. A. M. a. D. U. R. Wagner, "Electron Acceleration by a Laser Wakefield in a Relativistically Self-Guided Channel," *Phys. Rev. Letters,* 1997.

[96] A. T. K. K. E. E. R. F. H. B. H. H. R. B. C. M. a. P. S. C. I. Moore, "Electron Trapping in Self-Modulated Laser Wakefields by Raman Backscatter," *Phys. Rev. Letters,* 1997.

[97] C. B. D. C. D. D. W. B. M. K.-C. T. K. A. M. C. E. C. a. C. J. C. A. Coverdale, "Propagation of Intense Subpicosecond Laser Pulses through Underdense Plasmas," *Phys. Rev. Letters,* 1995.

[98] A. M. P. A. N. a. P. D. G. B. S. Rao, "Effect of chirp on self-modulation and laser wakefield electron acceleration in the regime of quasimonoenergetic electron beam generation," *PHYSICAL REVIEW SPECIAL TOPICS - ACCELERATORS AND BEAMS,* 2013.

[99] M. C. D. R. W. S.-Y. C. A. M. G. M. a. D. U. S. P. Le Blanc, "Temporal Characterization of a Self-Modulated Laser Wakefield," *Phys. Rev. Letters,* 1996.

[100] e. a. Esarey, *Rev. Mod. Phys.,* pp. 1229-1285, 2009.

[101] "Helmholtz Zentrum Berlin," [Online]. Available: https://www.helmholtz-berlin.de/media/media/grossgeraete/mi_synchro/world_of_synchrotron/photons/hhg_01.jpg .

[102] e. a. J. L. Krausse, *Phys. Rev. Letters,* pp. 3535-3538, 1992.

[103] C. Patel, "Continuous-Wave Laser Action on Vibrational-Rotational Transitions of CO2," *Physical Review - PHYS REV X,* pp. 1187-1193, 1964.

[104] e. a. C. Joshi, *Phys. Rev. Letters,* pp. 1285-1288, 1981.

[105] W. Rath, "CO2 Laser – Workhorse for," *Laser Technik Journal,* pp. 32-38, 2009.

[106] P. K. Cheo, "CO2 Lasers," in *Lasers, Vol. 3*, New York, Marcel Dekker, Inc., 1971, pp. 111-267.

[107] A. Damato, "Wikipedia page of Carbon Dioxide," 31 August 2007. [Online].

[108] C. C. Davis, Lasers and Electro-Optics: Fundamentals and Engineering, 219.

[109] M. R. M. a. R. I. Teresita K. Kolenchak, "Competitive High-Power Laser Technology Overview," II-VI Infrared, 2004.

[110] K. F. W. a. A. Sanchez, "Tunable Sapphire Laser," *The Lincoln Lab Journal,* pp. 447-462, 1990.

[111] M. B. I. B.-Z. J. S. M. P. I. Pogorelsky, "BESTIA - the next generation ultra-fast CO2," BNL, 2015.

[112] I. Pogorelsky, "Terawatt Picosecond CO2 Laser Technology for," in *CP472, Advanced Accelerator Concepts: Eighth Workshop,*.

[113] e. a. J. S. Ross, "Thomson-Scattering Measurements in," in *18th Topical Conference High Temperature Plasma Diagnostic*, Wildwood, NJ.

[114] R. Z. A. D. U. S. M. C. K. M. C. Downer, "Diagnostics for plasma-based electron accelerators," *Rev. Mod. Phys.,* 2017.

[115] R. E. S. a. C. M. Surko, "Study of density fluctuations in plasmas by small-angle CO2 laser scattering," *The Physics of Fluids 23,* pp. 472-490, 1980.

[116] R. Boyd, Nonlinear Optics, Third Edition, pg. 79: Academic Press, 2008.

[117] R. Fitzpatrick, "Plasma Physics by Richard Fitzpatrick," 24 June 2019. [Online].

[118] H. Bindslev, On the Theory of Thomson, Roskilde, Denmark: Risø National Laboratory, 1992.

[119] R. W. C. C. a. C. J. D. Umstadter, "Observation of Steepening in Electron plasma Waves Driven by Stimulated Raman Backscatfering," *Phys. Rev. Letters,* pp. 292-295, 1987.

[120] K. K. C. I. M. H. R. B. E. E. J. K. a. P. S. A. Ting, "Measured, Temporal Evolution of Self-Modulated Laser Wakefields," *Phys. Rev. Letters,* pp. 5377-5380, 1996.

[121] M. C. D. R. W. S.-Y. C. A. M. G. M. a. D. U. S. P. Le Blanc, "Temporal Characterization of a Self-Modulated Laser Wakefield," *Phys. Rev. Letters,* pp. 5381-5384, 1996.

[122] T. K. K.-C. Tzeng and W. B. Mori, "Self-trapped electron acceleration from the nonlinear interplay between Raman forward," *PHYSICS OF PLASMAS,* pp. 2105-2116, 1999.

[123] J.-C. D. J. J. G. V. a. A. P. Arvydas Umbrasas, "Generation of femtosecond pulses through second-harmonic compression of the output of a Nd:YAG laser," *OPTICS LETTERS,* pp. 2228-2230, 1995.

[124] K. Y. R. Z. L. D. A. M. D. R. S. N. V.-N. a. J. W. Prabhat Kumar, "Simulation study of CO2 laser-plasma interactions and self-modulated wakefield acceleration," *Physics of Plasmas,* 2019.

[125] L. e. al., *PRL,* p. 113, 2014.

[126] e. a. Sävert, *PRL,* p. 115.

[127] K. Y. L. A. M. D. P. I. V. L. N. V.-N. J. W. J. Y. R. Z. R. S. P. Kumar, "Self-modulated laser wakefield acceleration driven by CO2 laser in hydrogen plasma," in *EPS*, 2019.

[128] M. C. D. R. W. S.-Y. C. A. M. G. M. a. D. U. S. P. Le Blanc, "Temporal Characterization of a Self-Modulated Laser Wakefield," *Phys. Rev. Letters,* 1996.

[129] W. B. M. a. T. K. K.-C. Tzeng, "Self-trapped electron acceleration from the nonlinear interplay between Raman forward scattering, self-focusing, and hosing," *Physics of Plasma,* 1999.